

**PARTICLE IMAGE VELOCIMETRY MEASUREMENTS OF BLOOD FLOW IN ANEURYSMS
USING 3D PRINTED FLOW PHANTOMS**

by

ILUNGA JEANMARK TSHIMANGA

submitted in accordance with the requirements for
the degree of

MASTER OF SCIENCE IN PHYSICS

in the subject

MECHANICAL AND INDUSTRIAL ENGINEERING

at the

UNIVERSITY OF SOUTH AFRICA

SUPERVISOR: PROF WEI HUA HO

CO-SUPERVISOR: DR MALEBOGO NGOEPE (University of Cape Town)
&
DR PATRICK H GEOGHEGAN (Aston University)

(November 2019)

DECLARATION

Name: _____ILUNGA JEANMARK TSHIMANGA_____

Student number: _____46921664_____

Degree: _____MASTER OF SCIENCE IN PHYSICS (FULL DISSERTATION) 98980_____

Exact wording of the title of the dissertation as appearing on the electronic copy submitted for examination:

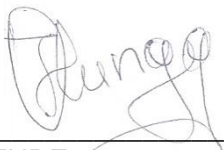
PARTICLE IMAGE VELOCIMETRY MEASUREMENTS OF BLOOD FLOW IN ANEURYSMS

USING 3D PRINTED FLOW PHANTOMS

I declare that the above dissertation is my own work and that all the sources that I have used or quoted have been indicated and acknowledged by means of complete references.

I further declare that I submitted the dissertation to originality checking software and that it falls within the accepted requirements for originality.

I further declare that I have not previously submitted this work, or part of it, for examination at Unisa for another qualification or at any other higher education institution.



SIGNATURE

09/11/2019

DATE

SUMMARY:

Cardiovascular diseases (CVD) remain one of the leading causes of deaths worldwide. The formation and presence of aneurysm is a very important question in the study of this CVDs. An aneurysm is a balloon-like bulge on a blood vessel which forms over time. An aneurysm is usually considered to be a result of weakening of the blood vessel walls, this definition has stood over many years without being conclusively proven. Eventually, the aneurysm could clot or burst due to degradation of the aneurysm wall and accumulation of blood. The latter would lead to internal bleeding and result in a stroke. Local hemodynamics have been found to be very important in the study of the evolution of an aneurysm. In this study, a steady flow experimental investigation was conducted using planar Particle Image Velocimetry (PIV) on a rigid flow phantom of an idealised geometry consisting of a curve parent artery and a spherical aneurysm located on the outer convex side of the curvature. The flow phantom was fabricated directly using a commercially available desktop Stereolithography (STL) 3D printer instead of the more conventional investment casting method using a core. Although 3D printing technologies have been around for many years, the fabrication of flow phantoms by direct printing is still largely under-explored. This thesis details the results of investigation into the optimal printing and post-printing procedures required to produce a flow phantom of suitable clarity and transparency. Other important areas of concern such as the geometric accuracy, surface topography and refractive index of the final model are also investigated. A planar PIV is conducted to study the impact of flow rates on the local flow field in and around the aneurysm and their impact on the wall shear stress. It was found that direct 3D printing is appropriate for the fabrication of flow phantoms suitable for PIV or other flow visualisation techniques. It reduces the complexities and time needed compared to the conventional investment casting methods. It was observed that the optical properties of the printed material such as the high refractive index (RI) and the transmittivity of light could cause a problem in large models. From the PIV measurements it was found that flow rates affect the flow field in both the parent artery and the aneurysm. First, high velocities were observed on the outer curvature of the parent artery. Secondly the centre of rotation in the aneurysm is not at the geometric centre but is displaced slightly in the direction of the flow. Finally, the flow rate affects the angle in which flow enters the aneurysm from the parent vessel. This change in the flow angle affects the flow within the aneurysm. A higher flow rate in the parent artery increases the incident angle which brings the centre of rotation closer to the geometric centre of the aneurysm, this changes the location and magnitude of high velocities and hence the local wall shear stress (WSS) on the wall of the aneurysm. This may have implications in the evolution of aneurysms.

KEY TERMS:

Seeding Particles, Particle Image Velocimetry PIV, Flow phantom, 3D printing, Cross-correlation, Cerebral Aneurysm, CFD, Ammonium thiocyanate, Stereolithography SLA, Manufacturing, Idealised geometry, Blood flow, Cardio-vascular diseases, in-vitro

To
you *Albertine Mbuyi Mudingayi*
A toi maman.

Acknowledgements

I was truly fortunate during my studies towards this Master's degree. It is with a lot of gratitude that would like to acknowledge the help and support that I benefitted throughout the course of the project.

First and foremost, I would like to thank my supervisor Prof Ho. From the moment I met Prof Ho to these days I still admire him as a person, his hard-working spirit, his passion for research and most of all his kind heart that always seem to answer the needs around him. He has been a supervisor, a mentor and in most cases a friend to me. For all the time we spend working in the labs, meeting in office and online, I ought to be grateful and I humbly say thanks. I have learned a great deal just by working around him, his positive impact will always be there in me and I hope that through this work he realizes that he did not just graduate a student but imparted his bright skills on so many of us. The same goes to my co-supervisors Dr Malebogo and Dr Geoghegan and just the thought of being their student was for me extraordinary and surreal. I am so fortunate to be guided and to learn from such excellent and admirable people. I only wish to keep this link with you always and may the work that you have invested in me bear more fruits.

I also want to thank the university and in a special way the department of Mechanical and Industrial engineering for being such a great environment for me and for providing me with financial support. I also benefitted from the Unisa 2019 Masters and Doctoral Bursary by experimental work. I want to personally thank all our staff in our department and in a special way to our admin: Nellie, Dorcas, Gugu and Matsepho for being like a family support to me. I also want to thank my friends Tolu, Rabe, Felix, Tshamano and Jane who have helped me with countless encouragements and guidance. Special thanks to Dr Linda Mthembu for all his assistance and especially regarding presentations skills.

This project was conducted conjointly with Mr. Struan Hume from the university of Cape Town who was doing the computational Fluid Dynamics (CFD) simulation part of this project. Special thanks equally to Mr. Struan Hume for his collaboration.

Finally, I would like to thank people with whom a share a special bond. My parent Jean-marie Tshimanga and Albertine Mbuyi. My sisters Rosette, Ruth, Sarah and Noella and my brothers Christian and Jeff and all people of good faith who have contributed in one way or another to my progress. Your love and your support could not be measured, your faith and your prayers have kept me blessed and I am grateful to have had such companions, thank you Marie. Toute Gloire à celui qui est seigneur et qui donne vie.

Publications arising from this work

Journal Papers

Published

1. WH Ho, **IJ Tshimanga**, MN Ngoepe, MC Jermy, and PH Geoghegan (2019). *Evaluation of a desktop 3D printed rigid refractive-indexed-matched flow phantom for PIV measurements on cerebral aneurysms*. Cardiovascular Engineering and Technology

In preparation

1. Struan Hume*, **Jean-Marc Ilunga Tshimanga** * *Joint first authorship. *Experimental and computational exploration of the effect of pulsatility on the transport of thrombin in aneurysm geometries*.

Conference Proceedings and Poster

1. **I.J. Tshimanga**, W.H. Ho, M. Ngoepe, M.C. Jerm and P.H. Geoghegan. *Particle Image Velocimetry analysis of blood flow in idealised cerebral aneurysm using refractive index matched 3D printed flow phantoms*. The 8th International Conference on Biomedical Engineering and Biotechnology (ICBEB 2019). October 22-25, 2019 Seoul, Republic of Korea
2. **I.J. Tshimanga**, W.H. Ho, M. Ngoepe, M. C. Jermy, P.H. Geoghegan. *Development of 3D Printed Models for Arterial Disease Investigation*. BioMedEng18 Conference at Imperial College London from 6 - 7th September 2018.

International Workshops and Symposium

1. **Ilunga Jeanmark Tshimanga** (Unisa, South Africa). *Particle Image Velocimetry measurements of blood flow in aneurysms in 3D printed models*, 4th European-South African Cardiovascular Research workshop. 1st-3rd April 2019, STIAS, Stellenbosch, South Africa
1. **Ilunga Jeanmark Tshimanga** (Unisa, South Africa), *Particle Image Velocimetry measurements of blood flow in aneurysms using 3D printed flow phantoms*. 1st Unisa International Symposium of Biomechanics in Bio-Fluids and Soft Tissue Mechanics. 3rd of April 2018, Unisa Science Campus, Johannesburg, South Africa.

Table of Contents

SUMMARY:	3
Acknowledgements	5
Publications arising from this work	6
List of figures	11
List of tables	13
CHAPTER 1: THE INTRODUCTION	14
1.1. Burden of cardiovascular disease	14
1.2. Cerebral aneurysms	14
1.3. Cerebral aneurysm treatment	15
1.4. Approaches for improving understanding of aneurysms	16
1.5. Focusing on experimental techniques: PIV and flow phantom fabrication	18
1.6. Goal of the study	20
1.6.1. Problem statement	20
1.6.2. Aim of the study	20
1.6.3. Project objectives	21
1.6.4. Scope and limitations	21
1.7. Thesis outline	22
2.1. Classification and identification of aneurysms	23
2.1.1. Classification of aneurysms	23
2.1.2. Identification of cerebral aneurysms	24
2.2. Effect of hemodynamics on aneurysm growth, rupture and clotting	25
2.3. Computational approaches for solution of biofluid flow problems	26
2.4. Experimental studies	28

2.4.1 Fabrication of the flow phantom	28
2.4.2. 3D printing use in PIV	30
2.5. Conclusion	32
CHAPTER 3: <i>IN VITRO</i> EXPERIMENTAL SETUP	33
3.1. Introduction	33
3.2. Flow setup	34
3.3. Devices	36
3.4. Pulsatile flow system	37
3.4.1. Pulsatile system configuration	37
3.4.2. Flow configuration	38
3.5. Conclusion	41
CHAPTER 4: FLOW PHANTOM FABRICATION	42
4.1. Introduction	42
4.2. Investment casting	42
4.2.1. Investment casting process	42
4.3. 3D printing	43
4.3.1. 3D printing technologies	43
4.4. Phantom geometries	45
4.4.1. Idealised geometry	46
4.4.2. Realistic geometry	47
4.5. 3D printing of Flow Phantom	48
4.6. Matching the refractive index between flow phantom and working fluid	50
4.7. Refractive index check using MATLAB	51
4.8. Surface roughness measurements	52

4.9. Conclusion	53
CHAPTER 5 : PARTICLE IMAGE VELOCIMETRY (PIV)	54
5.1. Introduction	54
5.2. PIV as a tool for fluid flow measurement	54
5.2.1. Laser	55
5.2.2. Camera	56
5.2.3. Seeding particles	58
5.3. Cross-correlation	59
5.3.1. Cross-correlation used in this work	59
5.3.2. Types of cross-correlation in use	59
5.3.4. Discrete Fourier Transform (DFT)	61
5.4. Calculation of Δt	62
5.5. Laser Timing	63
5.6. Accuracy evaluation in PIV	65
5.7. PIV image recording	66
5.7.1. Image recording session	66
5.7.2. Pre-processing: Background removal	67
5.7.3. Post-processing: Analyzing images using PIVLab	68
5.7.4. PIVLab results output and planes of interest	69
5.8. Conclusion	70
CHAPTER 6: RESULTS AND DISCUSSION	71
6.1. Introduction	71
6.2. Flow velocity results	71
6.3. Evidence of hemodynamic influence in aneurysm	76

CHAPTER 7: CONCLUSIONS AND FUTURE WORK	78
7.1. Conclusion	78
7.2. Future work	79
REFERENCES	80
Appendix A – Specifications of the Firefly Laser	85
Appendix B – Specifications of the pco.pixelfly PIV camera	86
Appendix C – Specifications of the SunSun Pump	87
Appendix D – Specifications of the Flow Meter	87
Appendix E – clear photopolymer resin form 2 material sheet	88
Appendix F – Stepper motor	89
Appendix G – Flow setup (3D printed parts)	89

List of figures

Figure 1 Fabrication of a flow phantom in investment casting (image by Geoghegan et al. 2012).....	19
Figure 2 description of Aneurysms (a) Cerebral aneurysm and (b) Abdominal aortic aneurysm.....	23
Figure 3 typical image of blood vessels around the brain/ Wikipedia common.....	24
Figure 4: Mechanical interpretation of the cardiovascular system. (a) Representing the actual cardiovascular system and (b) representing the mechanical interpretation	33
Figure 5: Schematic view of the experimental setup.....	34
Figure 6 experimental setup is presented	35
Figure 7 Stepper motor connected to the valve	37
Figure 8 Stepper motor and Arduino board connection	38
Figure 9 picoScope output from channel B for steady 0.202 l/min flow rate.....	38
Figure 10 Pulsatile profile recorded with a picoScope	39
Figure 11 Valve calibration.....	39
Figure 12 Stepper motor programing	40
Figure 13 Actual flow rate recorded.....	40
Figure 14 Percentage error after comparison of the expected and the actual flow profile	41
Figure 15 SLA printing in resin bath.....	44
Figure 16 Inkjet 3D printing.....	45
Figure 17 Idealised geometry STL file	46
Figure 18 Idealized flow phantom	46
Figure 19 Realistic geometries	47
Figure 20 Realistic model final design	47
Figure 21 Idealised geometry model printed on SLA 3D printer	48
Figure 22 3D printed realistic geometry on SLA 3D printer.....	49
Figure 23 RI matching test during PIV	51
Figure 24 Viscosity of the working fluid	51
Figure 25 RI check during PIV experiments	52

Figure 26 Typical PIV configuration	55
Figure 27 pco.pixelfly usb quantum efficiency graph	57
Figure 28 Direct cross-correlation	61
Figure 29 DFT measurements principles by calculating the correlation matrix in the frequency domain by detecting intensity peak.....	61
Figure 30 a. Trigger opening time, b. Camera exposure, c. Laser firing times	64
Figure 31 Laser and camera setup configuration	64
Figure 32 Front view of the printed model as seen from the camera	66
Figure 33 Typical raw image pair.....	67
Figure 34 Raw PIV image for the idealized geometry	68
Figure 35 PIV image after background subtraction.....	68
Figure 36 External image with contours of the middle plane	69
Figure 37 Blended image made of the background subtracted raw PIV image and the drawn mask	69
Figure 38 Typical PIV output results using PIVlab	69
Figure 39 Planes of the idealized geometry model on which PIV analysis were conducted	70
Figure 40 PIV velocity (m/s) results at middle plane of the artery.....	72
Figure 41 PIV results at a plane 2 mm away from middle plane	73
Figure 42 PIV image on plane 4 mm away from the center of aneurysm.....	74
Figure 43 PIV image on plane 6 mm away from the center of aneurysm.....	74
Figure 44 Vorticity location	75
Figure 45 PIV vorticity at middle plane	76
Figure 46 Flow visualization inducing dye inside the aneurysm.....	76
Figure 47 PIV results showing velocity distribution in the parent vessel and inside aneurysm	76

List of tables

Table 1 list of available transparent material	31
Table 2 Challenges in the field of aneurysm studies	31
Table 3 3D printing technologies (prices as of 2018)	44
Table 4 Material properties.....	49
Table 5 RI check using MATLAB Image Viewer	52
Table 6 Summary of the printed part	53
Table 7 Specifications of the oxford Firefly Laser	56
Table 8 Specification of the PIV camera	57
Table 9 The pixel clock	58
Table 10 In-Vivo data	62
Table 11 In-vitro data.....	62

CHAPTER 1: THE INTRODUCTION

1.1. Burden of cardiovascular disease

In the year 2015, 17.7 million people died from cardiovascular diseases (CVDs), representing 31% of deaths worldwide and this number is seen on the rise in the year 2016 as cardiovascular diseases caused 17.9 million deaths, which accounted for 44% death of noncommunicable disease worldwide (Organization World Health, 2018). The WHO has stated that early detection of cardiovascular diseases is preferable in order to enable adoption of effective management and treatment strategies. CVDs are linked with failure of the heart and blood vessels. Examples of CVDs are coronary heart disease, aortic disease and cerebrovascular disease. Aneurysm formation may be encountered in aortic and cerebral arteries, potentially resulting in blood vessel failure. Thrombosis is also closely associated with CVDs, and can cause an obstruction and an infarct or can be carried to the heart and lungs and this can be fatal.

An aneurysm, which is a balloon-like bulge on a blood vessel, forms at a weak spot along the artery (esculap Neurosurgery, 2012). Over time, the aneurysm could clot or burst, which would lead to potentially fatal cerebral haemorrhaging. Former French president Charles de Gaulle and physicist Albert Einstein are notable victims of aneurysms.

1.2. Cerebral aneurysms

Aneurysms have been the subject of many investigations in the past centuries and continue to remain arguably a challenging topic in the cardiovascular field today. Packet et al (2006) have described an aneurysm as a localized dilatation or inflation of a blood vessel. The word dilatation implies an expansion of volume due to an external physical factor (Norman and Powell, 2010). A different definition has suggested that a 1.5 increase in diameter is generally accepted as a good definition of an aneurysm, and seems to identify a pathological change in size (Norman and Powell, 2010). The consideration of volumetric change does not detail whether the dilatation is a result of pressure increase, heat or excessive accumulation of blood and still needs further investigations. This indicates that aneurysms are still not well understood. Packet has suggested that aneurysms form as a result of blood inflating stretched blood vessels as they weaken (Packet, 2006). People with aneurysms often do not have any symptoms until a rupture occurs (esculap Neurosurgery, 2012). Symptoms accompanying rupture can include severe headache, nausea, vomiting, brief blackout, paralysis or loss of control on one side of the body, vision and speech problems, and even death.

The history of aneurysms can be traced back to fourteenth century B.C., it has been recorded that ancient Egyptians use to practice magico-religious therapies as a method for treating aneurysms, (Sigerst, 1951; Grob,

1998). In the Ebers Papyrus, aneurysms are listed among the diseases, suggesting that awareness of the arterial disease has been around for as long as civilization itself. The famous Greek physician Galen of Pergamon (129 AD – c. 200/c. 216) is regarded as the first to give a description of the disease and to give it a definition. He made a sharp distinction between aneurysms and other diseases, which were described as dilatation of arteries. Traumatic aneurysms were frequent during his time and Galen of Pergamon, who was a physician to the gladiators and, frequently managed traumatic aneurysms, which appeared as lesions and could be discovered through eye inspection (Stehbens, 1958).

In 1554, Saporta gave the first recorded explanation of the causes of aneurysms (Stehbens, 1958). At the time, it was believed that aneurysms formed when the arterial coat ruptured. This description is not far from the current explanation, which hypothesizes that aneurysms form as a result of weakened arterial vessel walls. In the sixteenth century, syphilis was believed to cause aneurysms. It was also argued that not all aneurysms were subject to the pulsatility, which is characteristic of arterial flows. The argument was based on the fact that for an aneurysm sac occluded by a thrombus, there is less circulation of fresh blood, hence less response to its pulsatile nature. A different hypothesis relating to the origin of aneurysms focused on the erosive quality of the blood. Finally, Lancisi hypothesized that aneurysms were a form of congenital disease, stating that “an artery may be constructed by nature with fibers too slack or too small” (Stehbens, 1958).

The first recorded experimental study to investigate the origin of aneurysms dates as far back as 1793 and was conducted by John Hunter (Stehbens, 1958). The experiment was carried out on a living animal, where the carotid artery wall of a dog was sliced up and made very thin on a localized section. After three weeks of observations, the results failed to prove that thinner walls generate aneurysms. A major breakthrough came in the nineteenth century, when it was discovered that the rupture of the intimal and medial layers initiates aneurysm formation. Aneurysmal rupture was then attributed to atheromatous ulceration (Krings, Daniel M. Mandell, *et al.*, 2011).

Even though aneurysms have been investigated for a long time, the exact pathophysiology is not well understood (Sheppard, 2012). There is a lack of accurate information on how the arterial wall changes from a healthy condition to an aneurysmal condition (Ford *et al.*, 2005). Advances in medical imaging technology have made it possible to detect ruptured and unruptured aneurysms but this comes with a cost even in countries with high income and early detection of aneurysm remains a luxury. Even with this insight, it remains difficult to predict growth patterns and likelihood of rupture. Tools that enable monitoring and management of aneurysms on a per patient basis are highly desirable.

1.3. Cerebral aneurysm treatment

Aneurysms can be treated using a surgical or endovascular approach. In the case of open surgery, a surgical operation is needed to gain access to the brain through the skull. An anaesthetic is usually administered to

ensure that the operation is conducted while the patient sleeps, isolated from pain. Under this condition, a section of the bone is cut and lifted away, followed by the removal of the dura which is peeled back. This allows easy access to the matter. Blood as well as cerebrospinal fluid can be removed. In the surgical approach, a micro-clip is placed around the neck of the aneurysm (Yu *et al.*, 2012). In the case where rupture has occurred, the aneurysm can be clipped, with the intention to permanently prevent further bleeding. In the case of occlusion of the brain artery, a bypass is usually considered to artificially supply blood over the occluded part using a different route through an artificial blood vessel.

The endovascular process is an alternative treatment which intends to accelerate clot formation inside the aneurysm, preventing any blood flow into the bulge. This is a procedure which employs a catheter to guide either platinum coils, a stent or a flow diverter to the aneurysm through the arteries. Flow diverters are an increasingly common technique for treating aneurysms. The intervention is conducted in an x-ray lab to provide visual access to the aneurysm and arteries connecting to it.

Endovascular and surgical approaches are both risky, and can result in the following consequences:

- Accidental inflammation or bleeding inside the brain
- Permanent damage of arteries which can result in paralysis, loss of sight and sensation
- Deficiency in memory capacity
- Death

1.4. Approaches for improving understanding of aneurysms

In-depth understanding of aneurysms is required in order to manage the disease effectively. Statistics of patient outcomes have been beneficial for understanding aneurysm trends. In addition, hemodynamic characteristics inside aneurysms are regarded by many as a key factor which can help to understand aneurysm progression over time (Kakalis *et al.*, 2008).

Statistical data relating to aneurysm patients is often used to understand the pathophysiology of the disease (Wolfe and Bas, 2006). Data relating to the interaction between aneurysms and other diseases has proven useful. From 2001 to 2004, a study focusing on cerebral aneurysms was conducted in Japan, in order to identify the correlation between other diseases and aneurysms, as well as their specific contribution to the risk of rupture (The UCAS Japan, 2012) Patients enrolled in the study were selected on the basis of age, with a minimum age requirement of 20 years. The other criterion was the size of the unruptured aneurysm, which had to be greater than 3mm. Recorded data included details such as the clinical characteristics of the patient, a description of the aneurysm and the management plan. Follow-up was continued for several months or even years, until rupture or death occurs. The clinical status of each patient was recorded using the modified Rankin scale, and changes in the morphology of the aneurysm, including subarachnoid haemorrhage, were captured

using computed tomographic (CT) imaging or lumbar puncture. In cases where the patient had died, an autopsy was conducted. External investigators were consulted in order to confirm the accuracy of the data in the registry. The study concluded that the natural course of unruptured cerebral aneurysms depends on size, location and shape.

Investigating the characteristics of hemodynamics inside aneurysms can generate useful information which can be used to support diagnoses (Kefayati, 2013). Intrusive methods to study blood flow in cerebral arteries can expose the patient to a risk such as symptomatic epilepsy (World Health Organisation, 2015). Hence non-intrusive methods are preferred choices. Non-invasive in-vivo techniques such as Doppler ultrasound and magnetic resonance imaging (MRI) can be used to measure the flow rate in blood vessels with limited resolution (Geoghegan et al. 2012). Experimental techniques, such as PIV, have been used to study hemodynamics of aneurysms. Computational fluid dynamics has also been used as a tool for gaining insight into the flow in the aneurysm and parent vessel (Peach et al. 2014, Chong et al. 2014, Kakalis et al. 2008).

Experimental and computational studies make use of idealised and realistic or patient-derived geometries. The development of these tools is based on the assumption that hemodynamic conditions make a significant contribution to the formation, growth and rupture of cerebral aneurysms. The idealized geometries can be regarded as simplified models that approximate patient-specific geometries for the general population of a particular type of aneurysm. Patient-specific models must first be built from 3D computed tomography CT angiography images (Supply, 2010). Flow topology investigations and wall-shear-stress distribution can be successfully conducted in these models. In-depth studies that reveal the complexity of hemodynamics in aneurysms require patient-derived geometries (Geoghegan et al. 2012). Vortex core lines are usually computed and visualized to understand aneurysms (Roloff *et al.*, 2013; Nair *et al.*, 2016). The relationship between aneurysm progression and hemodynamics still requires a fair amount of investigations. In most existing studies, the analysis of the WSS distributions becomes the focal point for deducing the mechanism of aneurysm evolution (Mulder *et al.*, 2009; Aparício, Thompson and Watton, 2016). Hemodynamic studies also give insights into the effect of the flow development. In an experimental study, Trager *et al.*, (2009) examined the correlation between angiography and PIV quantifications of flow diverters in an in vitro model of elastase-induced rabbit aneurysms. In a computational study, Kim *et al.*, (2008) compared two stents in an attempt to modify cerebral aneurysm hemodynamics in order to treat aneurysms. They had observed that stents were useful in slowing or even stopping the growth of aneurysms, but there was a general lack of quantitative evaluation of how specific design features of endovascular stents (struts, mesh design, porosity) affect the hemodynamics in intracranial aneurysms. They investigated how these stents modify hemodynamic parameters such as aneurysmal inflow rate, stasis, and wall shear stress, and how such changes are related to the specific designs. They found that the flow damping effect of stents and resulting aneurysmal stasis and wall shear stress are strongly influenced by stent porosity, strut design, and mesh shape. They also confirmed that the damping effect is significantly reduced at higher vessel curvatures, which indicates limited practicality

of high-porosity stents as a stand-alone treatment. They also showed that the stasis-inducing performance of stents in 3D geometries could be predicted from the hydraulic resistance of their flat mesh screens. From this, they propose a methodology to compare cost-effectively different stent designs before running a full 3D numerical simulation.

Understanding the effect of hemodynamics is important in order to improve diagnosis and treatment of cerebral aneurysms (Ku, 1997; Le, Borazjani and Sotiropoulos, 2010). Current treatments target the reduction of blood circulation in aneurysms, resulting in thrombus formation within the aneurysm sac. In addition to the development of experimental and computational tools for the study of hemodynamics in cerebral aneurysms, much focus has been placed on techniques that model thrombosis. This provides an additional metric for examining aneurysm stability (Ngoepe and Ventikos, 2016). In most cases both tools (PIV and CFD) are used conjointly to validate CFD results. Improved understanding of the mechanisms at play will result in better therapeutic approaches.

1.5. Focusing on experimental techniques: PIV and flow phantom fabrication

As described in the preceding section, experimental techniques are used to study fluid flows in aneurysms. The approaches used are the same as those used in other low speed fluid mechanics applications. Earlier techniques of flow measurement required insertion of a physical probe in the flow itself. Pilot-static tubes is one of the earliest velocity measuring tools in fluid flow. In the 1920s, hot-wire anemometry was introduced and was later used to measure multiple velocity components. With the invention of the laser in the 1960s and the development of laser-doppler anemometry, non-intrusive velocity measurements were made possible with the use of a laser probe. Particle Image velocimetry PIV is a more recent non-intrusive tool for fluid flow measurement based on flow visualization. With the advent of image digitization methods and image processing software, the identification of changes in flow over time is made possible. This enables researchers to obtain valuable quantitative data on the flow field. Particle Image Velocimetry (PIV) is one of the most effective techniques used today for in-vitro blood flow measurements, with velocity field and wall shear stress (WSS) being the most studied physical quantities.

A PIV experimental setup system consist of a combination of electronic components, piping networks, computer hardware, software, algorithms and a transparent flow phantom. The method generally makes use of an algorithm to determine the displacement of particles seeded in the flow illuminated using a laser on images captured using a high-speed camera. A pair of images is captured, with the timing of capture being synchronized to that of light pulse (laser), with known time interval between the image pair. A set of pairs of images is recorded over a short period. These images are then processed using an algorithm to compute velocity values and their derivatives.

A flow phantom is an essential part of the flow setup in PIV flow measurements for several reasons; one of the reasons is that it replicates the geometry of the artery that needs to be investigated. The other reason is that it enables visual access to the stream of the flowing fluid. For this reason, the flow phantom has to be transparent and made from a clear material in order to provide the optical access required for PIV measurements. The fabrication technique to make a flow phantom thus becomes an important step. The common method of flow manufacturing still makes use of investment casting of clear silicone shown in the figure 1 below (Geoghegan et al. 2012).

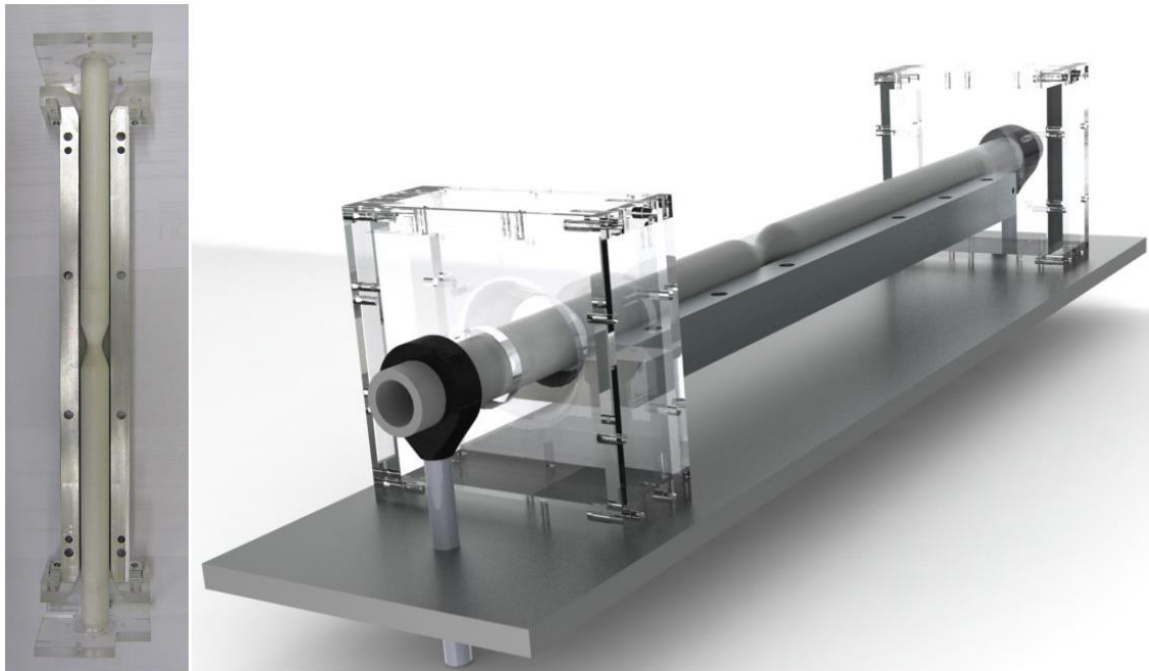


Figure 1 Fabrication of a flow phantom in investment casting (image by Geoghegan et al. 2012)

Today 3D printing has made noticeable advances in the layering techniques as well as the use of varieties of materials. After the introduction of fused deposition modelling (FDM) in 2000s, 3D printing gained much used in desktop configuration. Stereolithography (SLA) followed FDM and made it possible to improve the print resolution and increased the range of print materials. SLA is based on vat photopolymerization technologies. The building process uses a light source such as UV laser to cure photopolymer plastic resin in a liquid state into solid state by tracing the geometries profiles of the designed product with higher accuracy. Various clear materials have been developed to suit some applications for various industries and some of these are have optical properties that are suitable for PIV applications.

1.6. Goal of the study

1.6.1. Problem statement

Challenges still remain in the quest to understand the aneurysm evolution (Chen et al., 2014). There is a possibility that the growth and eventual outcome of aneurysms is linked to hemodynamic characteristics. Various computational models have been developed in an effort to better understand the mechanisms contributing to aneurysm growth, rupture and clotting. The main challenge with many of these models is that they have not been validated. In vitro experimental techniques can be used to validate computational results. This requires generation of experimental results of blood flow in aneurysms. In vivo experiments in humans are fairly difficult to conduct, therefore replication of in vivo conditions, via in vitro techniques, is desirable (Roloff et al., 2013). PIV is considered a competitive technique but requires construction of a flow phantom to the best accuracy possible.

Current manufacturing techniques for making flow phantoms still make use of investment casting, which is very laborious. Flow phantoms made from silicone material are usually of a lower refractive index, making it relatively easy to find a suitable working fluid. However, there are several inconveniences in this technique, the main one being the level of expertise required to build the model and the other being the possibility of entrapped air bubbles in the final piece, which may render the flow phantom unusable. Shrinkage is also a factor to consider during the curing stage. 3D printing poses an interesting alternative to traditional manufacturing techniques. 3D printers do not necessarily require extensive skills to operate and clear materials are still being developed. With 3D printing, it is now possible to produce a model directly from a CAD file. The use of a 3D printed phantom in hemodynamic PIV studies of cerebral aneurysms could be an interesting avenue that has not been extensively explored.

1.6.2. Aim of the study

The longer term goal of the overall study is to develop a computational and experimental model of thrombosis in cerebral aneurysms. The work presented in this thesis is a step towards that goal. The aim of this study, therefore, is to develop an experimental setup that can be used to validate an existing computational framework of blood flow in aneurysms, while implementing additive manufacturing (3D printing) to reproduce the test piece (flow phantom), which represents the geometry of the cerebral aneurysm of interest. SLA 3D printing technology will be used to produce the flow phantom representing an idealised cerebral aneurysm and PIV will be used to capture hemodynamics in that phantom. The results from this setup will be assessed, both in terms of the success of method implementation and of hemodynamic findings.

1.6.3. Project objectives

The first objective is to develop a flow setup capable of reproducing the hemodynamic conditions in actual arteries such as the aorta and cerebral arteries, maintaining dynamic similarity. The flow setup will be designed so that it can accommodate both steady state and pulsatile flow conditions. The steady state setup will be used to generate results, while the pulsatile configuration will be detailed for interest.

The second objective is to establish and evaluate the usability of additive manufacturing for the construction of a flow phantom that will replicate the geometries of an idealized cerebral aneurysm. This will be achieved by investigating available 3D printing technologies and materials for best results at a relatively low cost.

The third objective will be to conduct PIV measurements in the idealised cerebral aneurysm using the flow setup under steady state conditions. The PIV results have been used to validate CFD calculations on complementary work done at the University of Cape Town.

The objectives can be summarized as follows:

- To develop a flow setup capable of reproducing the hemodynamic conditions for both steady and unsteady pulsatile flow
- To develop a methodology for 3D printing of phantoms of aneurysm geometries
- Carry out PIV measurements of flow in models of idealised cerebral aneurysms

1.6.4. Scope and limitations

Cerebral aneurysms are a very complex disease, as evidenced by the amount of effort directed towards the study of this disease, by different disciplines. The methods developed in this study will not be able to address every aspect of cerebral aneurysm research. The focus of the study is on the development of low cost techniques that can elucidate some of the flow features associated with idealised cerebral aneurysms.

In vivo studies of aneurysms can either be can be intrusive or non-intrusive (Macleod *et al.*, 2015). These studies are conducted on living beings including animals, and in advanced clinical trials, humans. Non-invasive in-vivo techniques such as Doppler ultrasound and magnetic resonance imaging (MRI) can be used to measure the flow rate in blood vessels (Zöllner, 2014). The main limitation of these methods is their spatial and temporal resolution (Geoghegan et al. 2012). In contrast, *in vitro* studies are non-intrusive, making it possible to observe phenomena which might otherwise prove difficult *in vivo* as well as in a control environment and conditions. The limitation, of course, is that *in vitro* studies, based on techniques like PIV, may not mimic the natural state

accurately. Nonetheless, PIV has the capacity to provide interesting, detailed insights into flow conditions in a cerebral aneurysm model. This work will implement planar 2D PIV.

The wall of an artery is elastic by nature and expands to accommodate flow variation arising from pulsatility. This work will not use a compliant flow phantom, in part because of the lack of availability of a clear elastic material for 3D printing. Such materials are still under development and have not yet proven to have properties that match those of realistic vessels (Tamer et al. 2011). As a starting point, a rigid model printed out of transparent resin will be used. 3D printing of clear material in PIV is relatively novel. Some studies have indicated that pressure variation across the wall differs slightly in the case of a rigid wall when compared to the flexible wall, and especially around the aneurysm region (Xu *et al.* (2016)). An investigation into the effect of flow phantom properties will be the subject of future work.

In this work we will not consider blood as a non-Newtonian fluid in order to find a suitable working fluid substitute. Viscosity is an important physical property which characterizes the resistance to flow. A Newtonian fluid has a constant ratio between the shear stress and the shear rate at a given temperature. This implies that the viscosity remains constant, regardless of how fast the liquid flows through the flow channels. Non-Newtonian fluids behave differently, the relation between shear stress and shear rate is non-linear. Viscosity is dependent on shear rate and blood is an example of a non-Newtonian fluid. Blood viscosity determines the ability of blood to flow through the blood vessels and the work required from the heart to overcome these viscous forces. Blood viscosity can be measured for serum or plasma, without accounting for platelets and blood cells. This makes a good approximation to Newtonian fluid behaviour. The measurement of whole blood is complex, due to the blood cell deformability and red blood cells aggregation. This is in part due to shear rate variation, intermolecular forces, pressure variation and a host of other factors, such as immune complexes and stickiness of platelets (Anton-Paar, 2000). Several studies have shown that blood viscosity becomes more or less constant at a higher shear rate value (Geoghegan et al. 2012). The average shear rate is greater than 100 s^{-1} in in-vivo condition at the Reynolds number considered in this study which has an upper value of 106 and a lower value of 84.80. At this shear rate the viscosity is constant, this is our basis for applying a Newtonian assumption to blood.

1.7. Thesis outline

In the next chapters, chapter 2 will present the literature review, which will elaborate on the link between previous works and this present work. The methodology is detailed in Chapters 3, 4 and 5. The former provides details relating to the in-vitro experimental setup used in this work while the second discusses the implementation of 3D printing as method for flow phantom fabrication and chapter 5 presents details relating to PIV measurements and image processing. Chapter 6 presents results and analysis. Chapter 7 will provide a conclusion to this thesis and discuss possible opportunities to explore in future work.

2.1. Classification and identification of aneurysms

2.1.1. Classification of aneurysms

Aneurysms can occur in most parts of the circulatory system, though there seem to be no reported cases of aneurysms in veins. Some common places include aneurysms of the Circle of Willis in the brain and aortic aneurysms that affect the thoracic aorta and abdominal aorta as shown in the figure 2 below (Krings, *et al.*, 2011).

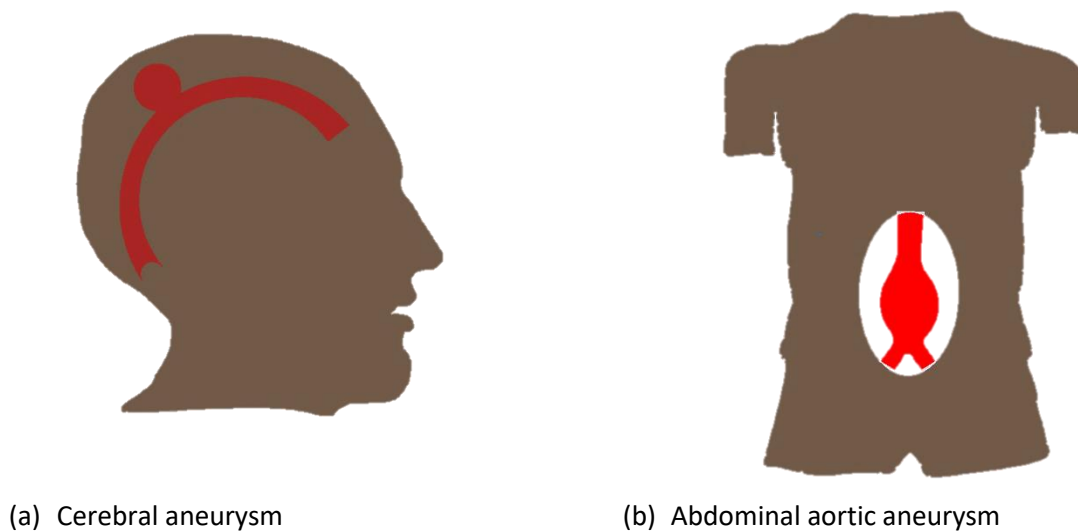


Figure 2 description of Aneurysms (a) Cerebral aneurysm and (b) Abdominal aortic aneurysm

Cerebral aneurysms have direct effects on the brain (Mulder *et al.* 2009). When blood gets in contact with brain matter, it impairs certain functional capacities of the brain, such as regulation of blood pressure and control of memory. When the blood leaks out of the aneurysm, it forms a clot called a hematoma inside the brain (Berg *et al.* 2014). At this stage the patient will experience some discomfort. Hydrocephalus is a case where blood fills open spaces inside the brain, building pressure on the brain tissues and causing the victim to become lethargic. Stroke usually happens in a case of vasospasm, when leaked blood eventually narrows cerebral arteries. This usually happens within 14 days from the time of rupture (Wolfe *et al.* 2006). An image of aneurysms on blood vessels in the brain is shown in the figure 3 below.

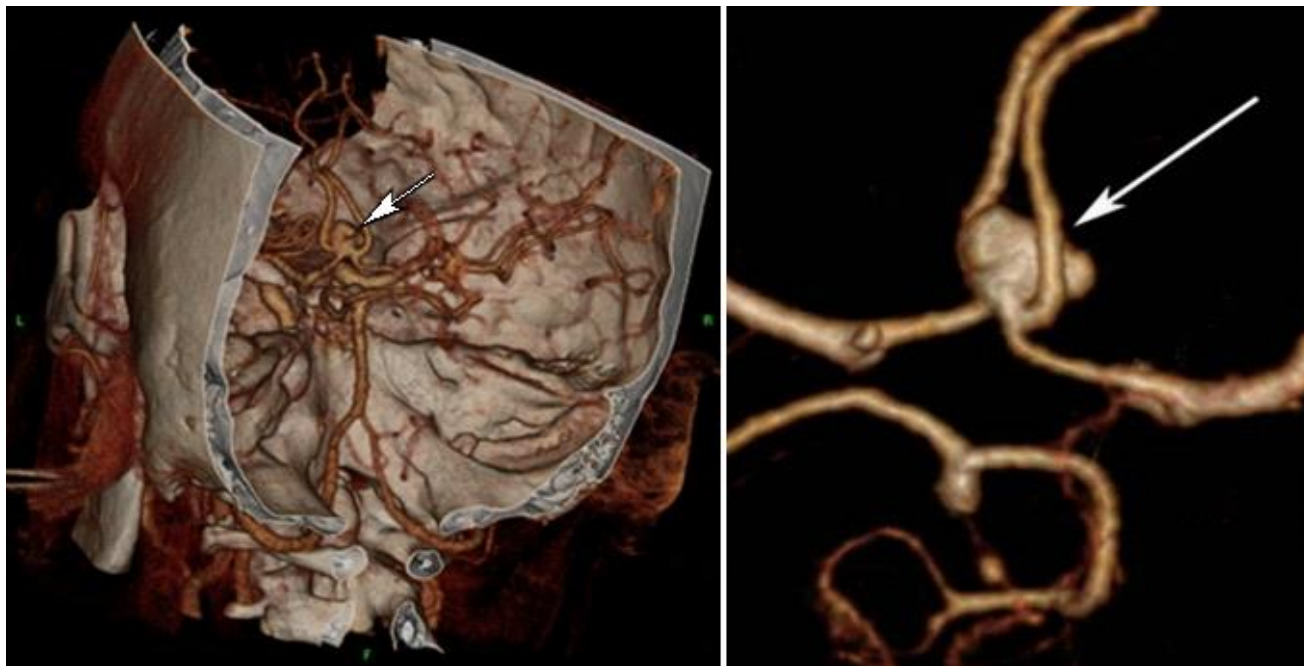


Figure 3 typical image of blood vessels around the brain/ Wikipedia common

The most common classification of cerebral aneurysms is based on shape and size. Aneurysms were classified as either saccular or fusiform and in addition to that, as giant or mycotic, the latter being quite rare (Tran, 2004). A saccular aneurysm is spherical in shape on a distinguished, localized part of the vessel wall. The size can vary from a few millimeters to about five centimeters, and some contain a thrombus (Krings *et al.* 2011). Fusiform aneurysms are sometimes referred to as spindle-shaped aneurysms and show wide variation in length and diameter. The UCAS Japan, (2012) showed evidence that aneurysm rupture is often fatal. A cerebral aneurysm may be accompanied by symptoms when its size is increasing and when ruptured. Cerebral aneurysms were found to have a strong occurrence in women in the Western world (The UCAS Japan, 2012). The UCAS Japan (2012) states that aneurysms are often associated with medical conditions such as atherosclerosis, syphilis as well as copper deficiency. In addition, Krings *et al.* (2011) discussed aneurysms resulting from immunodeficiency. According to their report, HIV patients (and especially children) develop multifocal, fusiform aneurysms in large arteries of the Circle of Willis.

2.1.2. Identification of cerebral aneurysms

As the cerebral aneurysm grows in size, it exerts pressure on surrounding brain matter, which in turn may result in severe sudden headache (esculap Neurosurgery, 2012). This is usually the first apparent symptom of a brain aneurysm. Further examination is usually required to confirm the presence of an aneurysm. A computed tomographic (CT) scan is such an examination tool. It generates the image of the brain and enables identification through visual inspection. In some circumstances, CT angiography is performed to reproduce a 3D image of the blood vessels (Wolfe *et al.* 2006). In addition to the CT scan, the spinal tap (lumber puncture) is used to extract cerebrospinal fluid (CSF), which flows in the brain as well as in the spinal cord. Through careful

examination of the CSF, blood may be identified, and this may suggest the existence of a ruptured blood vessel in the brain. The spinal tap usually extracts CSF from the lower spine using a needle. A special contrast dye can be injected into the brain arteries to determine the physical size and location of aneurysms, using an arteriogram.

It is apparent that even though we cannot currently predict the aneurysm progression, it is still possible to detect ruptured and unruptured aneurysms using x-ray scans, which can expose the patient to further radiation. In countries with lower income, it is even more difficult to detect aneurysms due to the cost of intervention and availability of expertise to conduct such operations (Sheppard et al. 2012). The complexity relating to aneurysms, from their origin to rupture, raises a number of concerns that need to be addressed.

2. 2. Effect of hemodynamics on aneurysm growth, rupture and clotting

While the origin of aneurysms seems to remain a tough subject, it is ostensible that the growth of aneurysms could be related to the hemodynamics developed inside aneurysms and the rate of change in the mechanical properties of the sheared wall vessel. Yasuda *et al.* (2011) investigated the risk of rupture associated with the growth of an aneurysm, as many others have investigated, but it remains unclear how the wall weakens. There is lack of clarity about whether the wall weakens from the interior of the vessel or from the exterior, and how much variables such as the presence of a clot mass contribute to the weakening of the bulge (Medero *et al.*, 2017). The key questions that many studies focus on relate to the link between aneurysm evolution and local hemodynamics.

Packet, (2006) claims that blood flow in the brain must be kept constant at all times in order for the brain to have any activity. 750 ml/min is considered to be the normal cerebral blood flow rate and the brain automatically regulates the flow rate to maintain it at a constant amount, regardless of blood pressure variations. To achieve this, the cerebral blood vessels undergo vasodilatation or vasoconstriction. Cerebral arteries are connected together by the circle of Willis, which serves as a regulator mechanism of blood flow and is able to momentarily shut down one side of the brain supply in order to ensure protection of the brain's functions (Wolfe et al 2006). Aneurysms frequently occur in this cerebral region, therefore the assumption that hemodynamics play a major role in the development of aneurysms is a sound one.

Cerebral blood pressure, together with cerebrovascular resistance, has a direct effect on cerebral blood flow. The pulsatility of blood flow is directly proportional to the cerebrovascular resistance and indirectly proportional to blood velocity. As a result, blood is expected to slow down and have a strong pulse when an obstruction is encountered (Packet, 2006). Blood flow is equally altered by some intrinsic factors such as the viscosity of blood and the cardiac output. Blood flow can also be altered by some extrinsic factors such as the intracranial pressure, the oxygen content and the carbon dioxide content. Higher content of carbon dioxide in

the blood vessels will result in the dilatation of the vessels. This vasodilatation, in turn, will increase cerebral blood flow.

In addition to the abovementioned factors, which have a direct impact on cerebral blood flow, there are other variables which also affect cerebral blood flow. For example, rapid eye movement sleep behaviour disorder and arousal both affect cerebral blood flow (Yazici, Erdoğan and Tugay, 2005). Cerebral trauma and body temperatures are also factors considered to have a direct effect on the cerebral blood flow regulatory system.

As mentioned earlier, victims of aneurysms are often not aware of the defective blood vessels until symptoms start to appear. By the time symptoms appear, most aneurysms are either about to rupture or have already ruptured (Xu *et al.*, 2016). A ruptured aneurysm often leads to internal bleeding or haemorrhage. Thrombosis (clot formation) is often associated with aneurysms (Sheppard, 2012). In a case where a clot detaches from the aneurysm and gets carried away in the blood supply system, it exposes the victim to greater risk of stroke. Thrombosis-associated hemodynamics of carotid artery bifurcation has also been a subject of many investigations and suggests that turbulent and transitional flows are often present in aneurysms (Mulder *et al.*, 2009). Nair *et al.*, (2016) conducted an interesting study, which investigated the wall shear stress on a growing aneurysm of a specific patient over a period of 27 months, by comparing the different geometries at different time points the result was not conclusive. In Japan, an investigation was conducted to identify the natural history of unruptured cerebral aneurysms (The UCAS Japan 2012). From January 2001 through April 2004, patients were enrolled with newly identified, unruptured cerebral aneurysms. Information about the rupture of aneurysms, deaths and the results of periodic follow-up examinations were recorded. The study included 5720 patients who were 20 years of age or older (mean age, 62.5 years; 68% women), presenting with saccular aneurysms that were 3 mm or more, and whom initially presented with no more than a minor disability. This study showed that the natural course of unruptured cerebral aneurysms varies according to the size, location and shape of the aneurysm. The results obtained in most studies thus far show an association between hemodynamics, and aneurysm initiation and growth, but do not necessarily prove causality.

2. 3. Computational approaches for solution of biofluid flow problems

Most studies that have been conducted to understand aneurysm development needed to adopt a non-intrusive approach, so that risks associated with physical intervention on the brain could be avoided. With advances in computer technology, computational fluid dynamics (CFD) is becoming a powerful tool to simulate practical fluid mechanics case (Tamer, Hassan & Yasser, 2011).

CFD is a computer based approach that conducts numerical solution of fluid flow problems. With advances in computer speed and memory, CFD solves various flow problems such as compressible, incompressible, turbulent, and laminar, chemically reactant, single phase as well as multi-phase flows. Finite-difference

methods (FDMs) and finite-volume methods (FVMs) are numerical methods commonly used for equations that govern fluid-flow problems (Xu *et al.*, 2016).

The use of appropriate governing equations and numerical recipes is always critical for obtaining accurate solutions. The initial conditions usually affect the processing speed while the boundary conditions are important factors that directly influence the accuracy of results. Even though CFD is a powerful technique for solving fluid-flow problems, the user should be able to understand the physics of the fluid-flow problem being solved, and the user should also be able to interpret results effectively.

The solutions obtained from CFD results need to be validated. This is mainly due to assumptions made in the boundary conditions. Among the validation tools, there are theoretical solutions as well as experimental solutions which help with verification and validation of the solution of complex fluid flow problems.

Hemodynamics is mainly concerned with the flow of blood. In the case of aneurysms, physical data of blood flow can provide clarity and identify factors that are most influential. In-vitro study is a relatively safe option to generate these data which can, in turn, be used for diagnosis and further computational simulation of aneurysms per specific patient (Ngoepe *et al.*, 2018).

Extensive work has been done on cerebral aneurysms using CFD. Tamer, Hassan & Yasser (2011) studied the effect of flow diverters on flow patterns in saccular aneurysms, using CFD. The flow diverters are similar to stents but are less porous and are used in endovascular intervention to treat cerebral aneurysms. A numerical simulation was conducted for three different stent models. The results show an increase in the circumferential pressure distributed on the wall of the aneurysm. According to the report, these results proved that the use of stents could be dangerous and could, in some instances, increase the risk of rupture (Tamer, Hassan & Yasser, 2011).

Many studies of cerebral aneurysms are conducted using both a numerical approach and experimental studies to validate results. Xu *et al.* (2016), conducted numerical studies to verify experimental research regarding cerebral aneurysms with a compliant wall. The results showed that wall shear stress was different when compared to rigid wall models. The peak value of the average shear stress was reduced in the case of the elastic wall model.

Ford *et al.* (2008) conducted a numerical study in anatomically realistic cerebral aneurysm geometries. This approach enables better understanding of the factors at play in an aneurysm's growth, using a patient specific model. PIV was used to provide input values for CFD and results were compared. There was good agreement in the velocity field vectors of both experimental and numerical studies. Owing to assumptions made in order to conduct CFD studies, there was no certainty that results would match in vivo hemodynamics accurately, and

it was suggested that in vivo data could be used for validation. It is important to note that CFD on its own still bears a number of limitations and that validation, usually conducted in experimental work, is always important.

2.4. Experimental studies

Computed tomography (CT) scans are one of the most popular tools used in the diagnosis of aneurysms and generation of 3D images of a patient's vasculature. These images can reveal information about the flow field (in the case of CT angiography) and other physical quantities, such as aneurysm shape and size.

PIV is a fluid mechanics tool for fluid flow measurement. This is flow visualization technique is usually conducted in transparent flow media (Potter et al., 2015). The method consists of a pulsed light source (e.g. laser) that illuminates small fluid-entrained particles over a short period of time exposure. The technique records image frames and uses an algorithm to generate velocity vectors based on a statistical average of the displacement of groups of particles within a particular interrogation area, from one image to another within a frame. More details are provided in the following chapter.

Several reports have used , this technique to obtain velocity data from image processing using an algorithm (Jahanmiri et al., 2011). When processed, instantaneous velocity measurements and related properties in the working fluid are obtained. In this technique, the motion of the fluid needs to be visualized (e.g. through a high-speed camera) and for this particular reason, the fluid has to be seeded with tracer particles, which are very small in size and must follow the flow to the best accuracy. The degree by which this happens can be determined by the Stokes number. When illuminated by a laser, the motion of the particles can be captured and used to calculate speed and direction of the flow under investigation, inside a transparent phantom.

The PIV system usually consists of a laser (light source), camera (digital CCD being the most commonly used) and a computer to visualize, store and process data. However, without proper matching of density between the working fluid and the tracer particles, there can be a noticeable error in the acquisition of flow field data, thus rendering the technique inadequate. The other constraints to the use of this technique are related to the high cost of PIV equipment and the safety issues associated with the manipulation of the equipment. For example, a Class IV laser can damage sight and lead to blindness when it passes the human eye. In addition, image distortion due to differences in refractive indices between the working fluid and the surround medium (the flow model) and the curvature of certain lenses can negatively affect the results. Despite these constraints, PIV is a powerful tool when properly used (Bouillot *et al.*, 2014).

2.4.1 Fabrication of the flow phantom

PIV experiments are conducted in transparent flow phantoms. Flow phantoms could be described as a scaled model that represents the geometry of interest (e.g. artery), which is connected to the flow circuit. Flow phantoms were traditionally constructed using investment casting methods (Geoghegan et al., 2012) with

Silicone being the most commonly used material. The process of making the phantom usually uses a set of moulds, one internal and the other external, while the silicone is poured in between to fill the cavities. After this, the phantom cures for few days at room temperature. To complete the task, dissolvent is usually required to melt-away the internal mould. When a model has many intricate internal surfaces, the task of removing the internal mould material could be very difficult. The complexity of this process requires adequate skill to achieve the best quality, both in terms of internal surface clarity and absence of air bubbles in the phantom during silicone solidification. In addition, this method requires a relatively long time to achieve the desired output, such as no shrinkage or uneven walls, to attain geometric and dynamic similarity as well as to avoid image distortion. The entire process could take an average of 2 weeks.

Jermy (2013) found that for internal flows, optical measurements (e.g. Laser Doppler Anemometry and PIV) work well if a flat window can be let into the walls of the system. The report shows that curved walls may lead to refractive distortions. While the correction for such distortion remains complex, he states that in order to meet the state of no optical distortion, the working fluid and transparent model must have the same refractive index (a mismatch of a few percent is acceptable except in cases where the very best image quality is required). For walls of simple configuration other than flat surfaces, for example cylindrical surfaces with a single radius of curvature, which is similar in magnitude to the distances between the components, the distortion may be corrected during post-processing. In other simple systems, it may be possible to orient the probe light and detector so that the small amount of distortion that occurs can be ignored. This means that whenever possible, the internal flow channels should be encapsulated by flat walls and be parallel to the image capturing plane. For rigid flow models, this is easily done but for elastic compliant model, other methods have to be employed.

In order to conduct an accurate PIV measurement, the following steps have been suggested by Jermy (2013):

- Flow phantom material and working fluid selection
- Construction of the flow phantom
- Dynamic similarity between in-vivo and in-vitro conditions
- Control of working temperature
- Fluid mixture control of density, kinematic viscosity and matching of refractive index.

For a successful experiment, several conditions must be reached. The refractive index must be matched between the phantom material and the working fluid. In most cases, the working fluid is a mixture, and therefore depends on the mixture fractions (e.g. salt or glycerol concentration). As a result, it is important that evaporation is prevented. Repeated checking of the refractive index match is suggested. The refractive index is also a function of the temperature, and this will require control of the working temperature. It may be convenient to operate the working fluid at a temperature slightly above or slightly below room temperature, so it can be thermostatically controlled with a heater or cooling loop. Another reason to carefully control

temperature is its effects on the viscosity of the working fluid, and hence the Reynolds number. Most index-matching experiments substitute the actual fluid (e.g. blood) with a working fluid that can be found in nature (e.g. air, water, and oil). When such replacement takes place, it is important to retain dynamic similarity of the flow. For fluid flow problems relating to liquids, which are virtually incompressible, the Mach number is low and need not be considered (Ku, 1997). The Reynolds number, however, must be matched, and is given by the Equation 1,

$$Re = \frac{\rho VD}{\mu}$$

With ρ representing the fluid density, V representing the instantaneous velocity of the fluid in motion, D is the diameter of the vessel and μ is the dynamic viscosity

2.4.2. 3D printing use in PIV

Song, Choi and Kim, (2013) investigated the use of 3D printing as a manufacturing technique in the field of optical flow measurements. This study's main interest was to quantify the optical properties and to compare transparency of prints and the refractive index matching of fluids. The refractive index at a wavelength of 532 nm, commonly used in PIV, was discussed for each 3D printing technology, Selective Layer Sintering (SLS) using VeroClear-RGD810, Stereolithography (SLA) using ClearVue and Vacuum casting base on the 3D printing master using epoxy and urethane plastic resins. SLA came up with higher transparent print compared to SLS but both prints were reported to have a refractive index of 1.51. Herb essential oils were mixed with light mineral oil, the matching index of refraction test was successful, and that opened the door to the use of 3D printing in PIV.

Another noticeable work using additive manufacturing techniques was reported by Aycock, Hariharan and Craven (2017), who conducted PIV measurements in an anatomical vascular model made from inkjet 3D printing. The work proved to be successful only at approximately 45° angle of print orientation, according to the report. The surfaces of the print needed wet-sanding using sandpaper in the range of P280 to P4000, then polished with a polishing compound "NOVUS Plastic Polish No.2 for the best surface finish. To match the refractive index, the working fluid was composed of 53% sodium iodide (NaI), 26% glycerol, and 21% distilled water by weight. The working fluid's refractive index was measured to be 1.5063. The model's transparency was reported to be good enough during PIV measurements and blurring of experimental images was not noticeable.

A 3D printed model is potentially a very good method of directly producing a phantom model for PIV studies. A few attempts have already proven to be a good option, but the limited availability of such optically transparent materials for 3D printers sets limits to the implementation of this manufacturing technique

currently (Jermy, 2013). In addition, to make the experiment closer to reality and to ensure a successful set-up, it is important to use appropriate materials for the working fluid. There is not enough work reported to identify specific fluids and mixtures. The choice between a steady flow study (Yu *et al.*, 2012) or a realistic transient flow study approach has not been much discussed, though it is generally accepted that steady flow is a good simplified approach for cerebral aneurysms and it should be expected that steady flow will miss the transient nature of cerebral arterial flow (Yu *et al.*, 2012).

The table 1 lists available transparent materials for selection with their refractive index values. The list is adapted from the work by Jermy, (2013).

Table 1 list of available transparent material

Solid materials (flow phantom material)		
Glass	Fused quartz	1.4584
	Optical glasses	1.45-1.96
	Borosilicate/aluminosilicate	1.47-1.49
Polymers	Fluorinated ethylene propylene	1.33
	Acrylic	1.47-1.49
	Polycarbonate	1.58
Resin materials		
Urethane based		1.49
Acrylic based		1.49-1.53
Silicone elastomer		1.415-1.47
Epoxy based (stereolithography)		1.56
Liquid materials (working fluid)		
Aqueous solutions	Water	1.33
	Glycerin	1.33-1.47
	Zinc iodide	1.33-1.62
	Sodium iodide	1.33-1.5
	Ammonium thiocyanate	1.33-1.50
Organic liquids	Tung oil	1.52
	Cassia oil	1.60
	Benzyl Alcohol	1.54
Powder based (mixing with fluids to get a working fluid)		
Ammonium thiocyanate		1.685

In addition to the refractive index value, it is important to consider the clarity, density and viscosity of the selected working fluid. This is because a fluid too dark may make it difficult to conduct RI match test, and a fluid too dense or too light may not find a compatible mixing fluid. A fluid that is too viscous may require a powerful pump and a higher head for the fluid to get through the flow loop. To create the required working fluid, it is common practice to mix different materials; therefore compatibility is also an important aspect to consider during selection of the base fluid and the mixing component.

Table 2 Challenges in the field of aneurysm studies

Most reported problems dealing with aneurysm	Tool used to investigate problems	Challenges that still need to be addressed
Changes in mechanical properties of the sheared wall vessel	Computational and experimental	Needs further validation
Risk of rupture	Statistical studies conducted on victims, CFD, experimental	No available material to replicate artery's mechanical properties
Thrombosis associated hemodynamics	CFD	Needs further validations

From the table 2 above, it is evident that a flow phantom model is critical in order to enable flow-related experimental studies of aneurysms. Other methods of producing a flow phantom are still required and need to be investigated. It is also important to further analyze experimental results in order to identify key factors that affect the hemodynamic characteristics and clot formation inside aneurysms.

2.5. Conclusion

This chapter started with a description of aneurysms and their symptoms. It demonstrated that aneurysm has been a subject of many studies and still is a subject that is not well understood. The growing aneurysm is subjected to possibilities of rupture or clotting at some point. The link between the hemodynamics and the evolution of aneurysms is a challenge that needs to be explored in order to provide more insight on the factors that contribute to its growth. Various treatments are still being improved for both ruptured and unruptured aneurysms with the intent to stop blood from entering the aneurysm. CFD is a growing tool used to study blood flow in aneurysm, validation is usually required in CFD by using experimental alternatives. PIV is one of the most acceptable non-intrusive in-vitro experimental measurement techniques and will be used to study fluid flow in aneurysms in this work. One of the challenges that PIV is facing is the laborious manufacturing process of the flow phantom, the actual investment casting techniques is laborious and requires extensive skills. Part of the work detailed in this thesis will address this challenge in a particular manner by identifying alternative additive manufacturing techniques and particularly 3D printing while implementing it to make flow phantoms suitable for PIV experiments. In the next chapters, the in-vitro experimental setup is discussed in details and the fabrication of the phantom by 3D printing will be discussed in much details in chapter 4.

CHAPTER 3: IN VITRO EXPERIMENTAL SETUP

3.1. Introduction

In this chapter, the flow setup for the in-vitro setup used in this experimental work is described. The flow setup was built in such a way that it can accommodate both steady and pulsatile flow conditions. A brief description of the pulsatile flow configuration is given in this chapter. It demonstrates a possibility to achieve continuous controlled pulses using a stepper motor and a screw valve at low cost. Figure 4 below describes the mechanical interpretation of the cardiovascular system, in order to build a similar in-vitro setup.

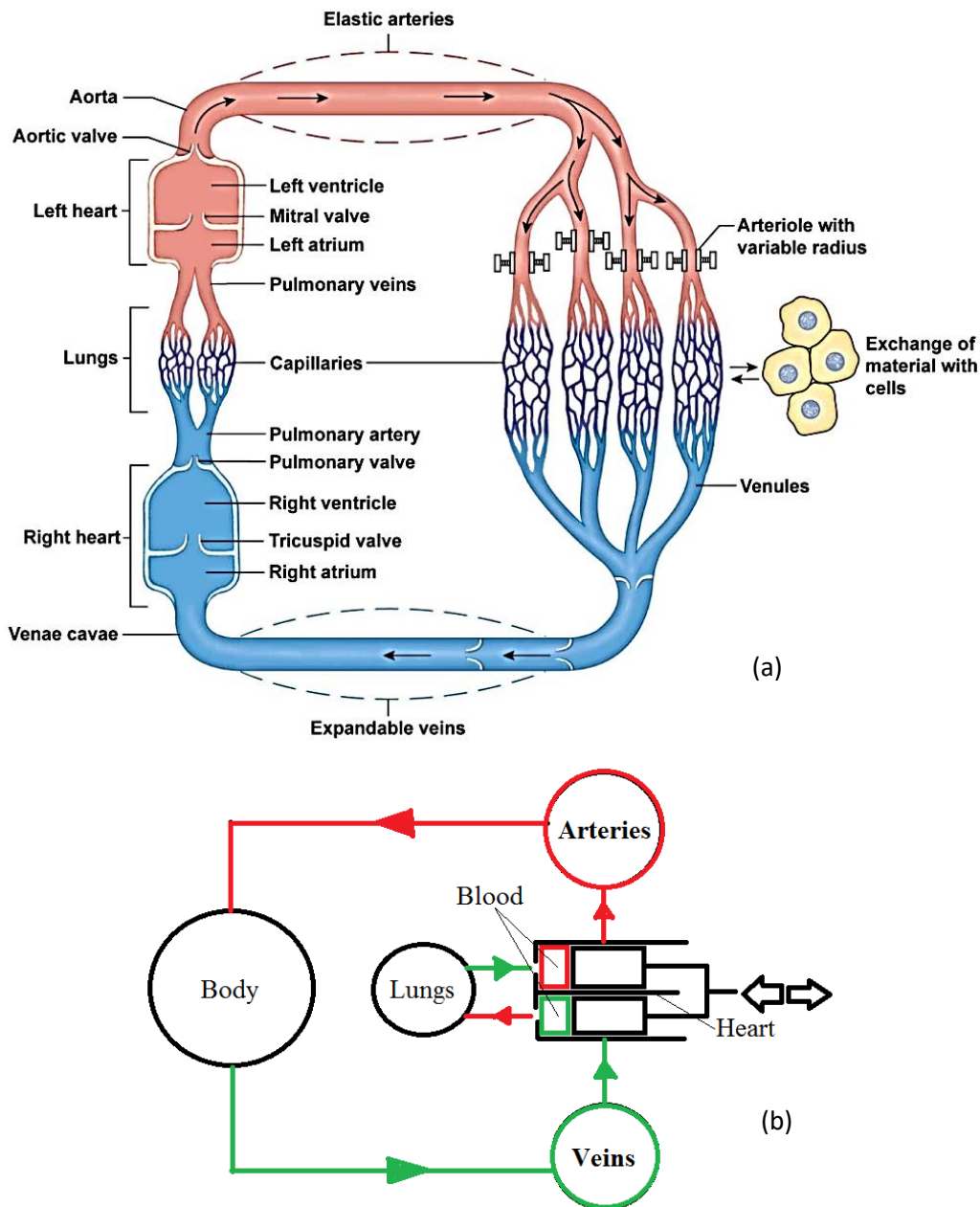


Figure 4: Mechanical interpretation of the cardiovascular system. (a) Representing the actual cardiovascular system and (b) representing the mechanical interpretation

3.2. Flow setup

A few assumptions are usually made when conducting experimental studies. The most important ones, in this study, are in the substitute for the human heart and the substitute for the arteries of interest. For most experiment, it is generally acceptable to consider steady flow as the first approach. Even though the heart pumps blood in a pulsatile fashion, the arteries of the brain have a reduced pulsatile effect, pulsatility decreases as a result of a decrease in cerebrovascular resistance due to a decrease in partial pressure of carbon dioxide in blood in arterial flow PaCO_2 (Packet, 2006). The other noticeable assumption is the use of rigid flow phantoms, while real arteries are compliant in nature. Most of these assumptions are influenced by the availability of materials that are used to make models, in order to substitute biological organs. Figure 5 below represent the schematic of the experimental setup used in this work.

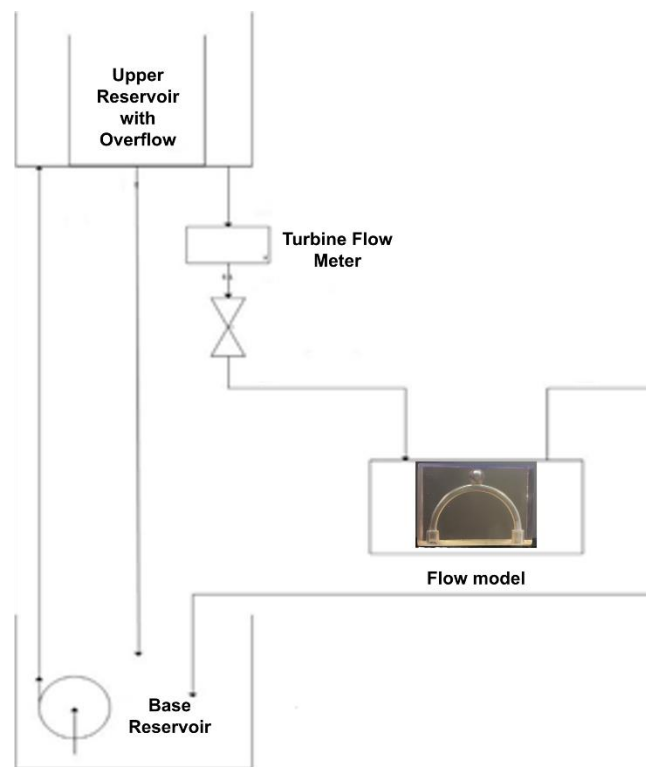


Figure 5: Schematic view of the experimental setup

In this work, a flow setup similar to the one used by Buchmann (2010) was considered and simplified. The flow circuit is constructed with two reservoirs, a lower reservoir and upper reservoir at a height above the flow model. The upper reservoir contains an overflow tube which serves to provide a fixed and constant head above the flow model for steady state conditions to be met. The lower reservoir contains a submersible pump and supplies the working fluid to the upper tank. The flow meter is fitted between the upper tank and the test piece in order to monitor the flow and to achieve the required velocity. Past the flowmeter and before the

phantom is a valve which controls the flow rate and was 3D printed. Details of this valve are provided in the following section. The flow path begins from the lower reservoir and is pumped to the upper reservoir (details of the pump to be found in Appendix C). The working fluid then passes the flow meter, the valve and the phantom. The working fluid then returns to the lower reservoir where the process resumes.

The PIV setup in this experiment was conceptualized, built and assembled in order to achieve the purpose of the study. Details about the frame design are given in the following section. The actual experimental setup is presented in the figure 6 below.

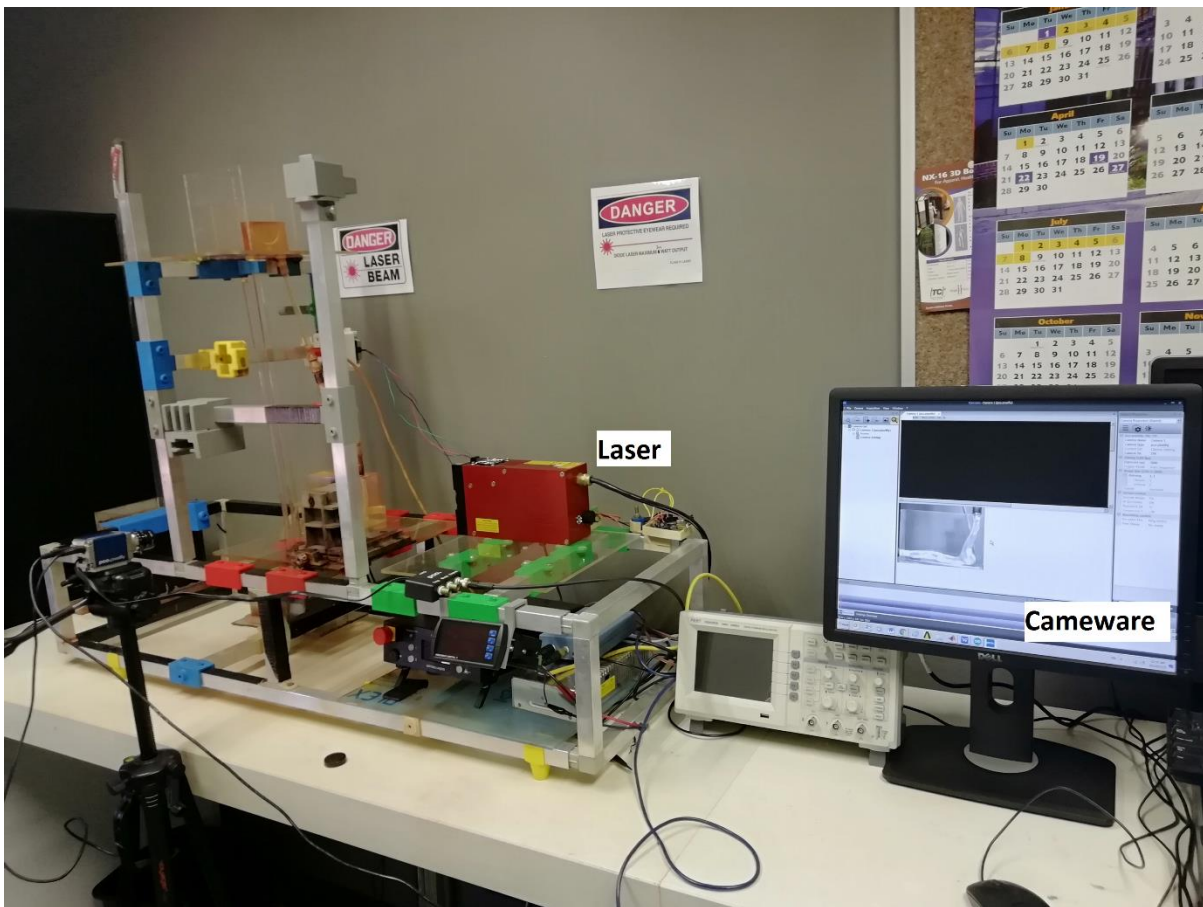


Figure 6 experimental setup is presented

The experimental setup was built and all accessories were attached to it. The laser and the flow phantom mountings were designed for two main purposes. The first purpose was to keep the laser and flow phantom at a right angle and the second purpose was to allow the flow model to move in-order to capture images at different planes within the model. Most fixtures in this setup were 3D printed using an FDM 3D printer from Makerbot. The following section will describe some of the devices and fixtures used in this setup.

3.3. Devices

The following devices were selected for the flow setup:

Pump: Water Lift Submersible Filtration Pump 44l/h, 220-240v/50 Hz, 5W, maximum Displacement Height: 0.8 m Minimum Height of Displacement: 400l/h at 0 m From SunSun.

Flow meter: Flow transmitter FT-210 ¼" NPT with Din, Nylon. Precision Digital Pro-Vu Universal Flow indicator 6 digit dual line red LED display fully customer programmable, supply: 220Vac, Input: Pulsed, open collector, contacts. Panel mounted: 96 x 48 mm, c/w 2 programmable alarm relays (rate or total + reset. From Transducers SA. The flow meter was selected based on the expected flow range. The expected inlet velocities range between 0.027 and 0.033 m/s resulting from dynamic similarity studies. In such a lower range of velocities there is a shortage of devices to read accurately the passing flow. This flow meter is a flow turbine sensor that generate an electrical signal or pulse for a specific rotation of the turbine sensor whose speed is proportional to the flow passing through it. The calibration of the flow meter and the reader was set to 22 000 pulses per liter. In order to monitor the flow rate, a digital data logger was connected to the flow meter. A picoScope from PICO Technology was used as the data logger. This registered the electrical signal pulses from the sensor and recorded the pulses over time, which can be converted into flow rate. More details on the flow meter are given in appendix D.

Piping and valve: Acrylic tubing of 10 mm and 6 mm inside diameter was used. The necessary flow restriction was controlled by a 3D printed screw valve, which can be manually set to achieve desired steady flow rate. The valve can also be controlled by a stepper motor connected to it. More details on the pulsatile configuration will be provided in the following section 3.4.

The scaffold was built with aluminum tubes connected together with 3D printed connectors. In Appendix G, a set of fixtures is presented. These fixtures were designed to fit the current setup, in order to provide more flexibility and usability of the equipment.

Keeping the flow phantom static during the experiment is important. The most straightforward approach was to 3D print the flow phantom mounting from a relatively cheap material. A fused deposition modelling (FDM) 3D printer was used to 3D print the model holder at lower cost. The flow phantom holder is one of the most important fixture that needed to be custom made. The fixture was printed from PLA filament and can be tightened to hold the model in place. In addition to the flow phantom mounting there are several other fixtures such as the stepper motor mounting and the screw valve as shown in Appendix G. The valve used in this work was particularly designed to fit the setup configuration. These fixtures were 3D printed from PLA filament. The flow restriction in the valve is controlled by squeezing or releasing a flexible tube passing through it as the screw is turned. If the screw is connected to a stepper motor, it could generate a pulse of a desired waveform.

More details will be presented later in this chapter. Other 3D printed fixtures include frame connectors and additional tubing shown in appendix G, most of which could not be easily sourced from local suppliers. This was done at lower cost and added more flexibility to the setup.

3.4. Pulsatile flow system

A steady flow profile is an acceptable approximation of the flow conditions, but pulsatile flow is more realistic. This section presents the approach to achieving pulsatile conditions for future work. It has to be noted that the pulsatile setup was not considered to produce PIV results presented in this work due to the time constrain. Through repetitive variation of the valve opening section, a pulse can be created. This is achieved through the use of a computer-controlled stepper motor connected to the screw valve described above, and could produce any desired flow profile. The system is illustrated in figure 7 below and was built at the fraction of the cost of available pulsatile pumps. Commonly used pulsatile pumps which are usually cylinder pumps driven by stepper motors are in the region of about R200K at the time of writing of this thesis. Hence a cheap alternative was attempted.

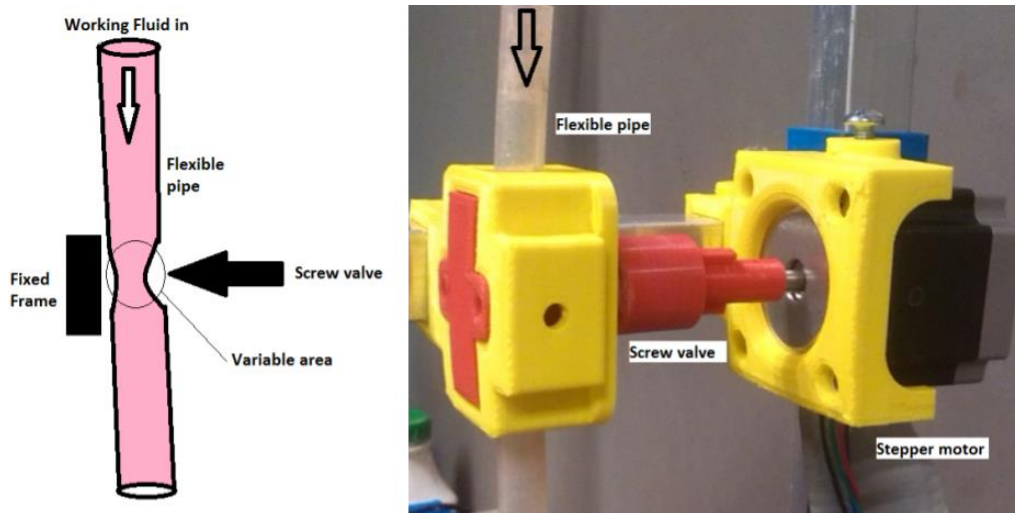


Figure 7 Stepper motor connected to the valve

3.4.1. Pulsatile system configuration

The pulsatile system, used in this work, comprises of the stepper motor and an Arduino board with details provided in appendix F which is connected to the screw valve described above. The connection between the Arduino board and the stepper motor is presented in the figure 8 below. The Arduino code was written so the stepper motor can rotate the screw valve with changing speed and be able to reverse the direction of rotation in intended sequences.

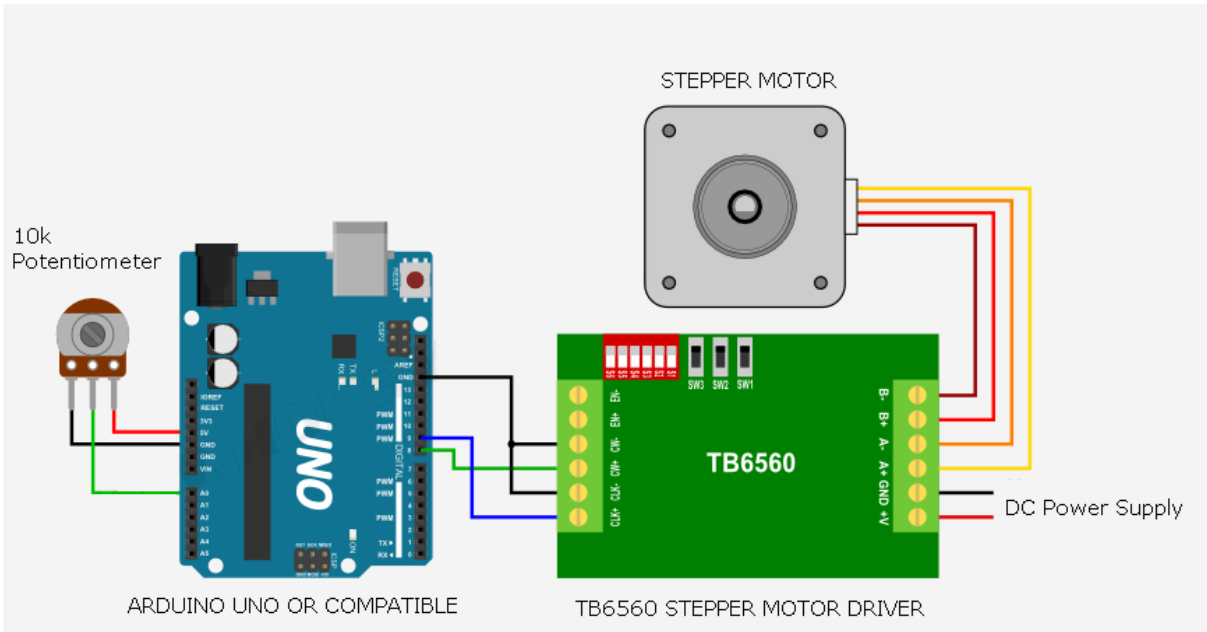


Figure 8 Stepper motor and Arduino board connection

3.4.2. Flow configuration

As there is no suitable instantaneous readout for the flow meter readily available, a picoScope which is essentially a digital oscilloscope was used to read out the signal from the flow sensor. The flow sensor produces a square wave of 0 and 5 volts. The period of the oscillation is a function of the flow rate. Figure 9 and 10 below shows the waveform for a steady and an unsteady flow. By measuring and plotting the period of each oscillation against time, we can then get flow rate vs time information.

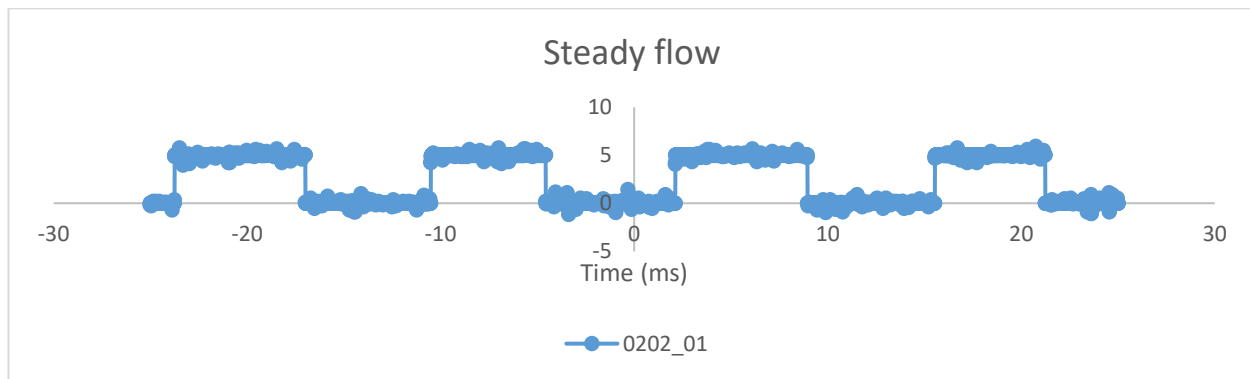


Figure 9 picoScope output from channel B for steady 0.202 l/min flow rate

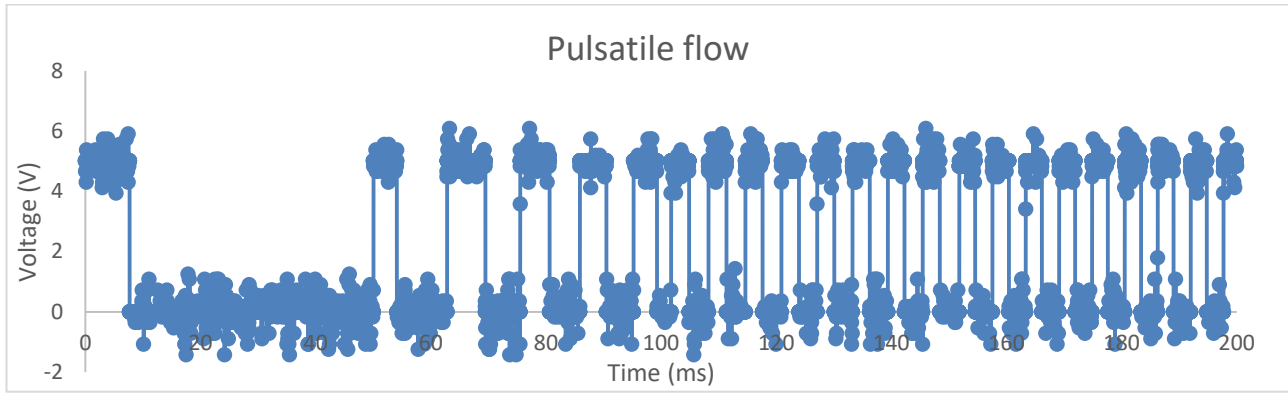


Figure 10 Pulsatile profile recorded with a picoScope

In order to the test the effectiveness of this valve, a simple sinusoidal waveform was used. The valve was first calibrated by varying the number of rotational steps for the stepper motor and the result is shown in Figure 11.

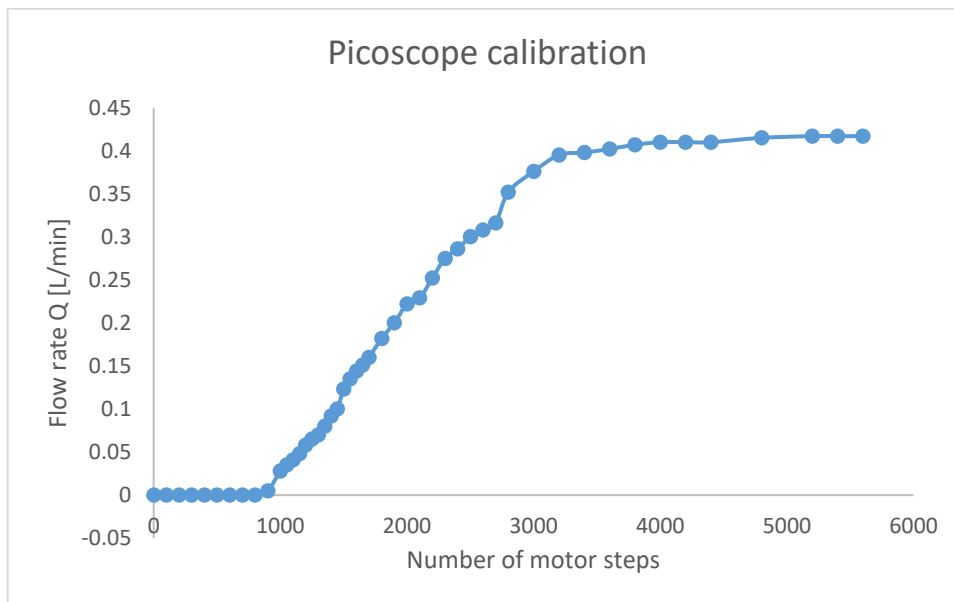


Figure 11 Valve calibration

Figure 12 below represents the simplified pulsatile flow profile that was used. Using the simplified flow profile, the stepper motor was programmed to rotate a specific number of turns in order to open and close the valve and to achieve the desired flow profile. A simplified Arduino code was used to this effect, to command the stepper motor to rotate with a specific direction and reverse with a very specific speed.

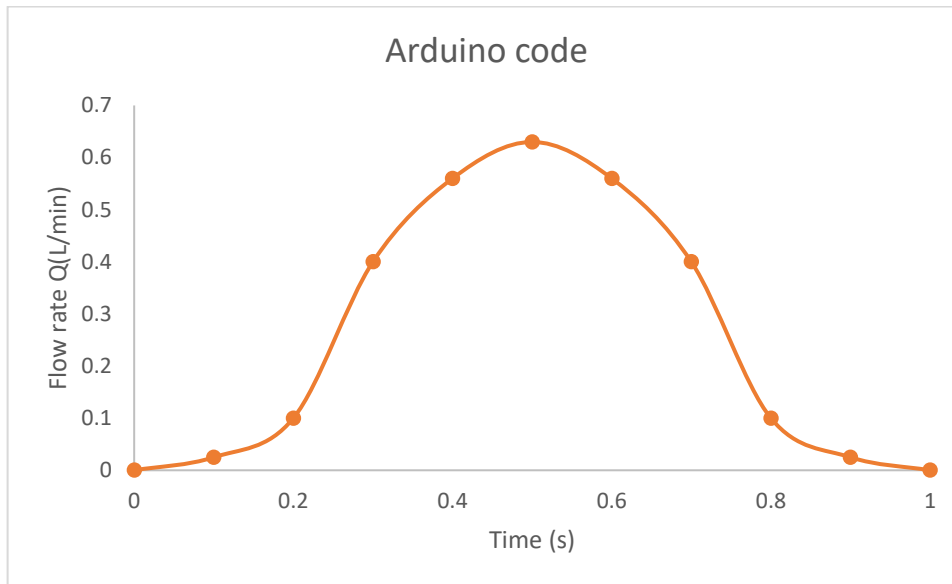


Figure 12 Stepper motor programming

The recorded flow was plotted and the resulting graph is shown in figure 13 and the error from the desired (Figure 12) in Figure 14. Although the waveform looks very different, this exercise indicates that a pulsatile flow can be represented in this way however further work needs to be done to refine the system including changing of the valve to other types of valves.

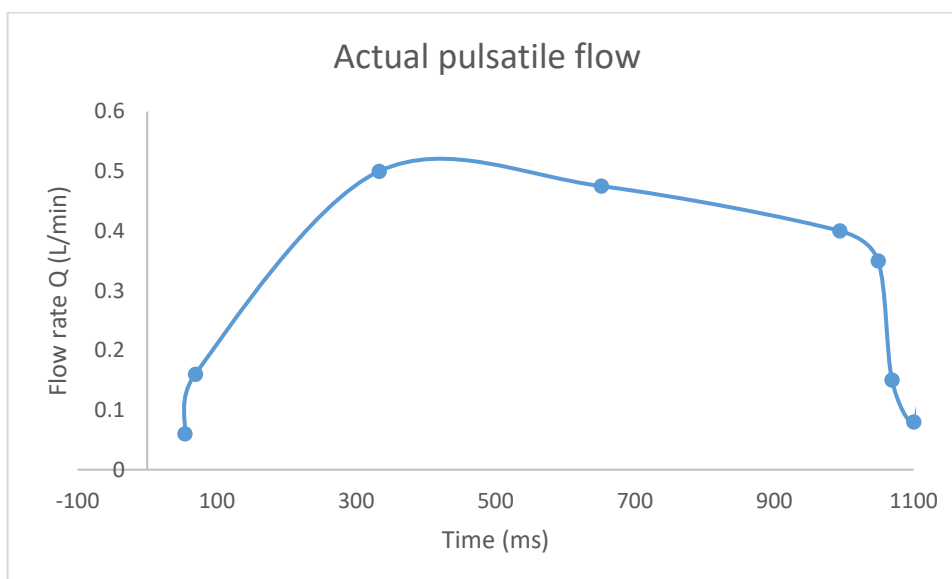


Figure 13 Actual flow rate recorded

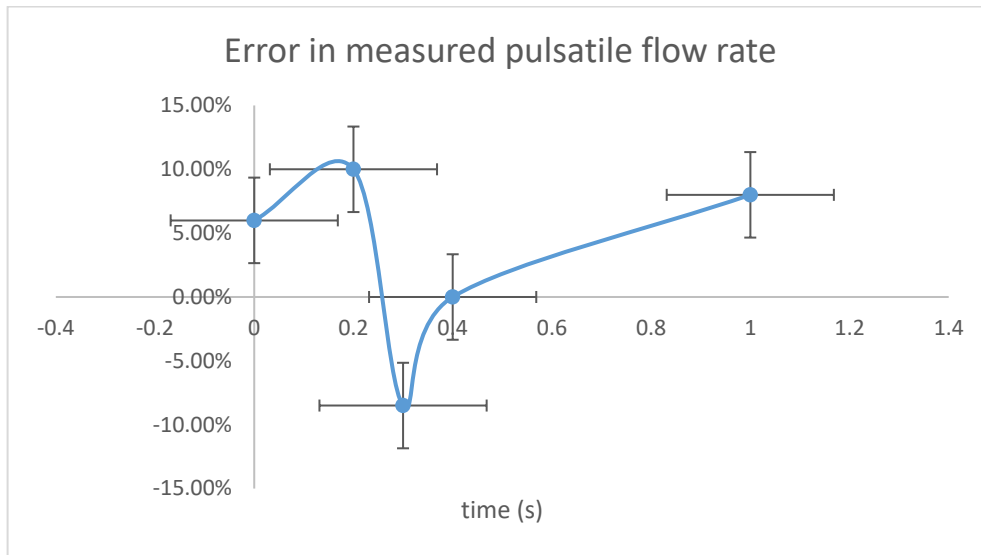


Figure 14 Percentage error after comparison of the expected and the actual flow profile

In this section, the pulsatile system was discussed. A stepper motor was used to control the screw valve that regulates the flow. An Arduino board controlled the stepper motor’s rotational speed and direction to produce the desired flow profile. The actual flow recorded show evidence of pulsatile flow conditions but further refinement of the Arduino code and the screw valve are still required to achieve better result and this will be done in future work.

3.5. Conclusion

This chapter provided a description of the flow setup used in this work. This chapter also discussed other important devices that are necessary for the PIV experiment. Finally, a proof of concept of a pulsatile flow system was presented. While this system is not used in any of the subsequent chapters, it demonstrated the potential expansion of the existing flow loop. Producing the flow phantom is a crucial stage in PIV experiment, and requires precision and accuracy in order avoid or reduce errors. The section detailing production of the flow phantom will be presented in the following chapter.

CHAPTER 4: FLOW PHANTOM FABRICATION

4.1. Introduction

Particle image velocimetry (PIV) relies heavily on the optical qualities of the flow phantom. In PIV experiments, it is crucial to make the flow phantom out of clear and transparent materials. Due to this requirement, the flow phantom needs to be constructed in such a way that it provides the optical and mechanical properties acceptable for analysis. There are a number of techniques for constructing the flow phantom. The most common approach is investment casting of clear silicone. However, with ongoing progress in 3D printing, it is now possible to use this newer technique and produce directly the flow phantom.

This chapter will first introduce the investment casting technique, to provide a brief description of the process. The 3D printing technology and process will also be discussed, followed by a comparison between 3D printing and investment casting. The design and overall process of printing the flow phantoms including any pre and post printing processes used in this project will also be provided.

4.2. Investment casting

Investment casting is one of the oldest casting techniques used to produce objects containing internal channels. During the casting process, the internal voids are filled by a male pattern, made out of wax. The part is constructed by pouring the material, in liquid form, into the enclosed frame. Clear silicone has the advantage of producing a model with a relatively low refractive index value.

4.2.1. Investment casting process

In general, the investment casting technique requires the following steps in order to construct a flow phantom that can be used in PIV experiments:

- The first step is to create the male pattern, which must represent the channels of the artery. The pattern is produced from a soluble material, such as wax. The geometry construction evolved from a skilled artist or mould maker, to 3D printing with custom made casting wax filament. In the latter case, the geometry can be computer generated by 3D scanning and adaptation using computer aided design (CAD).
- The second step is to create a negative mould. This mould will determine the exterior shape of the final flow phantom. The negative mould wall geometry is very important because it determines the enclosure's surface flatness. The mould can be created using a computer numeric control (CNC) machine, to improve accuracy, and is usually made out of aluminum.
- The third step is to assemble the first and second patterns together. The assembled unit must be tight to avoid any leakage.

- The fourth step is to carefully inject silicone between the external and internal patterns, followed by solidification and curing of the liquid. The curing process can take several days.
- The final step is the removal of the moulds and retrieval of the cured silicone model.

4.3. 3D printing

Additive manufacturing offers advantages such as lower costs and shorter manufacturing time. 3D printing is also pushing the limits in manufacturing processes, due to its ability to reproduce a design without the need for special cutting tools.

In the past few years, various advances have been made to improve printing resolution and to lower 3D printer production costs. Different kinds of 3D printers make use of different technologies and different feeding materials. The most common technologies used in 3D printing are fused deposition modelling (FDM), stereolithography (SLA), selective laser sintering (SLS) and Polyjet or Inkjet printing. The choice usually depends on the available material and the cost of printing.

4.3.1. 3D printing technologies

FDM offers the lowest resolution and the cheapest cost of manufacturing. It is widely used by hobbyist 3D printers. The printing process is based on melting a standard thermoplastic, such as PLA filament, as it passes through an extruder, before being squeezed through a print nozzle and deposited on the build plate. The model is built layer by layer. In most cases, steps taken between successive layers are achieved by lowering the build plate and the step often sets the resolution along the vertical axis.

Stereolithography uses a process called photopolymerization. This technology appeared in the 1980s. In SLA 3D printing, a laser beam is used to strike and polymerize a liquid layer within a transparent tank and successive layers are polymerized beneath each surfaces, resulting in a homogenous solid print without voids. This operation is done on a build plate completely submerged in a tank filled with resin. Parts are created with higher resolution and finer detail. A wide range of resin formulation is available and this includes optical material and other engineering materials. Figure 15 below describes SLA 3D printing and shows how layers bond without leaving gaps.

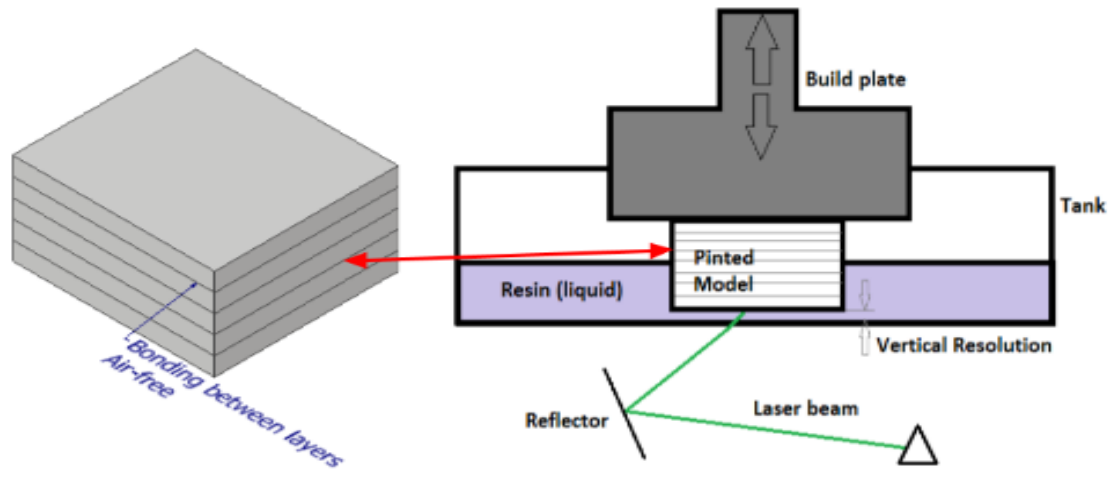


Figure 15 SLA printing in resin bath

Selective laser sintering (SLS) is the most commonly used technique in industrial applications. The technology makes use of a high-powered laser to fuse polymer powder. The rest of the powder, which has not been fused, can serve as support structure. This gives SLS the important advantage of being able to produce very complex shapes while achieving excellent mechanical characteristics. The most common material use in SLS 3D printing is nylon. Optical materials have not been reported for this particular printing technology.

The table 3 below makes a comparison between these 3D technologies.

Table 3 3D printing technologies (prices as of 2018)

3D printing technology	FDM	SLA	SLS
Equipment costs	Desktop: \$2,000 Industrial systems: \$15,000	Desktop: \$3,500 - \$10,000 Industrial systems: \$15,000	Desktop: \$10,000 Industrial systems: \$100,000
Material costs	Standard filament: \$50-\$150/kg Support material: \$100-\$200/kg	\$149-200/L	Nylon: \$100/kg
Labor required	Support removal: manual or Automated (soluble support material)	Support removal Washing Post curing	Remove excess powder

From table 3 above, only FDM and SLA can make use of clear, optical materials. After several investigations, SLA offered the best optical properties and was therefore selected as the most appropriate technology for this work. Inkjet 3D printing of flow phantom was reported by Aycok, Hariharan and Craven, (2017). Their work made use of Polyjet technology to produce clear models for PIV studies. The main limitations associated with the technique was that the printing orientation affect the optical properties of the model. The most acceptable results were obtained at a printing orientation of 45° only.

Inkjet or polyjet 3D printing and FDM have a very similar working configuration, and both build parts by individual layer deposition in open-air. Inkjet makes use of UV curable liquid resin instead of a standard thermoplastic such as PLA filament. In inkjet 3D printing, curing is achieved by exposure to UV radiation during the printing process. Figure 16 below describes the polyjet 3D printing process, illustrating the possibility of air gaps as a result of layer deposition in open air which can affect the trajectory of light as it passes through the model and this can explain why Aycock, Hariharan and Craven, (2017) did conclude that 3D printed flow phantom can only work at a certain angle when used in PIV.

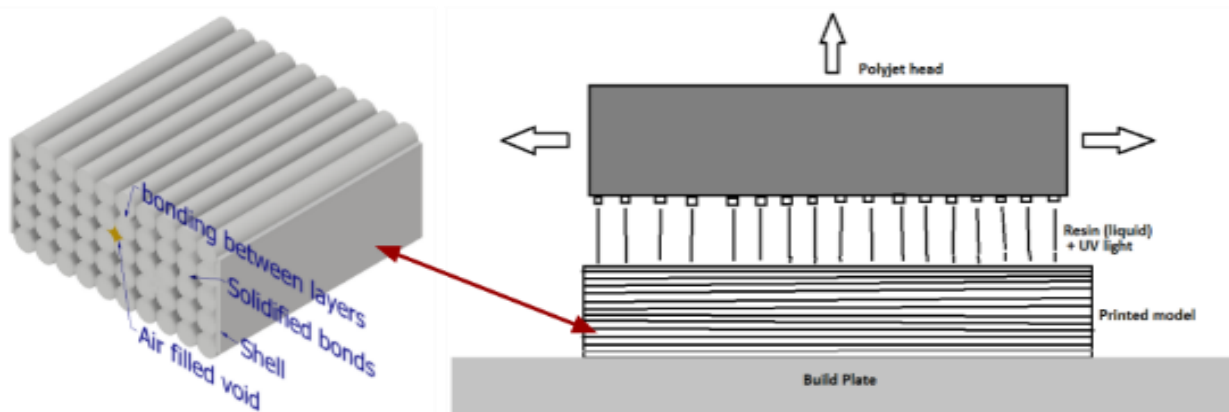


Figure 16 Inkjet 3D printing

Comparing the SLA and Inkjet 3D printing technologies, which can both make use of clear material, it is arguably true that SLA produces the most coherent solid medium and therefore faithfully reflects the light as it passes through the printed model. PIV images recorded on flow phantoms printed with SLA conserve their good qualities regardless of the print orientation or angle. In light of the abovementioned observations, SLA is a better choice for producing flow phantoms for PIV experiments. The printer and material chosen for this project was the Form2 printer using the FLCPL series resin from Formlabs.

4.4. Phantom geometries

Idealized geometries are generally considered acceptable to give a general sense of the flow field throughout the population. In addition to being somewhat standardized, idealized geometries also reduce complexities of realistic geometries, which could not be easily manufactured with more dated techniques. In this work, most of the experiments are conducted in idealised geometries. The framework is then extended to realistic geometries, as a proof of concept.

PIV images are provided for both idealized and realistic geometries, to demonstrate that 3D printing can be used to study hemodynamics in blood vessels of varying complexity. PIV results will be conducted on rigid, idealized geometries. Flexible flow models will be the subject of future investigations.

4.4.1. Idealised geometry

The experiments in this study were conducted using an idealized cerebral aneurysm geometry. The geometry was adapted from the work of (Mulder *et al.*, 2009) and (Yu *et al.*, 2012). The latter study used the model to examine the effect of two different stents and the resulting hemodynamics. The idealized geometry was created using Space Claim ANSYS® 18.0 from ANSYS® and Autodesk® Inventor® Professional 2013. Figures 17 and 18 below show the geometry of the idealised cerebral aneurysm and the final model encapsulated in a rectangular “box”.

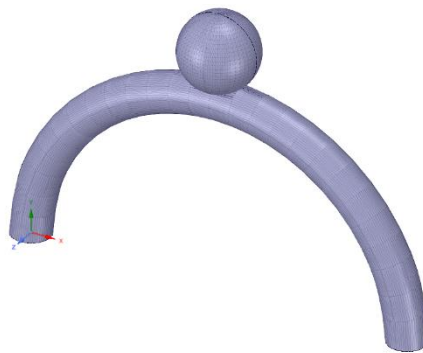


Figure 17 Idealised geometry STL file

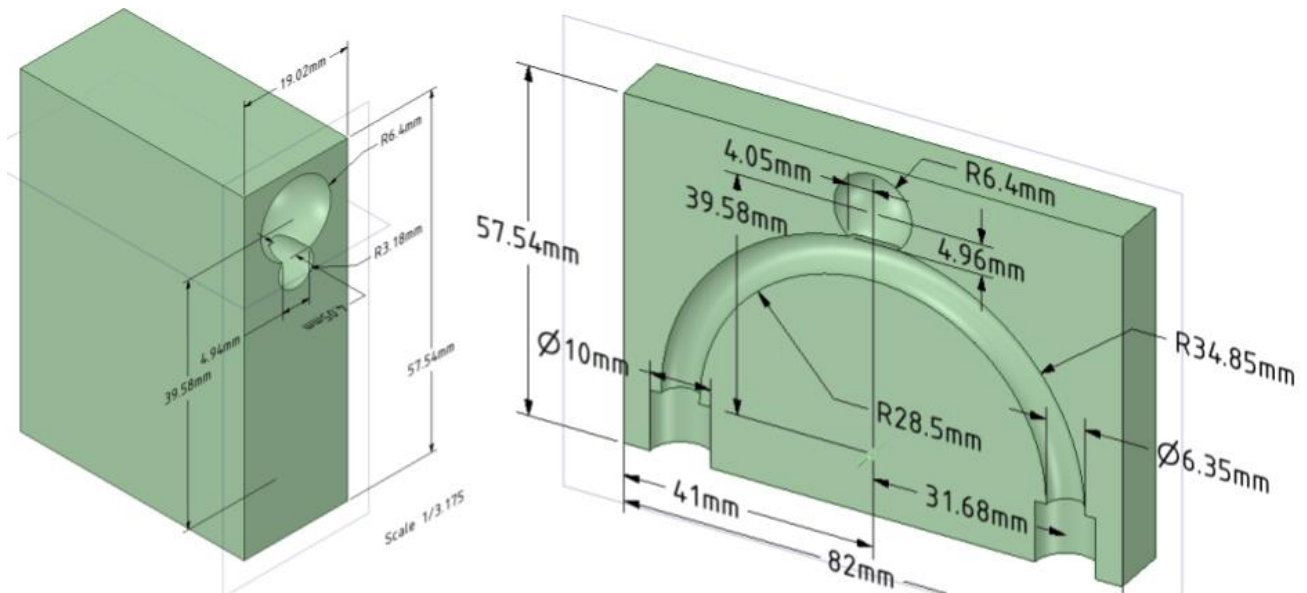


Figure 18 Idealized flow phantom

4.4.2. Realistic geometry

In order to extend the framework developed using the idealised model, a realistic geometry (shown in figure 19 below) of a cerebral aneurysm was obtained from a computed tomographic (CT) scans. The diameter of the artery was approximately 2 mm. The model is used to test the 3D printing capacity and the PIV setup, however, results of the realistic geometry will not be analysed in this thesis.

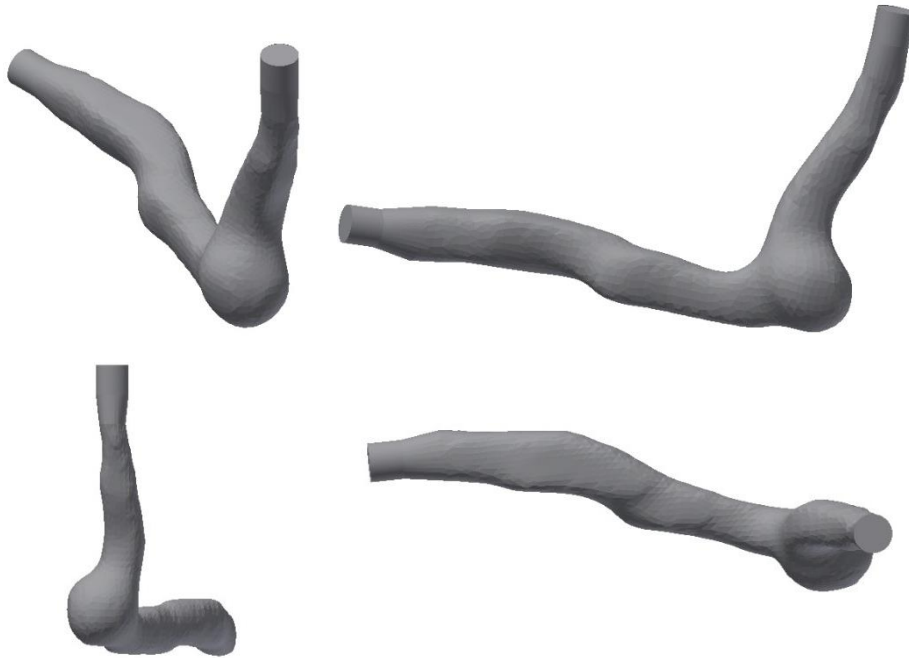


Figure 19 Realistic geometries

This particular cerebral artery with an aneurysm has an L shape, with a $\pm 90^\circ$ angle at the neck. Figure 20 below shows the final design of the realistic flow phantom before printing.

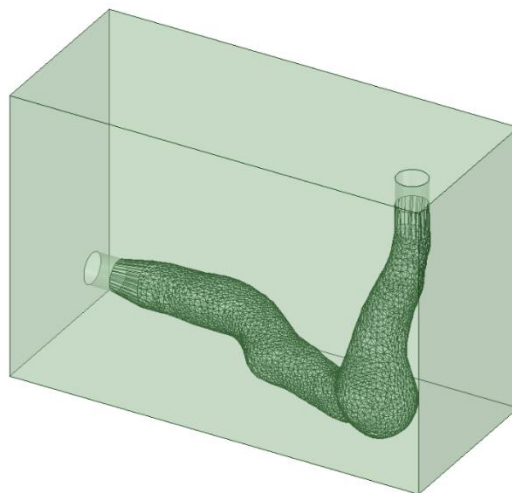


Figure 20 Realistic model final design

4.5. 3D printing of Flow Phantom

One of the main goals of this study was to investigate and find a suitable 3D printing technique in order to produce flow phantoms that can be used in PIV experiments. The idealized and realistic geometries were successfully 3D printed using clear photopolymer resin form 2 FLGPCL02 (material sheet to be found in Appendix E). The model was printed on a Form2 desktop SLA printer, as illustrated in figure 21 and 22. To start the printing process, it is important to prepare the CAD model. The flow phantom requires the use of CAD software to specify the final shape and scale of the model. The idealised geometry is produced using CAD software, while the realistic geometries are generally obtained from CT or MRI scans. Many 3D printers require the CAD model to be exported in STL format to ensure compatibility with the printer's software. Once the model is printed, additional processes are usually required in order to achieve better quality. Post-printing processes such as cleaning the printed model in isopropyl alcohol (IPA), right after the print, ensure that uncured resin is removed from the model's surfaces. Other important post-curing processes include drying the model under UV-light. Sanding the external surfaces is also considered good practice, as it prepares the surfaces for painting with a fine coat of clear lacquer. The sanding was done using water and sanding paper from lower to higher grades (P600 to P2000), resulting in a good finish. This was followed by spraying of clear lacquer, which improved the clarity of the model.

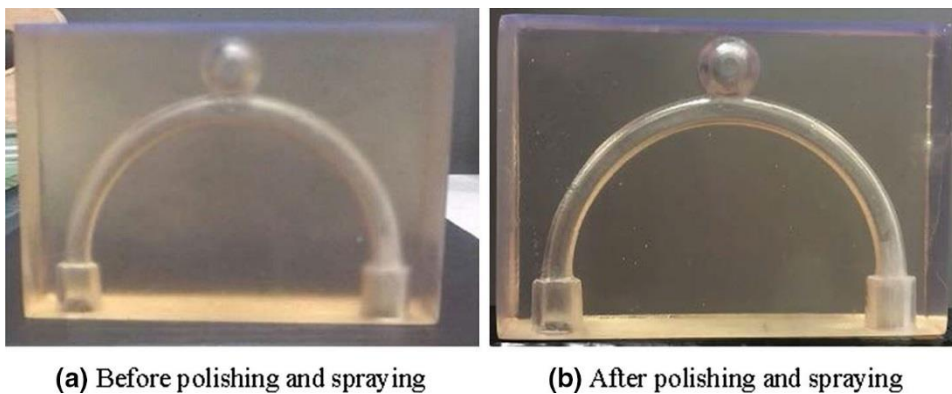


Figure 21 Idealised geometry model printed on SLA 3D printer

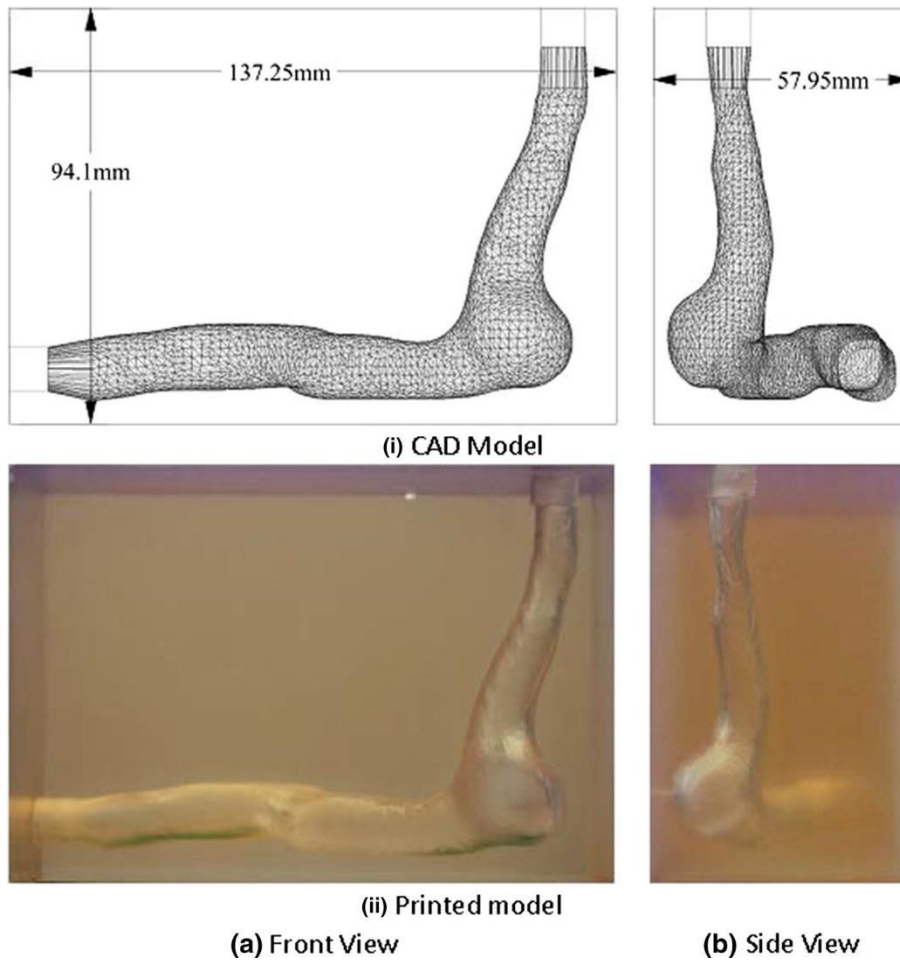


Figure 22 3D printed realistic geometry on SLA 3D printer

Inkjet printing has limitations related to the printing orientation. This work presents PIV results that were conducted on the SLA printed flow phantom using FLGPCL02. Phantoms printed using SLA give acceptable optical properties for PIV measurements. A suitable working fluid that will match the properties of blood and match the optical properties of the phantom is required. In the next section, the refractive index (RI) test will be introduced. RI testing is done in order to match the RI value of the working fluid with that of the flow phantom. The objective is to achieve 100 percent match, but due to temperature changes during experiments and aging factors, it is important to constantly conduct the RI test. Table 4 below shows the list of materials for the working fluid and the flow phantom with their respective RI values.

Table 4 Material properties

Material	Refractive index
Borosilicate glace (Tracer particle)	1.52
De-ionized water (base fluid)	1.33
Ammonium thiocyanate (mixing powder)	1.685
CLEAR FLGPCL02 ¹ Formlabs (Flow phantom)	1.507 (+/- 0.003).

4.6. Matching the refractive index between flow phantom and working fluid

In order to get PIV images with an acceptable optical quality and avoid light distortion, which influences results, it is important to consider the refractive index matching. In order to reach the exact value of the refractive index of the solid material or the flow phantom it is important to find a fluid of the exact RI which is usually difficult to find. The common approach is to use fluids of higher and lower refractive-index values that can be mixed proportionally to achieve the required balance and match the phantom's RI. The base fluid and the mixing fluid will also need to have densities and kinetic viscosities that will enable homogeneity in mixing and ideally match the properties of blood.

Water would be the best fluid to conduct experiments because it is safe and cost effective, transparent and clear. Working towards meeting the refractive index of water "1.33" would result in an ideal optical product for PIV studies. The challenge in this study is that the refractive index of the phantom does not match that of water. Future work that will consider finding a 3D printable material with RI value similar to that of water should be encouraged.

One of the best working fluid choice considered for this study is ammonium thiocyanate prepared as an aqueous solution (Jermy, 2013). The choice is mainly due to its high RI value and its availability from local suppliers. Ammonium thiocyanate (NH_4SCN) at its highest RI value can be found in powder form and it is colourless, shiny, flaky or columnar crystal and additional information about this compound can be found in the extensive work conducted by Borrero-Echeverry and Morrison, (2016). The refractive index of NH_4SCN is 1.685. It is easily soluble in water and undergoes an endothermic reaction while being dissolved in water. It is not flammable and is therefore relatively safe when well stored.

The refractive-index-matching test of the aqueous solution of ammonium thiocyanate and deionized water at room temperature was conducted successfully. In order to match the SLA printed phantom's refractive index, the solution comprised 66% NH_4SCN and 34% deionized water by weight was used. The measurement of refractive index of the printed model was conducted and the value are given in Table 4 above. Figure 23 below shows the RI matching technique using a black and white checked grid behind the model, for visual inspection of any image distortion that would suggest a mismatch in RI values. Visual inspections conducted to test RI matching show minimal distortion and an acceptable level of optical access, required for PIV analysis.

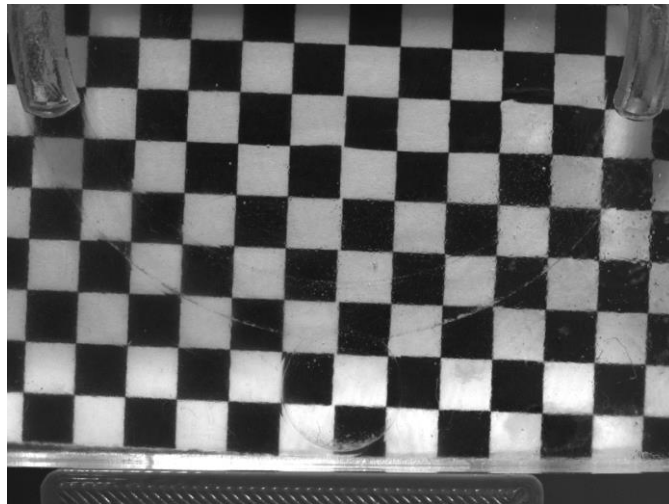


Figure 23 RI matching test during PIV

This working fluid is sensitive to changes in temperature and figure 24 below illustrates the viscosity variation as a function of temperature. The viscosity was measured with a TA instruments discovery hybrid rheometer. At temperatures ranging from 25 °C to 45 °C a 40 mm Peltier parallel plate was used to measure the viscosity of the walking fluid as reported below.

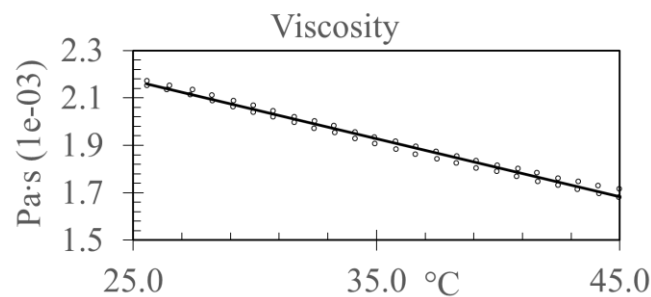


Figure 24 Viscosity of the working fluid

4.7. Refractive index check using MATLAB

A more rigorous check for distortion due to mismatch of RI can be done by analysing the images using digital image processing tools.

The steps taken to check for RI matching still make use of a black-and-white checkered board, which is placed behind the flow phantom. The flow phantom is connected to the flow circuit through the inlet and outlet. The pump is then switched on and the working fluid circulates through the model. Single images of the flow phantom are taken. These images are then used in the MATLAB image tool application. The application allows manual measurements to be performed. In order to evaluate any distortion due to changes in RI, squares are measured in line, both through the solid medium and solid-fluid medium. Through comparison of values, it

becomes evident whether there is a mismatch between regions in the model. Any mismatch is corrected by adjusting the work fluid (adding additional ammonium thiocyanate or deionised water), whichever is required until acceptable conditions are met. Figure 25 below shows the RI matching test results.

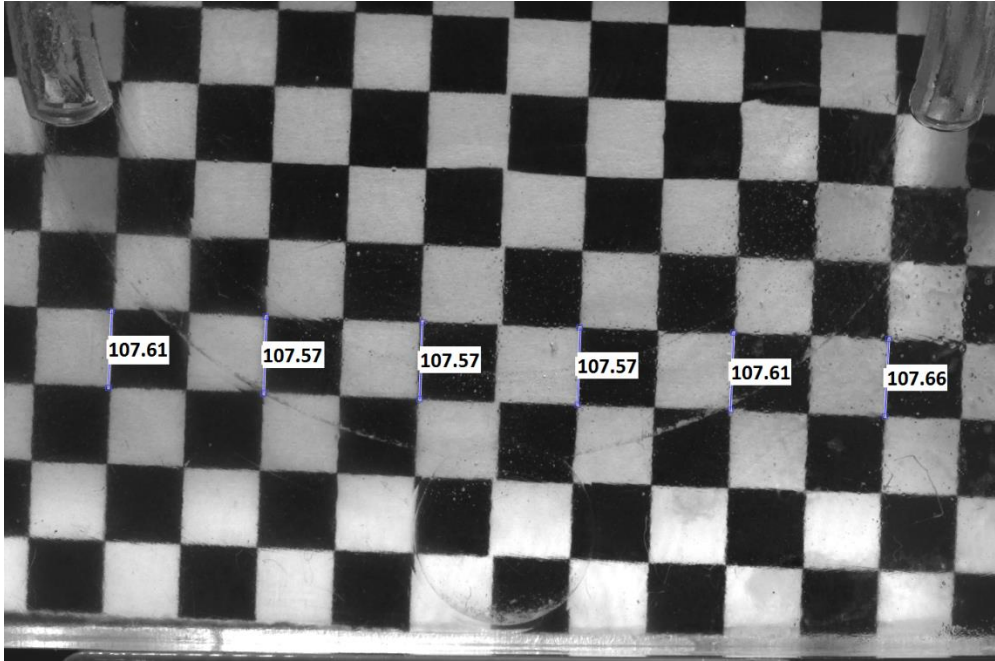


Figure 25 RI check during PIV experiments

Table 5 below shows the differences in measurements for this RI test, which is about 0.01%. The difference in measurements could be influenced by the flatness and congruence of the checkerboard, in relation to the back surface of the model.

Table 5 RI check using MATLAB Image Viewer

	1	2	3	4	5	6	Average
Measured height	107.61	107.57	107.57	107.57	107.61	107.66	107.5983
% difference from average	0.010001	0.009997	0.009997	0.009997	0.010001	0.010006	0.01

4.8. Surface roughness measurements

Surface roughness measurements are essential for assessing the quality of the print. For complex geometries, such as those representing aneurysms, it is not yet feasible to polish interior surfaces. The surface roughness is an important factor for flow dynamics in interior channels. This project is one of first to conduct such measurements. The surface roughness measurement was conducted using the SmartZoom 5 Digital Microscope from Carl Zeiss. The digital microscope was able to generate the topography of the surfaces, manual measurement was required in order to compute the surface roughness. The surface roughness measurements were taken along the X-axis and along the Y-axis. The arithmetic average roughness (Ra) was

calculated along each axis from the values extracted from the digital microscope report. The X-axis had a Ra value of 2764 nm while the Y-axis had a Ra value of 5093 nm. The Ra values correspond to N8 and N9 of the Roughness N ISO Grade number respectively which implies a good finish quality. Table 6 below gives a summary of the printer and the printed part's specifications.

Table 6 Summary of the printed part

Printer	Form2 desktop SLA printer
Printing resolution	25 μm
Material	Clear photopolymer resin FLCPL Series
Surface roughness of the printed model	(Ra – Average roughness) X-axis Surface Ra 2764 nm / Y-axis Surface Ra 5093 nm (Measured with SmartZoom 5 Digital Microscope)
Measured refractive Index of the model	1.507 (+/- 0.003)

4.9. Conclusion

This chapter discussed the flow phantom making process, emphasising the best 3D printing technology for this project. The chapter gave more insight into the differences between 3D printing technologies available on the market and concluded that SLA 3D printing technology was the most suitable for PIV experiments. A description of the printing process was also detailed. Key aspects relating to the flow phantom geometries and construction were discussed as well as the optical properties required. The following Chapter 5 gives more insight on PIV experiments and how PIV is conducted on these transparent models.

CHAPTER 5 : PARTICLE IMAGE VELOCIMETRY (PIV)

5.1. Introduction

Particle Image Velocimetry (PIV) is widely used in hemodynamics studies, mainly due to the non-intrusive nature of this technique. In order to conduct a PIV experiment a set of materials, equipment and systems need to be gathered. Selecting the right optical material for the flow phantom and the appropriate working fluid is essential to the success of the experiment. The details of how the flow phantom was made and the details about the working fluid were discussed in Chapter 4. PIV measures velocity components of the flow field, based on recorded image frames, while the fluid flows through the flow phantom. The experimental setup therefore needs to enable image recording. The recorded images are later subject to further processes. In order to capture images of the flow field, the flow phantom needs to be transparent and clear, so to allow visual access to the flow field without any obstruction. In addition, the flow field needs to contain seeded tracers in order to computationally trace the displacement of the working fluid in details. This necessitates the use of seeding tracer particles in the working fluid. The tracer particles, in turn, have to be illuminated by a light source, such as a laser, to increase their visibility inside the flow field during image capturing. In the case of a planer PIV system, a camera is placed perpendicular to the flow and is used to record sequences of images of the flow. Recorded images are used in a PIV algorithm and results are generated in this manner. This chapter will detail the theory of PIV. This discussion will include cross-correlation techniques and seeding particles. Important components, such as cameras and lasers are also presented in this chapter.

5.2. PIV as a tool for fluid flow measurement

PIV, being a fluid mechanics tool for flow measurements, shares some similarities with Particle Tracking Velocimetry (PTV). Both of these techniques are based on time-lapse photography or video recording, and are thus identified as flow visualization techniques, conducted in transparent flow media (Potter, Wiggert, & Bassem, 2015). The method consists of a pulsed light source (e.g. laser) that illuminates small fluid-entrained particles over a short period of time exposure. PTV generates vectors based on the tracking of individual particles and requires lower seeding density of tracer particles. This method is therefore suitable for channels with simple shapes. PIV techniques, on the other hand, generate vectors based on a statistical average for many particles within a particular interrogation window. This increases accuracy of results in more complex flow structures, where higher seeding density is required. In this study we will be conducting measurements using planar PIV.

Many experimental studies on aneurysms have made use of PIV to obtain velocity data. PIV requires an algorithms with a cross-correlation code that will generate velocity vectors from captured images. When flow images are processed through a cross-correlation code, instantaneous velocity measurements and related derivatives of velocity, such as vorticity, can be obtained. The motion of the fluid needs to be visualized (e.g.

through a high-speed camera) and the fluid has to be seeded with tracer particles, which are relatively small in size. The tracer particles need to be density neutral relative to the working fluid. The shape of the tracer particle is equally important and ensures fidelity to the flow dynamics. The Stokes number is generally used in order to determine the faithfulness of the tracer particle as it is being dragged by the working fluid. When illuminated by a strong light source such as a laser, the motion of the particles can be captured and used to calculate the speed and direction of the flow under investigation within the region of interest. For internal flow systems, a transparent flow phantom is required. A typical PIV system is depicted in figure 26 below.

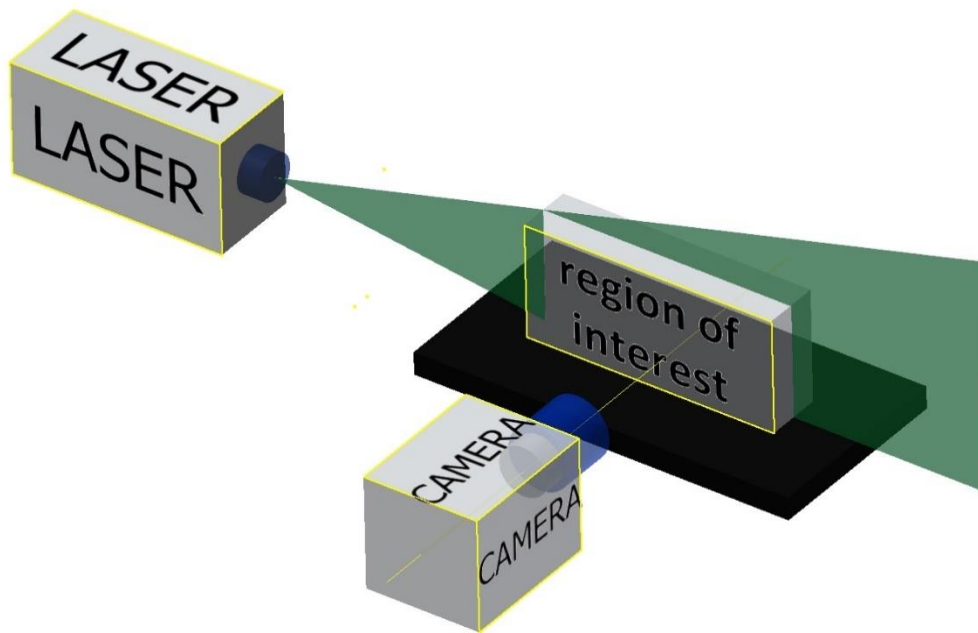


Figure 26 Typical PIV configuration

In addition to the laser, the high-speed digital camera and the algorithm, the clarity of the flow phantom is equally critical to the success of the experiment. The discussion around the optical properties of the flow phantom has already been presented in Chapter 4. More details of the camera and laser used in this work are provided in Appendix (A and B). Tracer particles also play an important role in ensuring that the algorithm can track the displacement of the fluid faithfully. Provided that there is neither obstruction nor constriction while acquiring velocity values, the non-intrusive nature of PIV makes it a method of choice and arguably a tool that produces the more realistic results. Other than the flow model, other important components in a PIV experiment are the laser and its accompanying optics, the PIV camera and the seeding particles. Details of these are given below.

5.2.1. Laser

Particle illumination is an important parameter in PIV. Light can be identified as a form of radiation and is characterized by its wavelength. When the wave encounters a new medium, its speed changes and it undergoes deflection. Laser (acronym for Light Amplification by Stimulated Emission of Radiation) first

appeared in the early 1960s, based on theoretical studies conducted by Charles Hard Townes and Arthur Leonard Schawlow. Spatial coherence is the advantage that laser has over other sources of light. In addition, the light from the laser can be made into a light sheet, which is suitable for planar or stereo PIV or as a volume for tomographic or light-field PIV, using suitable optics. This enables pulses of light to be produced and externally controlled, without using mechanical interfaces, while providing coherent light. This makes the laser a good option for PIV. In our experiment, the laser used in this study is the Oxford Firefly Laser. Key specifications are listed in table 7 below.

Table 7 Specifications of the oxford Firefly Laser

Light Source	Semiconductor laser
Laser Class	Class 4 (IV)
Wavelength of emission	808nm \pm 3nm
Peak power	300 watts
Pulse energy	0.15mJ to 30mJ
Individual pulse length	0.25 μ s to 100 μ s
Maximum duty cycle	1%
Maximum external trigger frequency	0Hz - 10 kHz
Internal trigger frequency	1Hz - 10 kHz
Pulse separation (in burst mode)	Range 0.5 μ s - 9999 μ s

The Firefly 300W Laser used in this work can be fully computerized. The laser head is built with integrated adjustable optics and this fixture enables manual control of the laser sheet thickness and no external laser optics are required. The laser is coupled to a compact controller that contains all the control electronics. The unit is very compact and can be mounted on the setup with ease. The laser produces a light with a wavelength of 808nm, which is invisible to the human eye. This wavelength is within the range of the camera's quantum efficiency, as shown in the following section. The equipment is supplied with an infrared detector card to enable visualization of the light during setup. There is a major safety issue relating to this class IV laser, whose light cannot be localized by the naked eye. The use of safety goggles is therefore a requirement and has to be worn during image capturing, while the laser is running.

5.2.2. Camera

The pco.pixelfly usb is the high speed digital camera used in this work. This is a 14bit CCD camera system with a quantum efficiency of up to 62% as shown in figure 27 below. The camera is equipped with a PGA processor for better control and perfect timing of the CCD. These characteristics of the camera are important in order to clearly view the particles at a particular wavelength of the laser. The key specifications of the camera are provided in the table 8 below and technical data is provided in Appendix B.

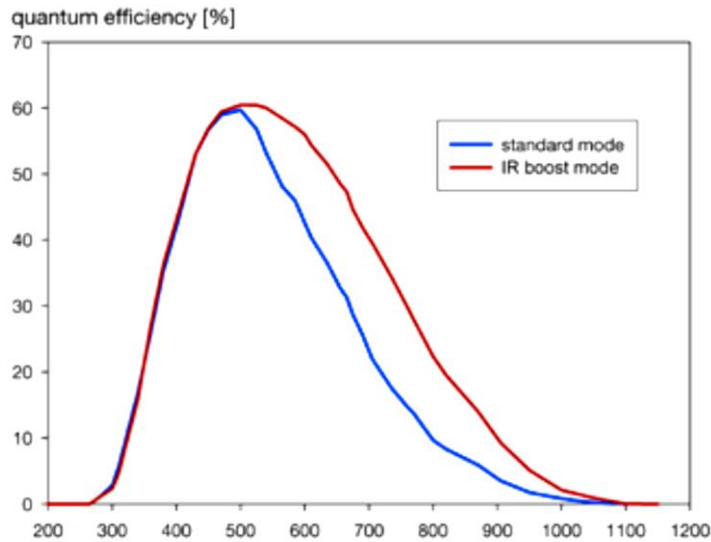


Figure 27 pco.pixelfly usb quantum efficiency graph

The camera's main features are:

Table 8 Specification of the PIV camera

Camera	Pco.pixelfly usb	Unit
Resolution (horizontal x vertical)	1392 x 1040	pixel
Pixel size (horizontal x vertical)	6.45 x 6.45	μm^2
Quantum efficiency (peak)	62	%
Optical input	c-mount	
Exposure time	5 μs to 60 s	
Image frequency (frame rate)	7.3 / 13.5	fps
Interface	USB2.0	

The camera is suitable for particle image velocimetry applications and is controlled through its software, CamWare. The software enables the user to set the timing and to control the image quality, while providing an interface for image visualization and recording.

Auto Sequence trigger mode is an optimized option for the camera to achieve the best frame rate possible, depending on the adjusted exposure time and the required readout time. When this exposure control is selected, the recording sequence starts and ends with a command. This trigger mode was used to record PIV images in this work. The exposure time for this camera can be set between 1 μs to 60 s and adjusted in steps of 1 μs .

The image sensor readout speed is controlled by the pixel clock which sets the clock frequency. Two optional frequencies are available. The options are 12 MHz and 24 MHz. With 12 MHz, the image quality is higher due

to the low readout noise, while the 24MHz option gives higher frame rates and suitable for PIV application of high flow rates. Table 9 below provides more details on the clock frequency options.

Table 9 The pixel clock

Resolution	12 MHz	24 MHz
1392 x 1040	7.3 fps	13.5 fps
800 x 600	11.7 fps	21.6 fps

The camera has both single and double image options and the double image option needs to be activated whenever PIV experiments are being conducted. The camera exposure time needs to be set for the first exposure and can be any value within the range of the camera. The second exposure time is automatically adjusted by the readout time of the first image and therefore cannot be set. These settings are used as a signal reference to the laser for the timing of the light pulse.

As previously stated in this section, the recording is done through the camera software. The maximum number of images that the camera is able to record at a given time is mainly dependent on the available RAM on the computer.

PIV image recording is a critical step as the results rely heavily on it. The following steps are important prior to image capturing: matching the refractive index, setting the required flow rate and seeding the right amount of tracer particles, and focusing the camera on the plane of interest.

5.2.3. Seeding particles

In order to obtain useable PIV images, the right choice of seeding particles has to be made so that the seeding particles can scatter the light from the laser beams or the light sheet, and make it visible to the camera. Mean particle size, specific gravity, particle shape, width of size distribution, surface characteristics and refractive index are important properties for selection purposes.

The characteristics of a seeding particle illuminated by the laser when looking through the PIV camera is also limited by the diffraction in the lens (Geoghegan, 2012b). The seeded particle in the flowing fluid may appear as an airy disk instead of a point source. This condition is believed to be directly proportional to the laser timing.

The size of the Airy disk set the limit for the smallest particle that can be obtained using a digital camera. The diffraction limiting diameter can be calculated, the extensive work by Geoghegan, (2012) gives more details.

20 μm mean diameter Hollow glass spheres (HGS) particles made from borosilicate glass it is generally used for liquid flow application and was suitable for this this experiment. The seeding material used for the experiment has a spherical shape, 1.1 g/cm^3 density and a refractive index of 1.52 from Dantec Dynamics, Denmark.

5.3. Cross-correlation

PIV technique focuses mainly on acquiring a set of image pairs of the flow being investigated and uses the recorded images to derivate velocity vectors. In order to achieve this, a computer algorithm is used to determine the changes in distance and direction for a set of particles within an image pair. By taking the separation time between an image pair, the velocity can be computed from the known changes in distance. The following equation can be used,

Equation 2

$$u = \frac{d}{M\Delta t},$$

With u the velocity, d the diameter, M representing the scale factor for pixel to mm conversion and Δt the separation time.

5.3.1. Cross-correlation used in this work

The cross correlation algorithm used in this work is PIVLab, which is an open source PIV software programmed with MATLAB. PIVLab does not just calculate the velocity within an image pair but can also be used to compute other velocity derivatives of the flow such as vorticity and can provide additional tools to visualize and post process results. PIVLab can perform single analysis using a single frame and can also perform time-resolved analysis using multiple frames to give a sense of the flow progression and an average of the velocity. PIVLab gives two cross-correlation options to choose from and the Discrete Fourier Transform (DFT) was the one utilised in this study.

5.3.2. Types of cross-correlation in use

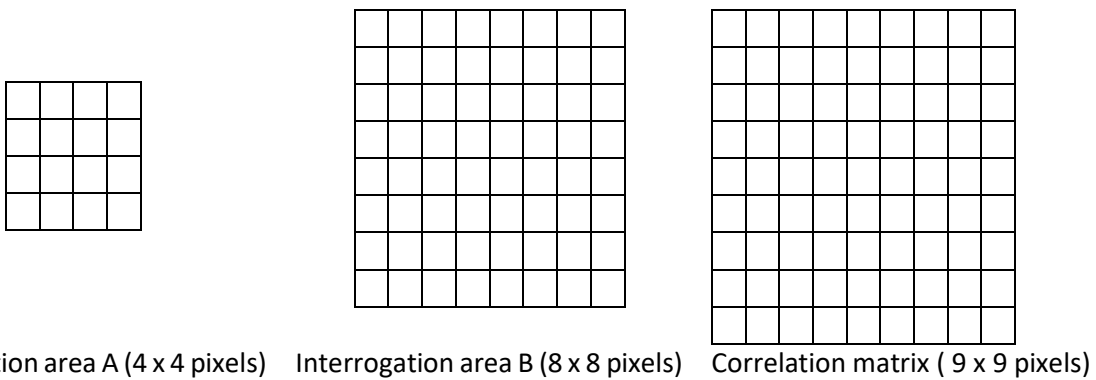
Cross-correlation is performed on image pairs by dividing the images into multiple uniform and adjacent areas of defined numbers of pixels called interrogation areas on each image within the pair. The cross-correlation technique can thus be regarded as a statistical pattern tracking tool from the first image to the second image within the pair (Huang, Dabiri and Gharib, 1997). In the discrete cross-correlation function, a statistical technique is implemented.

Equation 3

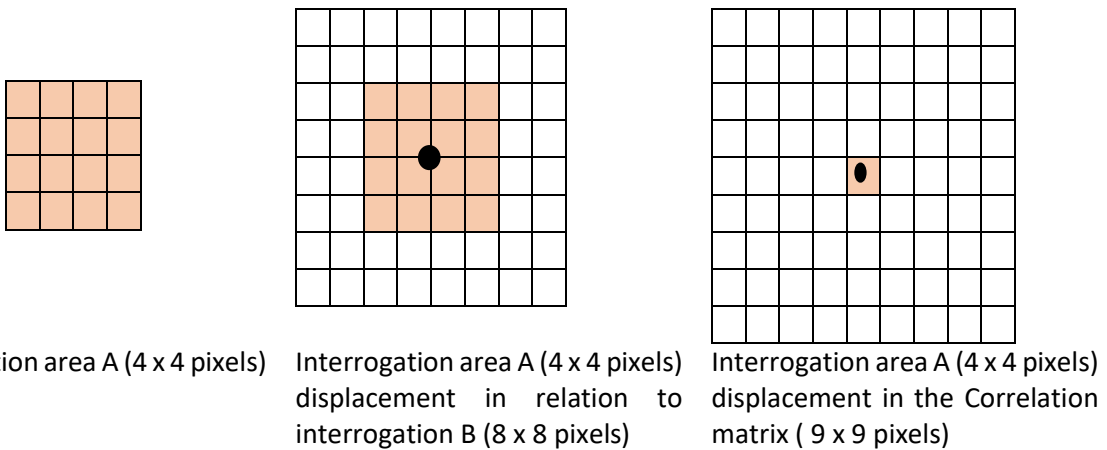
$$C(m, n) = \sum_i \sum_j A(i, j)B(i - m, j - n)$$

With A representing the interrogation area from the first image and B the interrogation area from the second image within the pair. For a given shift, the discrete cross-correlation measures the agreement between interrogation areas A and B (Cholemari, 2007). The resultant matrix C gives the expected displacement of groups of particles from image A to B by finding the location of intensity peak.

Cross-correlation can be used in the spatial domain, referred to as direct cross-correlation (DCC), or using the frequency domain, calculated using a fast Fourier transform. The latter is also referred to as discrete Fourier transform (DFT). A brief description of the two approaches is given in the sections that follow. 5.3.3. Direct cross-correlation (DCC)



At the initial position the interrogation area A has zero displacement in relation to interrogation area B (Shift $x = 0, y = 0$)



Now let the group of particles in the interrogation window A shifts downwards towards the right (shift $x = 1, y = -2$)

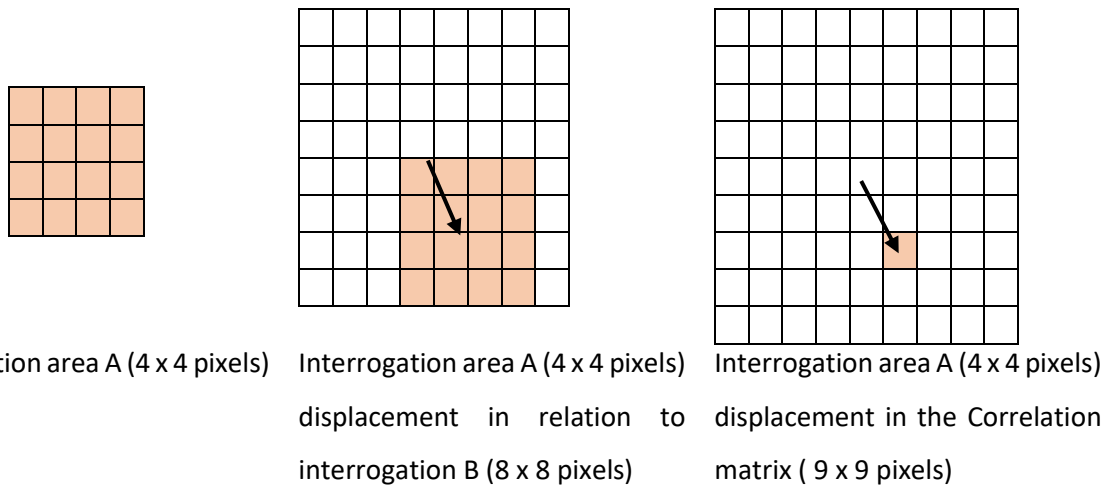
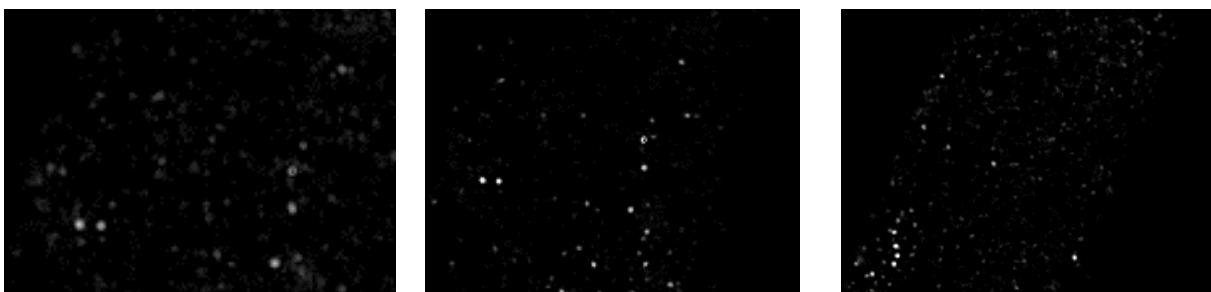


Figure 28 Direct cross-correlation

The above figure 28 shows the DCC approach. When large interrogation areas are required, the computational cost increases with the DCC approach, as both time and space are required. This is the noticeable disadvantage of the DCC approach, but with advances in computing, it is widely accepted that this method is more efficient than DFT, which is briefly discussed in the following section.

5.3.4. Discrete Fourier Transform (DFT)

The standard DFT illustrated in figure 29 below is less computationally expensive when determining the displacement of a tracer particle from the first interrogation area on image A to the second interrogation area on image B, and when both interrogation areas are the same size. Owing to the identical interrogation areas A and B, every displacement of a tracer particle is inclined to some degree of error in the correlation matrix. This error is noticed because the background noise in the matrix immediately increases once the displacement is greater than zero pixel. The occurrence of background noise makes it difficult to locate the position of the intensity peak, and therefore reduces the accuracy of the DFT approach.



Initial position in the first Interrogation area Displacement less than 1/2 Interrogation window size Displacement greater than the Interrogation window size

Figure 29 DFT measurements principles by calculating the correlation matrix in the frequency domain by detecting intensity peak

In DFT, the displacement of the tracer particle has to be smaller than the size of the interrogation area. In cases where the displacement is greater than half the size of the interrogation area, the location of the intensity peak is reversed in the correlation matrix and appears on the opposite side in this matrix (Thielicke, 2014). In order to prevent this phenomenon, the tracer particle displacement should be limited to smaller than half the size of the interrogation area. Different approaches can be explored to minimize the displacement within the interrogation area. One of the alternatives is to reduce the separation time (Δt) between image A and B, while the other requires reduction in image zooming in order to use images with the lowest magnification possible. A general rule is to keep Δt at approximately one quarter or one third of the size of the interrogation area, when DFT is applied. The result can also be improved by doing several passes of DFT on the same images, by refining the interrogation window in every pass. This enables better location of the intensity peak position, which can be better located with subpixel precision (Thielicke, 2014).

5.4. Calculation of Δt

As stated in the previous section, timing is a very important consideration in PIV. The time between image A and image B within an image pair needs to be determined so that the expected displacement falls within the limits that cross-correlation can trace. To determine Δt or separation time, it is necessary to start with dynamic similarity studies as shown in the following table 10 and 11.

Table 10 In-Vivo data

In-Vivo		
Fluid	Blood @ 38-39C	
Density	1060	kg/m ³
Viscosity	3.00E-03	Pa.s
Velocity	0.12	m/s
	0.15	m/s
Diameter	0.002	M
Re	84.80	
	106.00	

Table 11 In-vitro data

In-Vitro		
Working fluid	Ammonium Thiocyanate at 23.7 °C	
Density	1131	kg/m ³

Viscosity	2.50E-03	Pa.s
Velocity	0.027	m/s
	0.033	m/s
Diameter	0.007	M
Re	84.80	
	106.00	

If the maximum flow rate in the in vivo model is known, Δt can be calculated as follows:

The size of the 3D printed model is 94.1 mm x 137.25 mm from the front view or the view in front of the camera. The maximum velocity through the phantom is taken as 0.033 m/s and the camera resolution is 1392 x 1040 pixels. In the calculation, only 90% of the camera resolution is taken into considerations. This accounts for difficulties with fitting all borders of the model into the camera window. The starting interrogation area is taken as 16x16 pixels. The reduced camera resolution results in 1252 x 936 pixels. From this area, the number of individual interrogation regions (each with 16x16 pixels), results in 78.25 x 58.5 windows.

In this setup, 1252 pixels corresponds to 137.25 mm, hence 1mm is equivalent to 9.122 pixels. The maximum velocity reached is 0.033 m/s. Converting this value yields 301.026 pixels in one second. In the previous section, it was stated that the particle should not travel more than 1/3 of the interrogation window (which is 16 pixels). This translates to 5 pixels for succeeding captured images. To calculate Δt , the distance (5 pixels) is divided by the speed in pixels (301.026 pixels/s), giving a value of 16.6 ms. which is feasible because the laser can fire at a much faster rate and the camera separation time can be set accordingly.

The PIV system used in the work does not have an external synchronisation device between the camera and the laser, signals from the camera acts as the trigger for the laser and synchronisation is based on camera trigger. This is not the usual method of synchronising camera and laser and the next section illustrates how the synchronisation is performed.

5.5. Laser Timing

As indicated earlier, the synchronization is based on the signal from the camera. Figure 30 below shows idealized graphical illustrations of the camera trigger, camera exposure (which happens at a very small delay after the trigger) and the firing of the laser. Unlike conventional PIV system where the camera and lasers are triggered via a synchronization device, they are coupled in our setup. The laser takes its timing from the camera trigger signal (Figure 30a) and is set to fire before the end of the first and after the start of the second exposure of the camera with the duration between the two being the Δt as explained previously. The entire system is wired up according to the diagram in Figure 31 below.

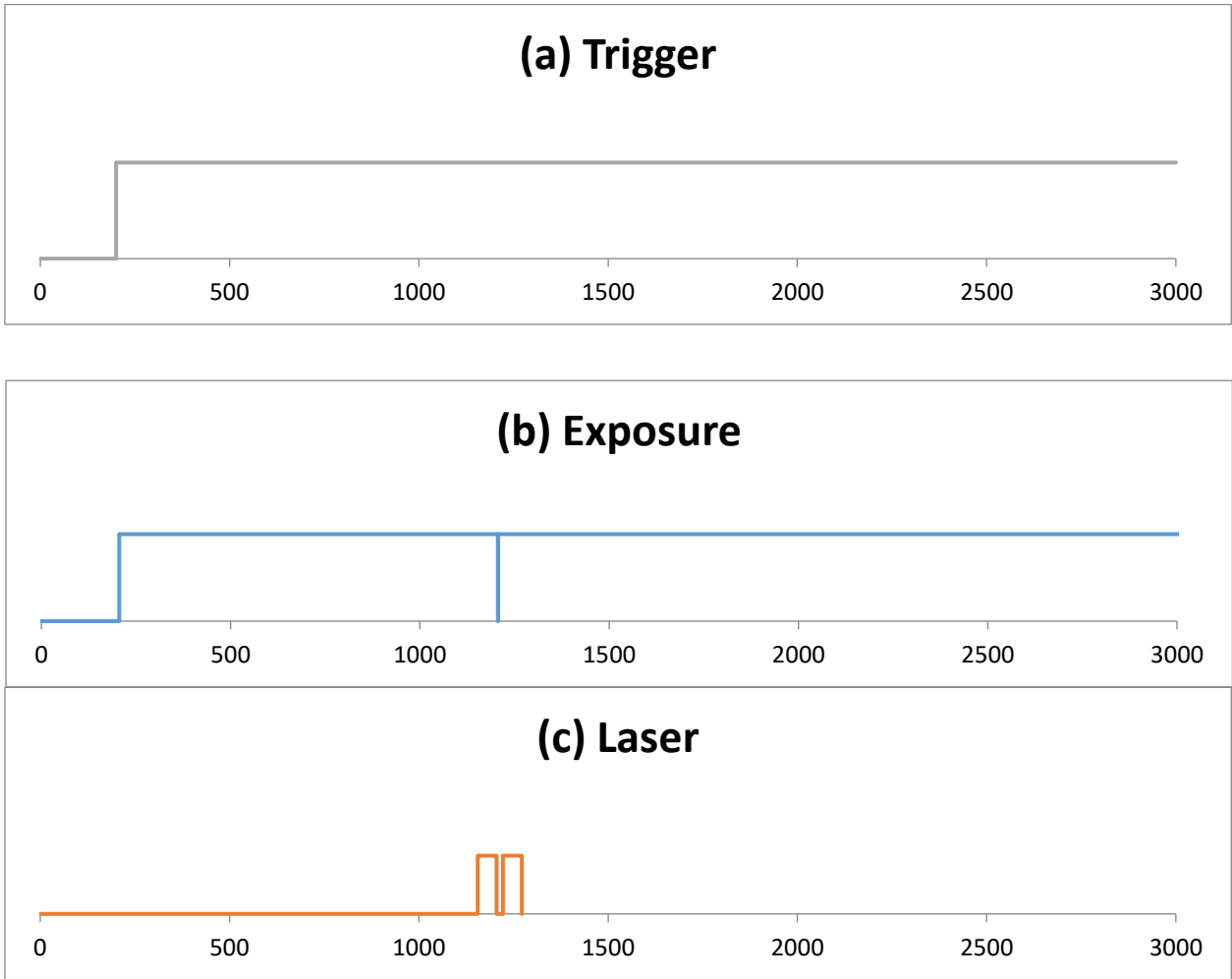


Figure 30 a. Trigger opening time, b. Camera exposure, c. Laser firing times

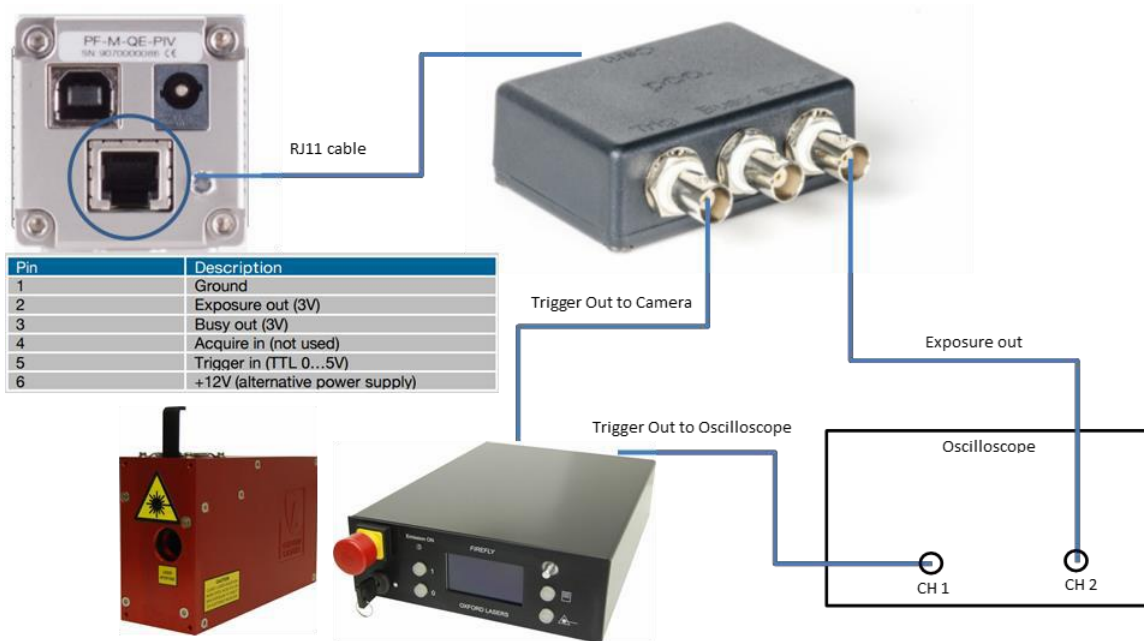


Figure 31 Laser and camera setup configuration

5.6. Accuracy evaluation in PIV

The accumulation of errors in the measurement process determines the level of accuracy. Thielicke, (2014) reported two important sources of error, the first one being random error (ε_{rms}) and the second being bias error (ε_{bias}). Bias error results from displacement estimations and how well they agree with the average of a series of measurements. The random error is related to the precision of the displacement estimate. It is also argued that particle size is an important consideration and that a particle size above 2 pixels in diameter increases errors (Guezennec and Kiritsis, (1990)). Both the trueness and precision are required to determine the accuracy of PIV and the respective formulae are given below,

Equation 4

$$\varepsilon_{bias} = \frac{1}{n} \sum_{i=1}^n d_{meas,i} - d$$

With d_{meas} representing the displacement as measured by the PIV algorithm, while d represents the true displacement resulting from the camera resolution and the model size and,

Equation 5

$$\varepsilon_{rms} = \sqrt{\frac{1}{n} \sum_{i=1}^n (d_{meas} + d_{meas,i})^2}$$

With d_{meas} representing the average measured displacement.

In addition to the abovementioned errors, the following points are considered to induce errors in PIV:

- Particle diameter, as previously explained in this section
- Particle density, which decreases as a result of optimizing particle density within an interrogation area. This requires a fair level of competence in PIV and the error was noted by Huang, Dabiri and Gharib, (1997).
- Sensor noise, which is hardly quantifiable and occurs during conversion of photons to electric signal by the sensor. This source of error can be linked to the random error.
- Motion blur, which depends on the light intensity from the source of light, e.g. the laser, and the light sensitivity of the camera. The camera exposure time needs to be long enough to capture all the light from the laser. The motion blur modifies the shape and therefore makes it difficult to achieve accurate measurements.
- Refractive index matching, which can be a source of image distortion.

5.7. PIV image recording

The camera used in this work was described in section 3.2.2 above. The lens used in this work is the RICOH FL-CC2514-2M. This lens has the following optical characteristics:

➤ Focal Length	25 mm \pm 5%
➤ Maximum Aperture Ratio	1: 1.4
➤ Iris Range	F/ 1.4 to F/16
➤ Picture format	8.8 mm x 6.6 mm
➤ Focusing range	0.25 m

Additional specifications of the lens are provided in the appendix B. This lens has a (theoretical) minimum focal distance of 25 cm \pm 5%. The focal distance sets limits to the closest distance between the camera and the flow phantom. To maximize the image resolution and to capture the whole flow phantom, it was important to place the plane of interest of the flow phantom at a distance equal to that of the minimum focusing distance from the camera. This influenced the design of the flow model and set a maximum size of the 3D printed model to 94.1 mm x 137.25 mm as seen in front of the camera, as shown in the figure 32 below.

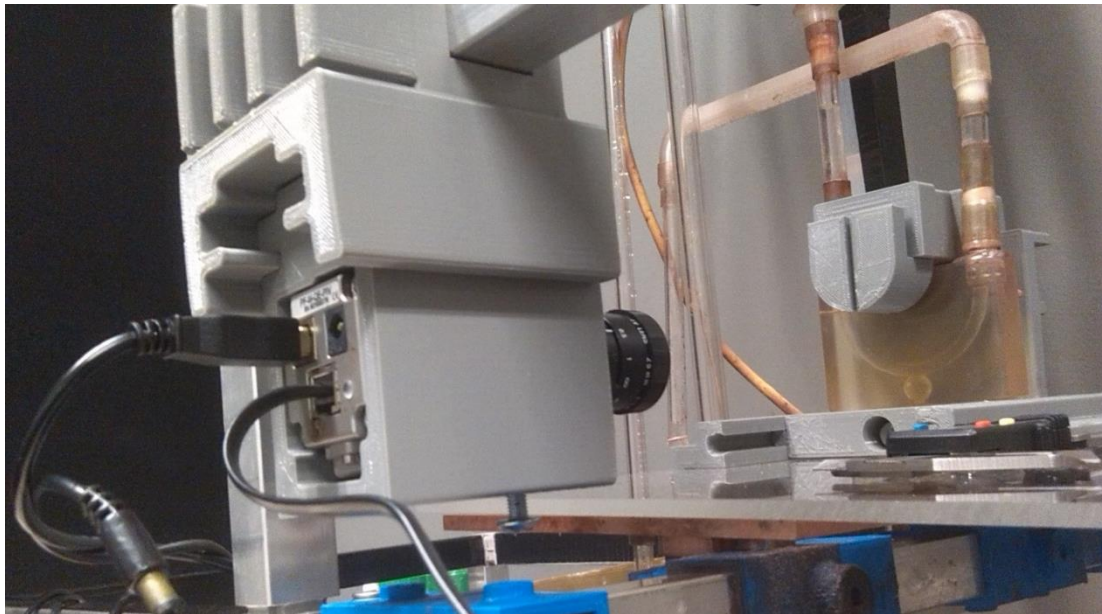
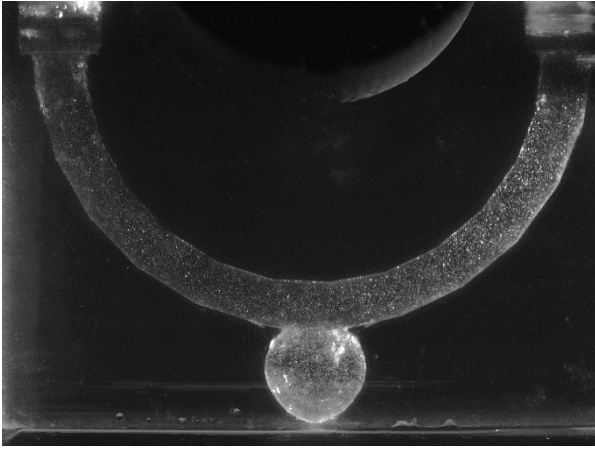


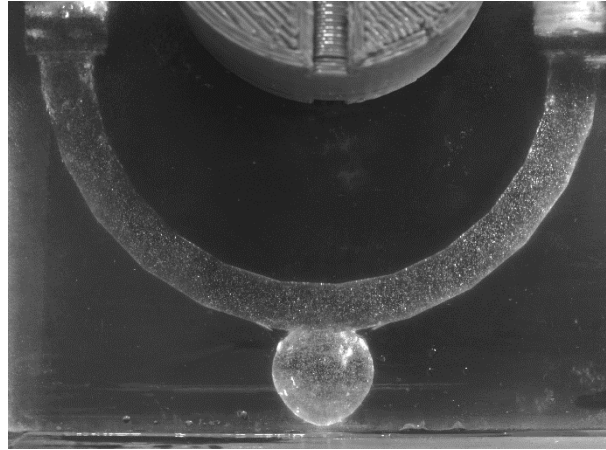
Figure 32 Front view of the printed model as seen from the camera

5.7.1. Image recording session

On average, 400 pairs of images were recorded in a single session. The first and second image within the pair are automatically named image A and B during the recording session. Figure 33 below illustrates a typical pair obtained during recording sessions.



IMAGE_A_00001



IMAGE_B_00001

Figure 33 Typical raw image pair

5.7.2. Pre-processing: Background removal

Background removal is an image pre-processing step that is undertaken after PIV image recording. Ideally, a PIV image should consist of illuminated particles on a dark background only. In practice, there is additional noise, which incorrectly populates the PIV images. This background noise results from various sources such as the laser light reflection originating from a slight mismatch in RI at the interface of different media, or noise from any other possible source (Jahanmiri, 2011). Noise constitutes a source of error during cross correlation (Guezennec and Kiritsis, 1990). Mendez *et al.*, (2017), proposed a background subtraction tool that works based on Proper Orthogonal Decomposition (POD) decomposition of PIV raw images this tool makes an approximation of the background noise source and the PIV particles pattern with reduced order models constructed from different portion of the video sequence's POD spectra. POD is also known as Karhunen-Loève decomposition, and consist of decomposing the original images into the sum of partial modes evolving with their corresponding temporal nodes. The particles images and the background are therefore identified through the comparison of the higher degrees of correlation of the particles pattern to that of the background noise. More information about the POD-based background removal for PIV can be found in their work. The algorithm that was provided works in MATLAB. In this study, the POD-based background removal technique was used during image pre-processing. Figures 34 and 35 below show the differences between the raw PIV image and the background subtracted image.

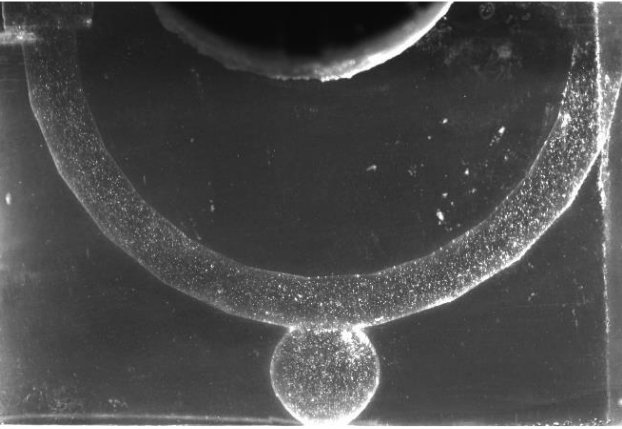


Figure 34 Raw PIV image for the idealized geometry



Figure 35 PIV image after background subtraction

5.7.3. Post-processing: Analyzing images using PIVLab

Thielicke and Stamhuis, (2010) described the process required to analyse a series of image pairs using PIVLab in MATLAB. Before carrying out an analysis, it is important to select the PIV setting. This enables application of appropriate interrogation window areas and the appropriate cross-correlation. The cross-correlation used in this work was the FFT. The analysis step generates velocity vectors that represent the displacement of particles. The following steps can be considered as important guidelines for analysing images:

- Load series of image pairs.
- Apply the exclusion (Mask) tool. This focuses the computation on the region of interest (ROI) only. The mask is specified manually and applied to all images. In order to improve accuracy of the mask contours, an additional pair of images consisting of the contour outline was inserted in the loaded series of image pairs. These added images are excluded from the averaged results. Figures 36 and 37 below show the additional image and the combined to the PIV image respectively. The additional image was drawn from the original CAD file of the model. It shows the original CAD file contours and it provides more accuracy when specifying contours.

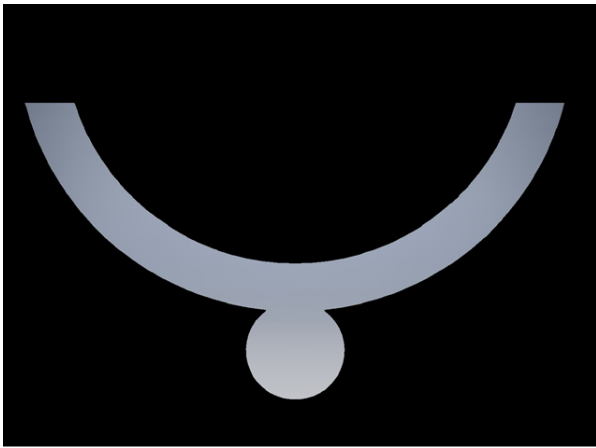


Figure 36 External image with contours of the middle plane

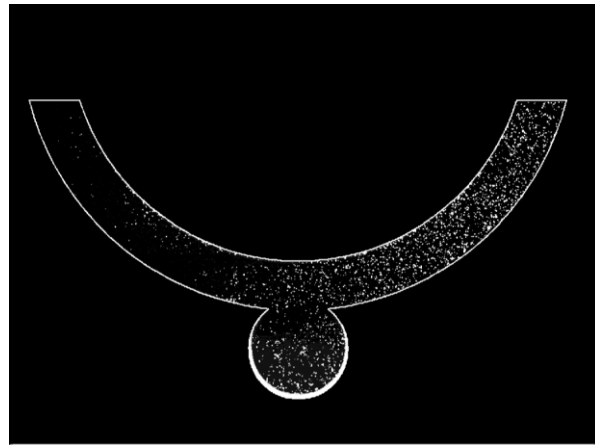


Figure 37 Blended image made of the background subtracted raw PIV image and the drawn mask

Additional post-processing steps are required in order to refine the results. These include the vector validation tool, which calibrates the vectors by selecting a known reference distance within the loaded image. By specifying this known distance and the separation time between image A and B, vectors can be scaled accordingly.

5.7.4. PIVLab results output and planes of interest

Figure 38 below shows a processed image output after PIV analyses using PIVLab. Velocity vectors are generated in pixel values. The flow direction can be observed from the arrows. Due to the scale used, the vectors in the aneurysms are not easily seen because of relatively low magnitudes.

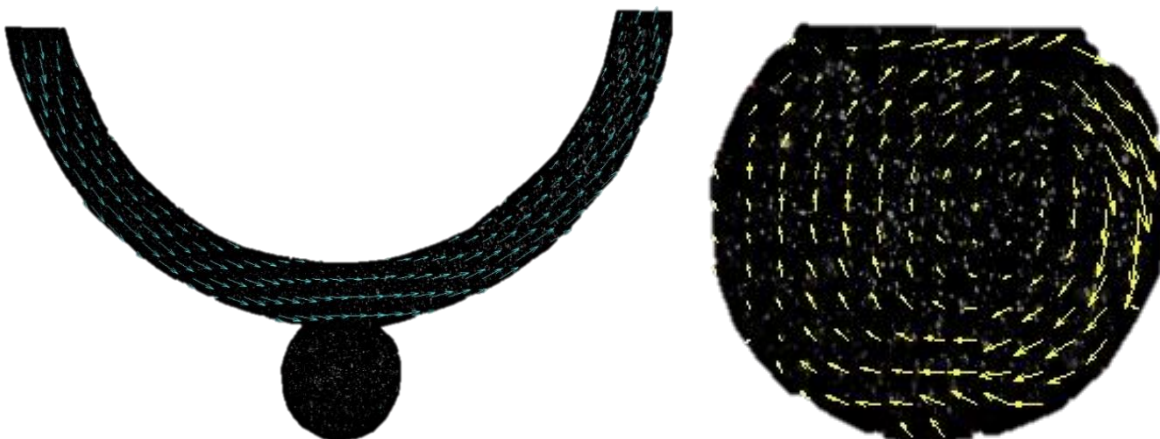


Figure 38 Typical PIV output results using PIVLab

The figures 39 show the planes on which flow measurements were conducted and the flow region in those planes. Multiple planes parallel to the center plane will be interrogated in order to give a broad view of the flow development inside the aneurysm.

Plane 1 (off center) 00 [mm] Plane 2 (off center) -02 [mm]/ +02 [mm] Plane 3 (off center) -04 [mm]/+ 04 [mm] Plane 4 (off center) -06 [mm]/+ 06 [mm]

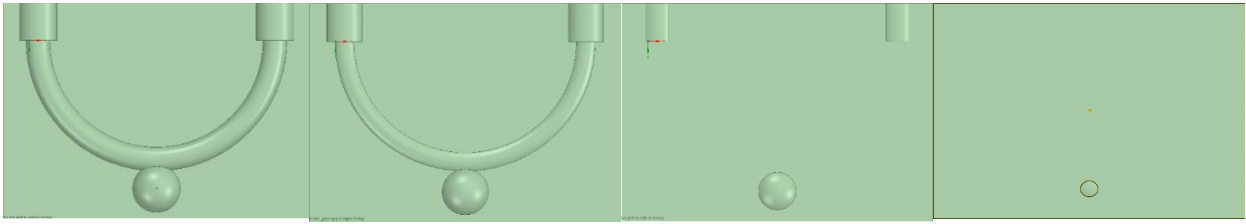


Figure 39 Planes of the idealized geometry model on which PIV analysis were conducted

5.8. Conclusion

In this chapter, the principles of PIV were explained. The importance of the laser and the camera (and how they are synchronized), and seeding particles was outlined. Achieving the correct timing is an important part of error minimization in PIV. Furthermore, PIV image processing was discussed. In the following chapter, results from the amalgamation of techniques in Chapters 3, 4 and 5 are presented.

CHAPTER 6: RESULTS AND DISCUSSION

6.1. Introduction

The previous chapters 3, 4 and 5 discussed the design and methodological approach of the flow setup, flow phantom and PIV technique. In this chapter, the steps required to conduct PIV measurements are explained gradually. Starting from the image recording using the high speed camera to the image pairs analysed using a PIV algorithm in order to generate results. This chapter presents the results of the experiments conducted using the idealized cerebral aneurysm model. First, the velocity distribution of the entire geometry is presented, and then greater detail of the aneurysm is given. In addition, several measurements are taken on different planes parallel to the front plane, thus giving insight on the flow distribution at different depths. Analysis of results and discussion are presented at the end of this chapter.

6.2. Flow velocity results

Figure 40 shows the results obtained on the middle plane of the idealised cerebral aneurysm geometry. The left column shows results for the lower inlet velocity and the right column shows results for the higher inlet velocity. From the first row, it is evident that the flow velocity is the highest on the side of parent vessel wall that has the aneurysm. In the second row, which depicts the vector and contours in the aneurysm, the scale was increased in order to zoom into the aneurysm and see the flow development inside the aneurysm. As the inlet flow rate increases, there are two significant observations to make. The first observation is that the flow increases on the outer curvature of the parent vessel which has the aneurysm located on it. The second observation shows high regions of flow rate along the rear wall of the aneurysm with a rearward off-center vortex forming. These results show that variation of flow rate has an impact on the hemodynamics inside the aneurysm. The first main impact is that more blood enters the aneurysm when the flow rate increases in the parent artery. The second major impact is that as blood enters the aneurysm, it accumulates along a portion of the wall and only a small amount finds its way back the aneurysm's opening.

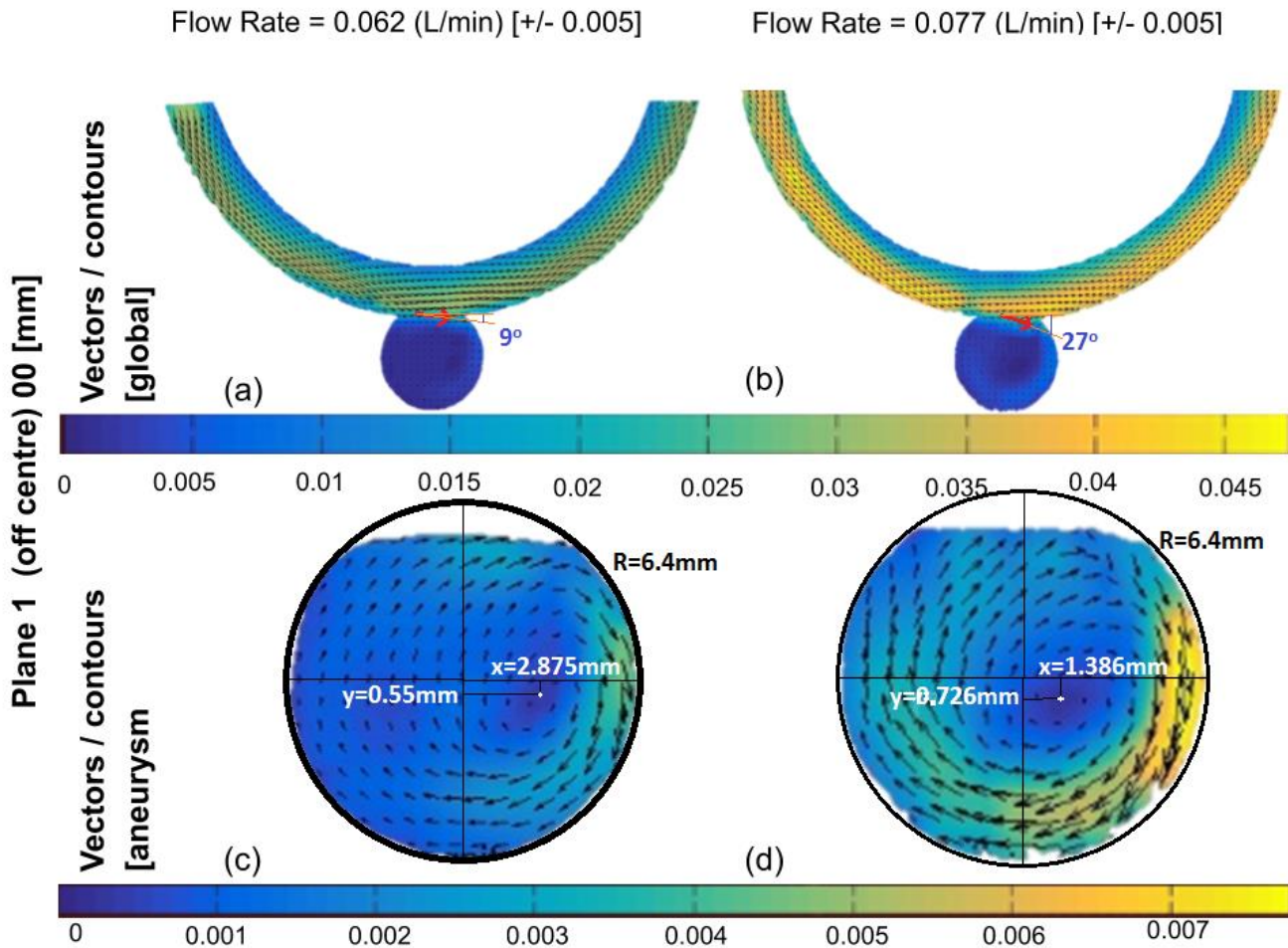


Figure 40 PIV velocity (m/s) results at middle plane of the artery

The first observation of higher velocities on the outer curvature of the parent vessel is more pronounced at higher flow rate but the eccentricity of the center of rotation is less. At the lower flow rate, the displacement was (+2.875, -0.55) whilst at higher flow rate it was (+1.386', -0.726'). This may be due to the actual angle of the in-flow into the aneurysm and the shape of the blood vessel. At the lower flow rate, the in-flow angle was -9° and at the higher flow rate it was -27° (Figure 40). This has implications on the enlargement and erosion of the aneurysm wall. The velocities near the wall of the aneurysm is also different as a result of the in-flow angle. For the low flow rate, the highest velocity inside the aneurysm was 0.005m/s located approximately at the (+6.4, 0), which is a location at the wall resulting in a wall shear stress (WSS) of 5.931 Pa. For the higher flow rate, the highest velocity was 0.0075m/s' located at approximately (+6.4, 0), resulting in the WSS of 8.896 Pa these pick values could be lower in a compliant model and therefore in the actual artery (Xu *et al.* 2016). These are all presented in Figure 40 above. The WWS can be calculated from the following formula: $\tau(y) = \mu (\delta u / \delta y)$ where μ is the dynamic viscosity; u the velocity along the boundary; y the height above the boundary.

Figure 40 contains sets of results which were taken 2 mm away from the middle plane, towards the camera. Keeping the higher inlet flow rate at 0.077 L/min and the lower inlet flow rate at 0.062 L/min. The global vectors and contours show that the velocity decreases around the regions close to the wall. When zooming in on the

aneurysm, it is evident that the flow patterns are similar regardless of the change in velocity. Observations show that on this plane, there is flow exiting the aneurysm towards the parent artery. When the flow rate is lower at inlet, more blood can escape the aneurysm, while a higher flow rate causes more recirculation inside aneurysm, this can be observed with the brown arrows on the figure 41 below.

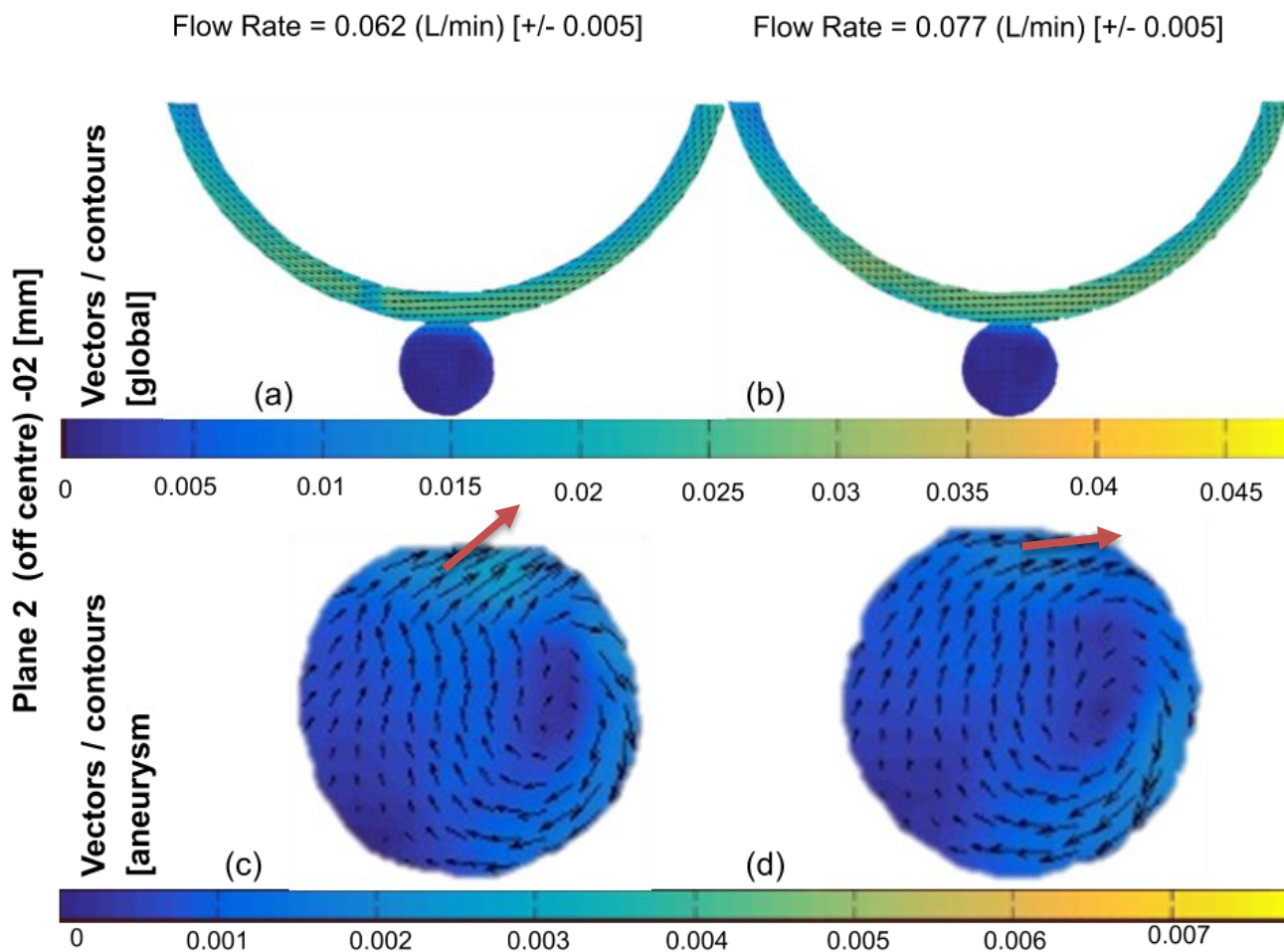


Figure 41 PIV results at a plane 2 mm away from middle plane

The set of results presented in Figure 42 were taken on a plane 4 mm away from the middle plane, towards the camera. The inlet flow rate was kept at 0.077 L/min in the right column and at 0.062 L/min in the left column. The global vectors and contours show that the velocity keeps decreasing around the regions that are closer to the wall. When zooming inside the aneurysm, the center of vorticity inside the aneurysm shifts towards to bottom on the right side as a result of inlet flow increase. The red lines mark the boundaries between regions of flow and regions of stagnation or immobility. These stagnant zones are likely to give rise to phenomena such as clotting.

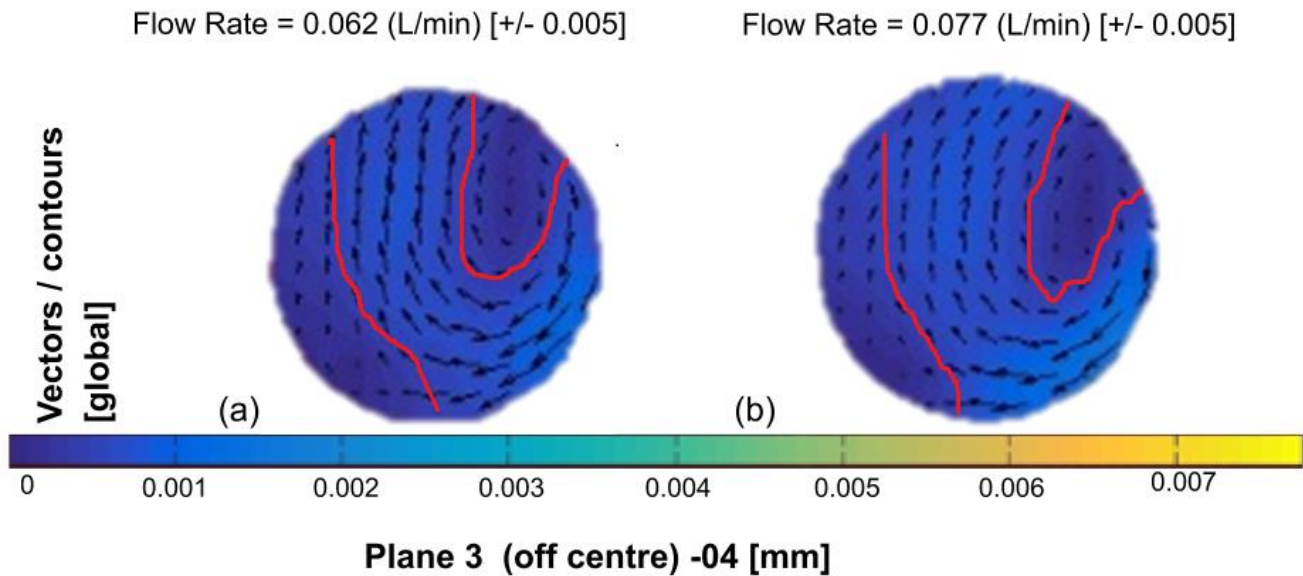


Figure 42 PIV image on plane 4 mm away from the center of aneurysm

The fourth sets of results, illustrated in the figure 43, were taken on a plane 6 mm away from the middle plane, towards the camera. The inlet flow rate was kept at 0.077 L/min in the right column and at 0.062 L/min in the left column. The global vectors and contours show that the velocity is close to zero on this plane. This region is closest to wall of the artery. The stationary flow around these regions is likely to promote clotting. There is a very slow upward displacement of fluid inside the aneurysm. The magnitude of velocity in this region is slow enough, with an average value of 0.0005 m/s, for the flow to be considered stagnant.

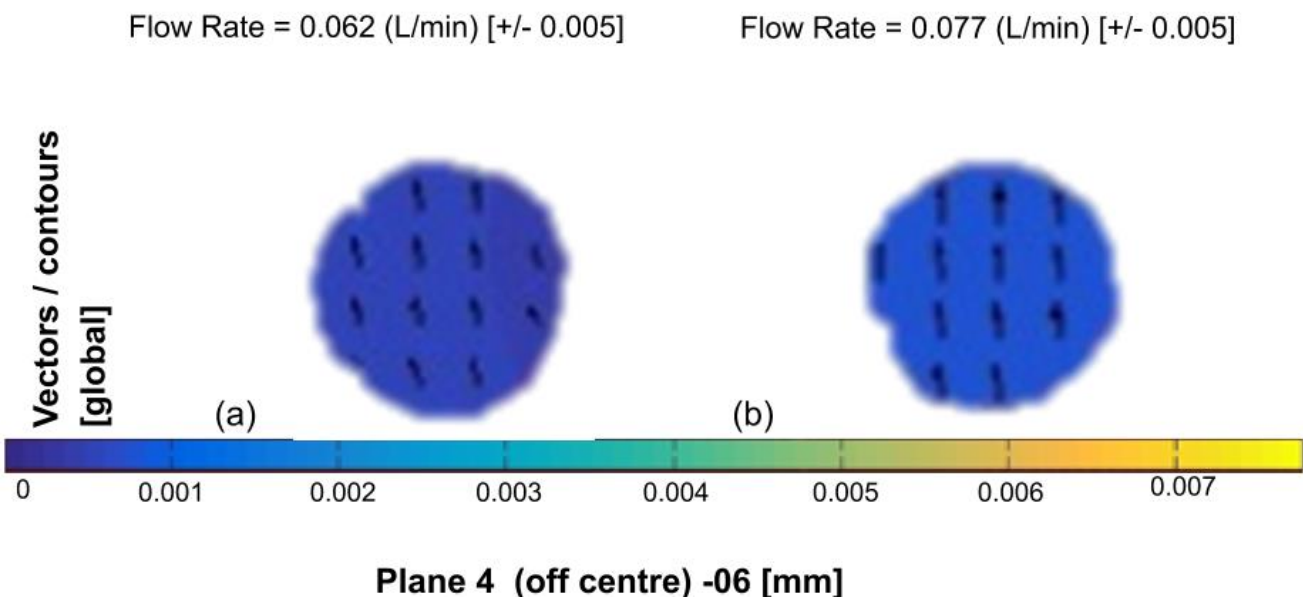


Figure 43 PIV image on plane 6 mm away from the center of aneurysm

Figure 44 below shows the location of the center of vortex on plane 2 and plane 3. Results on the figure 44 below show that the flow development inside the aneurysm is continuously changing. However, there is a constant vortex which is eccentric to the geometric center of the aneurysm.

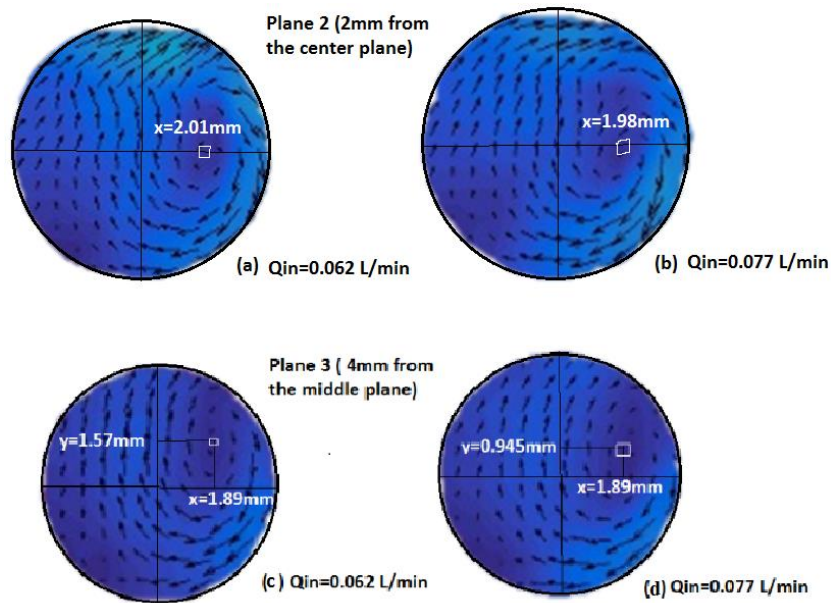


Figure 44 Vorticity location

At the center of the vortex the velocity value is close to zero and this region of blood flow is condemned to a loop that is not renewed with fresh blood. Separate work, which is done after the writing of this thesis, carried out flow visualisation using a dye. Figures 45 and 46 below show similar trend between PIV results and experimental flow visualisation through dye diffusion. The flow visualisation made use of the same PIV setup but required a channel on top of the aneurysm to introduce dye. The dyed fluid was injected with a constant flow using a controlled syringe. The similarity between the two images confirms the existence of recirculation motion inside the aneurysm. Vorticity should be regarded as an important factor when considering aneurysm hemodynamics as the resulting angular motion may have an impact on surrounding tissues.

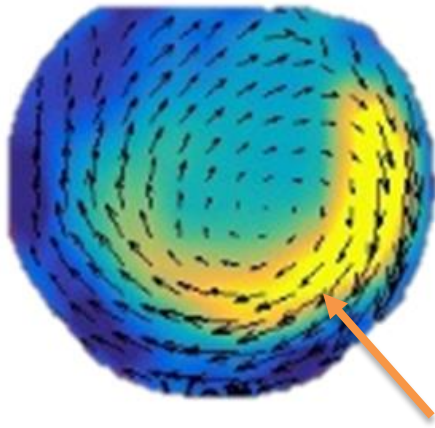


Figure 45 PIV vorticity at middle plane

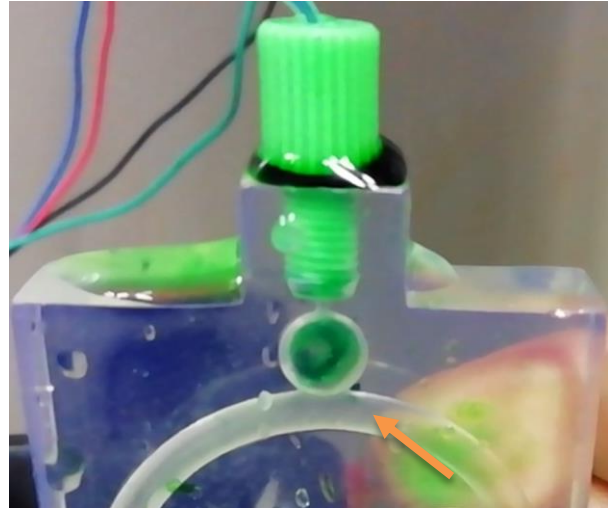


Figure 46 Flow visualization inducing dye inside the aneurysm

6.3. Evidence of hemodynamic influence in aneurysm

PIV results give clear insights into the effects of hemodynamics in an idealized cerebral aneurysm geometry. Two main observations can be made from figure 47, which represents the velocity distributions at the middle plane section. The first observation is the higher velocity (in the parent vessel) along the side of the wall where the cerebral aneurysm grows. The second observation is the higher velocity inside the aneurysm wall. These two observations may imply that the degree of curvature of the artery has an effect on blood flow inside aneurysm and influences how flow enters the aneurysm and the location of the maximal pressure on one side of the wall inside aneurysm. In addition, there is a vortex inside the aneurysm with a velocity value closer to zero at its center. This area of stagnation or immobility may favour blood accumulation.

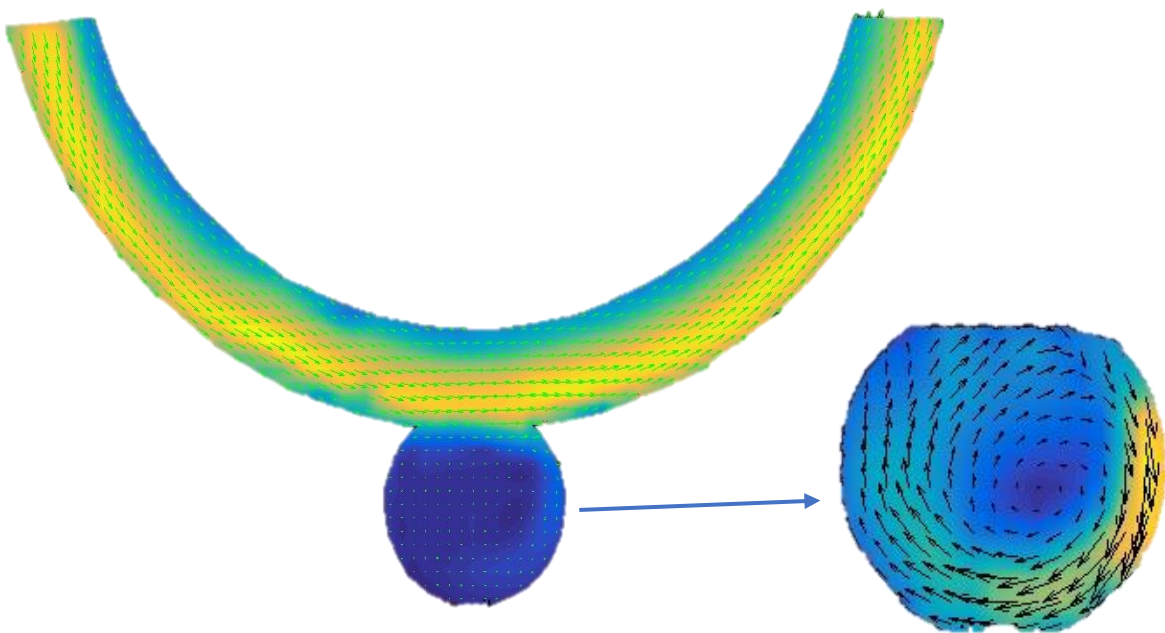


Figure 47 PIV results showing velocity distribution in the parent vessel and inside aneurysm

The difference in inlet flow rates shows a variation in flow behaviour inside the aneurysm. The concentration of the high flow region shifts towards the lower end of the aneurysm and the center of the vortex keep shifting at each plane. Higher flow rate results in more recirculation and this could be interpreted as an accumulation of blood flow inside the aneurysm and pressure increases on a localised part of the wall inside the aneurysm. There is no hard evidence to quantify flow coming out of the aneurysm. This suggests that in the case of pulsatile flow, a compliant arterial wall could attenuate the energy of blood inside the aneurysm or eject blood out of the aneurysm, depending on the elasticity limit of the aneurysm's wall.

In the artery, the velocity increases towards the external wall as it passes through the curved side of idealized geometry. The flow, which is highest on the outer edge of the bend, finds the opening of the aneurysm and forces part of the flow into the aneurysm while the remainder of the flow continues its flow towards the outlet. This shows that the positioning of the aneurysm, in relation to the curvature of the artery, has a significant impact on the aneurysm expansion.

If the aneurysm were to be positioned on the opposite side of the bend, there might be no flow therein, thus reducing the hemodynamic load on the weakened aneurysm wall (Wolfe and Bas, 2006). In this study, the results show more evidence of flow entering the aneurysm than flow exiting the aneurysm. The flow in the aneurysm is at its maximum along the wall right opposite the entry of the flow (aneurysm opening) and forms an eccentric flow field inside the aneurysm, where the origin of the vortex has the lowest velocity value.

When slicing the flow field at various locations parallel to the middle plane and outwards, it can be noticed that the flow in the main artery decreases in value the further the location is from the middle plane. The behaviour in the aneurysm seems to remain the same, having a high value at the aneurysm opening and in the vicinity of wall opposite the flow entry region. In addition, the flow is weak at the geometric center of the aneurysm.

The flow patterns are symmetric on the left side and right side of the middle plane. A few errors can be noticed further away from the middle plane, mostly due to difficulties in focusing the camera on those planes. The amount of tracer particles stacked on the wall of the aneurysm, during the experiment, make the region seem brighter and made that region empty after background subtraction. This explains the high velocity region just after the entry of the aneurysm. In general, the flow seem to flows symmetrically from the middle plane.

In this section, the results from the experiment were presented. A 3D printed flow model using an SLA 3D printer was successfully used to conduct PIV studies of cardiovascular flow. The results conducted on the idealized cerebral aneurysm show trends of behaviour of the flow. Variation of flow rates in the parent artery has an effect in the aneurysm, as demonstrated in the results. This chapter demonstrated how the PIV measurements were conducted in this work and concluded that 3D printed models can be used in PIV flow measurements.

CHAPTER 7: CONCLUSIONS AND FUTURE WORK

7.1. Conclusion

An experimental flow setup was built around a rigid 3D printed flow phantom of an idealised cerebral aneurysm in order to study the hemodynamics in such a system. The setup was built to accommodate both steady flow and pulsatile flow conditions. The pulsatile system was designed to demonstrate system capacity and was built at a fraction of the cost of a typical pulsatile pump. It made use of a computer-controlled valve to give the required pulse. However flow analysis focused on steady state conditions. Dynamic similarity was observed throughout the experiment by matching *in vivo* and *in vitro* Reynolds numbers. The working fluid was Newtonian in nature given certain constraints. Also the flow used in the experiments is sufficiently high such that blood behaves as a Newtonian fluid.

The idealized geometry of a cerebral aneurysm and the realistic geometry of a patient specific cerebral aneurysm were both 3D printed using an SLA desktop 3D printer. This greatly reduced the complexity and the cost of making the model with conventional techniques and was achieved in a shorter time when compared to traditional techniques that make use of investment casting of clear silicone. It was demonstrated that the complexity of the realistic model geometries was not a limitation as 3D printing replicated these geometries with relatively high accuracy. The clear material used for the prints still has a higher refractive index when compared to silicone. This refractive index was not a limitation, as a solution of NH_4SCN and H_2O matched the RI of the printed model. Further investigations should explore the appropriateness of 3D printing for large flow phantoms and as well as microchannels and elastic compliant models.

Measurements of the flow were done with a planar PIV setup consisting of a PIV camera and an LED laser. Free PIV software “PIVLab” was used to analyse recorded image frames. The entire setup was cost effective, and the system produced acceptable results for both the parent artery and the aneurysm.

Two distinct inlet velocities, were considered, with values of 0.033 m/s and 0.027 m/s respectively. PIV analysis showed a shift in the location of the higher velocity region inside the aneurysm as a result of the change in inlet velocity. The higher the inlet velocity, the further the region of higher velocity travelled along the wall inside the aneurysm. In the parent artery the peak value of the velocity shifted towards the wall with the aneurysm. The experimental results demonstrated the effects of hemodynamics inside the aneurysm bulge. If for instance the aneurysm were to be moved to the inside wall of the curved artery, opposite its current position on the parent vessel, results could show close if not zero flow inside the aneurysm. The above statement could be worth to consider as an endovascular approach to treat similar unruptured aneurysms.

PIV images captured with a USB 14 bit CCD camera, using a 3D printed flow model of an idealised cerebral aneurysm produced sufficiently clear images, with particles easily distinguishable after background

subtraction. These images produced useful results, which contain relevant flow features and give more insight into the behaviour of the flow and its potential contribution to aneurysmal disease evolution.

7.2. Future work

To make the experimental work more realistic, other parameters need to be considered in future work. This work provided evidence that a realistic model can be 3D printed at affordable cost. It has also demonstrated that 3D printing can open doors to producing flow phantoms with more realistic mechanical properties. This can be done by using clear elastic resin to 3D print flow models that better match the elasticity of real arteries. Formlabs has developed the RS-F2-ELCL-01, which is an elastic resin. This material can be investigated for suitability for PIV applications.

Chapter 3 presented preliminary work towards building a pulsatile system, which can be programmed for particular flow conditions, at a fraction of the cost of available pulsatile pumps. This system needs to be refined and tested in PIV experiments, to gauge the accuracy of the flow profile produced.

Finally, the working fluid used in this study provided the required properties to conduct the experimental measurements successfully. Future work still needs to address the need for a more appropriate working fluid, in order to render the experimental results more realistic. Striking a balance between matching the properties of blood while being suitable for PIV experiments will prove, no doubt, challenging.

REFERENCES

Anton-Paar (2000) 'Viscosity Measurement of Whole Blood', pp. 1–5.

Aparício, P., Thompson, M. S. and Watton, P. N. (2016) 'A novel chemo-mechano-biological model of arterial tissue growth and remodelling', *Journal of Biomechanics*. Elsevier, 49(12), pp. 2321–2330. doi: 10.1016/j.jbiomech.2016.04.037.

Aycock, K. I., Hariharan, P. and Craven, B. A. (2017) 'Particle image velocimetry measurements in an anatomical vascular model fabricated using inkjet 3D printing', *Experiments in Fluids*. Springer Berlin Heidelberg, pp. 1–8. doi: 10.1007/s00348-017-2403-1.

Berg, P. *et al.* (2014) 'Cerebral blood flow in a healthy Circle of Willis and two intracranial aneurysms: computational fluid dynamics versus four-dimensional phase-contrast magnetic resonance imaging.', *Journal of biomechanical engineering*, 136(4), pp. 1–9. doi: 10.1115/1.4026108.

Borrero-Echeverry, D. and Morrison, B. C. A. (2016) 'Aqueous ammonium thiocyanate solutions as refractive index-matching fluids with low density and viscosity', *Experiments in Fluids*. Springer Berlin Heidelberg, 57(7), pp. 1–5. doi: 10.1007/s00348-016-2207-8.

Bouillot, P. *et al.* (2014) 'Multi-time-lag PIV analysis of steady and pulsatile flows in a sidewall aneurysm'. doi: 10.1007/s00348-014-1746-0.

Cholemari, M. R. (2007) 'Modeling and correction of peak-locking in digital PIV', *Experiments in Fluids*, 42(6), pp. 913–922. doi: 10.1007/s00348-007-0300-8.

Chong, W. *et al.* (2014) 'Computational Hemodynamics Analysis of Intracranial Aneurysms Treated with Flow Diverters : Correlation with Clinical Outcomes', pp. 136–142.

esculap Neurosurgery (2012) *Brain Aneurysm, Bulletin of the History of Medicine*.

Ford, M. D. *et al.* (2005) 'Virtual angiography for visualization and validation of computational models of aneurysm hemodynamics', *IEEE Transactions on Medical Imaging*, 24(12), pp. 1586–1592. doi: 10.1109/TMI.2005.859204.

Ford, M. D. *et al.* (2008) 'PIV-Measured Versus CFD-Predicted Flow Dynamics in Anatomically Realistic Cerebral Aneurysm Models', *Journal of biomechanical engineering*, 130(2), p. 021015. doi: 10.1115/1.2900724.

Geoghegan, P. H. *et al.* (2012) 'Fabrication of rigid and flexible refractive-index-matched flow phantoms for flow visualisation and optical flow measurements', *Experiments in Fluids*, 52(5), pp. 1331–1347. doi: 10.1007/s00348-011-1258-0.

Geoghegan, P. H. (2012a) *In Vitro Experimental Investigation Into the Effect of Compliance on Models of Arterial Hemodynamics*.

Geoghegan, P. H. (2012b) 'In Vitro Experimental Investigation Into the Effect of Compliance on Models of Arterial Hemodynamics'.

Guezennec, Y. G. and Kiritsis, N. (1990) 'Doh2000.pdf', *Experiments in Fluids*, 10, pp. 138–146. doi: 10.1007/BF00215022.

Huang, H., Dabiri, D. and Gharib, M. (1997) 'On errors of digital particle image velocimetry', *Measurement Science and Technology*, 8(12), pp. 1427–1440. doi: 10.1088/0957-0233/8/12/007.

Jahanmiri, M. (2011) 'Particle Image Velocimetry: Fundamentals and Its Applications Particle Image Velocimetry : Fundamentals and Its Applications'.

Jermy, M. C. (2013) 'MAKING IT CLEAR : FLEXIBLE , TRANSPARENT LABORATORY FLOW MODELS FOR SOFT AND HARD PROBLEMS Re Reynolds number U m mean velocity', *8th World Conference on Experimental Heat Transfer, Fluid Mechanics, and Thermodynamics*, pp. 1–8.

Kakalis, N. M. P. *et al.* (2008) 'The Hemodynamics of Endovascular Aneurysm Treatment : A Computational Modelling Approach for Estimating the Influence of Multiple Coil Deployment', 27(6), pp. 814–824.

Kefayati, S. (2013) 'PIV-based investigation of hemodynamic factors in diseased carotid artery bifurcations with varying plaque geometries', (September), p. xx + 180. Available at: <http://ir.lib.uwo.ca/cgi/viewcontent.cgi?article=2896&context=etd>.

Kim, M. *et al.* (2008) 'Comparison of two stents in modifying cerebral aneurysm hemodynamics', *Annals of Biomedical Engineering*, 36(5), pp. 726–741. doi: 10.1007/s10439-008-9449-4.

Krings, T., Mandell, Daniel M., *et al.* (2011) 'Intracranial aneurysms: from vessel wall pathology to therapeutic approach', *Nature Reviews Neurology*. Nature Publishing Group, 7(10), pp. 547–559. doi: 10.1038/nrneurol.2011.136.

Krings, T., Mandell, Daniel M, *et al.* (2011) 'Intracranial aneurysms from vessel wall pathology to therapeutic', *Nature Reviews Neurology*. Nature Publishing Group, 7(10), pp. 547–59. doi: 10.1038/nrneurol.2011.136.

- Ku, D. N. (1997) 'Blood Flow in Arteries', *Annual Review of Fluid Mechanics*, 29(1), pp. 399–434. doi: 10.1146/annurev.fluid.29.1.399.
- Le, T. B., Borazjani, I. and Sotiropoulos, F. (2010) 'Pulsatile flow effects on the hemodynamics of intracranial aneurysms.', *Journal of biomechanical engineering*, 132(11), p. 111009. doi: 10.1115/1.4002702.
- Macleod, M. R. *et al.* (2015) 'Risk of Bias in Reports of In Vivo Research : A Focus for Improvement', pp. 1–12. doi: 10.1371/journal.pbio.1002273.
- Medero, R. *et al.* (2017) 'Patient-specific in vitro models for hemodynamic analysis of congenital heart disease – Additive manufacturing approach', *Journal of Biomechanics*. Elsevier Ltd, 54, pp. 111–116. doi: 10.1016/j.jbiomech.2017.01.048.
- Mendez, M. A. *et al.* (2017) 'POD-based background removal for particle image velocimetry', *Experimental Thermal and Fluid Science*. Elsevier Inc., 80, pp. 181–192. doi: 10.1016/j.expthermflusci.2016.08.021.
- Mulder, G. *et al.* (2009) 'On automated analysis of flow patterns in cerebral aneurysms based on vortex identification', *Journal of Engineering Mathematics*, 64(4), pp. 391–401. doi: 10.1007/s10665-009-9270-6.
- Nair, P. *et al.* (2016) 'Hemodynamic characterization of geometric cerebral aneurysm templates', *Journal of Biomechanics*. Elsevier, 49(11), pp. 2118–2126. doi: 10.1016/j.jbiomech.2015.11.034.
- Ng, W. L. *et al.* (2018) 'Proof-of-concept : 3D bioprinting of pigmented human skin constructs Proof-of-concept : 3D bioprinting of pigmented human skin constructs'. IOP Publishing.
- Ngoepe MN, V. Y. (2016) 'Computational modelling of clot development in patient- specific cerebral aneurysm cases', (March 2015), pp. 262–272. doi: 10.1111/jth.13220.
- Norman, P. E. and Powell, J. T. (2010) 'Site specificity of aneurysmal disease', *Circulation*. doi: 10.1161/CIRCULATIONAHA.109.880724.
- Organization World Health (ed.) (2018) *World health statistics 2018: monitoring health for the SDGs, sustainable development goals*. 2018th edn. Geneva.
- Packet, S. (2006) 'Overview of Adult Traumatic Brain Injuries', *Prevention*, pp. 1–57.
- Peach, T. *et al.* (2014) 'The Sphere: A Dedicated Bifurcation Aneurysm Flow-Diverter Device', *Cardiovascular Engineering and Technology*, 5(4), pp. 334–347. doi: 10.1007/s13239-014-0188-4.
- Roloff, C. *et al.* (2013) 'Investigation of the velocity field in a full-scale model of a cerebral aneurysm',

- International Journal of Heat and Fluid Flow*. Elsevier Inc., 43, pp. 212–219. doi: 10.1016/j.ijheatfluidflow.2013.06.006.
- Sheppard, M. N. (2012) 'Diseases of blood vessels', *Surgery (United Kingdom)*. Elsevier Ltd, 30(8), pp. 370–376. doi: 10.1016/j.mpsur.2012.05.017.
- Song, M., Choi, H. and Kim, E. (2013) 'Matching Index-of-Refraction for 3D Printing Model Using Mixture of Herb Essential Oil and Light Mineral Oil', *Transactions of the Korean Nuclear Society Autumn Meeting*, (3), pp. 24–25.
- Stehbens, W. E. (1958a) 'History of aneurysms.', *Medical history*, 2(4), pp. 274–80. doi: 10.1017/S0025727300023978.
- Stehbens, W. E. (1958b) 'History of aneurysms', *Medical History*, 2(4), pp. 274–280. doi: 10.1017/S0025727300023978.
- Supply, B. (2010) 'Internal Carotid Arteries Vertebral Arteries Circle of Willis Medial View MCA and Penetrating arteries Angiogram (aka arteriogram) Dural Sinus (Superior Sagittal)', pp. 1–9.
- Tamer, Hassan & Yasser, M. A. & A. A. H. (2011) 'The adverse effects of flow-diverter stent-like devices on the flow pattern of saccular intracranial aneurysm models : computational fluid dynamics study', pp. 1633–1640. doi: 10.1007/s00701-011-1055-9.
- The UCAS Japan, I. (2012) 'The Natural Course of Unruptured Cerebral Aneurysms in a Japanese Cohort', *New England Journal of Medicine*, 366(26), pp. 2474–2482. doi: 10.1056/NEJMoa1113260.
- Thielicke, W. (2014) 'The flapping flight of birds Digital Particle Image Velocimetry (Unpublished doctoral dissertation)', pp. 1–39. Available at: <http://irs.ub.rug.nl/ppn/382783069>.
- Thielicke, W. and Stamhuis, E. J. (2010) 'PIVlab - T IME -R ESOLVED D IGITAL P ARTICLE I MAGE V ELOCIMETRY T OOL FOR MATLAB', pp. 1–4.
- Trager, A. L. *et al.* (2009) '(Correlation Between Angiographic and Particle Image Velocimetry Quantifications of Flow Diverters in an In Vitro Model of Elastase- Induced)', *Journal of biomechanical engineering*, 131(3), p. 034506. doi: 10.1115/1.3049528.
- Tran, H. (2004) 'Coronary Artery Disease ', *October*, 292(15), pp. 1867–1874. doi: 10.1007/978-1-4471-2828-1.
- Wolfe, S. Q. and Bas, M. K. (2006) 'Cerebral Aneurysms : Learning from the Past and Looking toward the

Future', 53, pp. 157–178.

Xu, L. *et al.* (2016) 'Effect of elasticity on wall shear stress inside cerebral aneurysm at anterior cerebral artery', 24, pp. 349–357. doi: 10.3233/THC-161135.

Yasuda, R. *et al.* (2011) 'Aneurysm volume-to-ostium area ratio: A parameter useful for discriminating the rupture status of intracranial aneurysms', *Neurosurgery*, 68(2), pp. 310–317. doi: 10.1227/NEU.0b013e3182010ed0.

Yazici, B., Erdoğan, B. and Tugay, A. (2005) 'Cerebral blood flow measurements of the extracranial carotid and vertebral arteries with Doppler ultrasonography in healthy adults.', *Diagnostic and interventional radiology (Ankara, Turkey)*, 11(4), pp. 195–198. doi: 16320223.

Yu, C. H. *et al.* (2012) 'A steady flow analysis on a cerebral aneurysm model with several stents for new stent design using PIV', *Journal of Mechanical Science and Technology*, 26(5), pp. 1333–1340. doi: 10.1007/s12206-012-0322-x.

Zöllner (2014) *Blood Flow Measurement Techniques*.

Appendix A – Specifications of the Firefly Laser

General	
Light Source	Semiconductor laser
Laser Class	Class 4 (IV)
Wavelength of emission	808nm \pm 3nm
Peak power	300 watts*
Pulse energy	0.15mJ to 30mJ
Individual pulse length	0.25 μ s to 100 μ s
Maximum duty cycle	1%
Maximum external trigger frequency	0Hz - 10 kHz (dependant on model)
Internal trigger frequency	1Hz - 10 kHz (dependant on model)
Pulse separation (in burst mode)	Range 0.5 μ s - 9999 μ s
* Dependant on model (200W also available)	
Electrical	
Fuses	Internal – not user serviceable
The laser may be connected to a fused plug or outlet to provide additional electric shock protection.	
Input power	100 to 240 VAC, 50/60 Hz, 500W
Trigger input	TTL (4.5V @ 1M Ω)
Trigger delay	10ns to 0.5s
Mechanical	
Dimensions (mm)	
Laser head (L \times W \times H)	220* \times 70 \times 125
Control unit: (W \times H \times D)	200 \times 75 \times 320*
*including umbilical cable attachment. Does not include allowance for cable bend radius. You should allow 50mm for cable bend.	

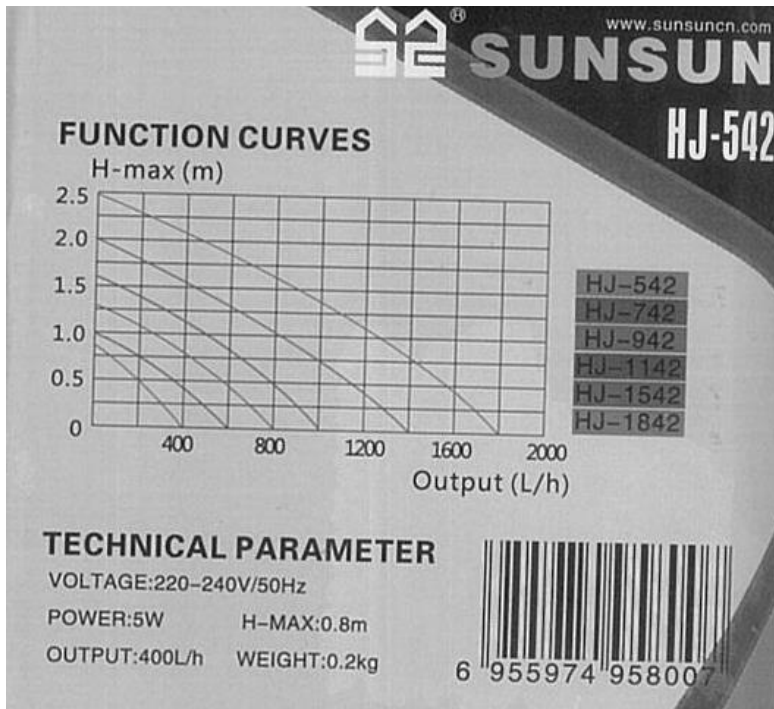
Appendix B – Specifications of the pco.pixelfly PIV camera

This high performance **digital 14bit CCD camera system** features state of the art in CCD and electronics technology. The pco.pixelfly usb has **extraordinary high quantum efficiency**, high dynamic range and **very low readout noise**. Available exposure times range from microseconds to a minute.



<ul style="list-style-type: none">• Ultra compact design
<ul style="list-style-type: none">• Dimensions: 72 x 39 x 47 mm
<ul style="list-style-type: none">• 14 bit dynamic range
<ul style="list-style-type: none">• High resolution 1392 x 1040 pixel
<ul style="list-style-type: none">• superior quantum efficiency up to 62%
<ul style="list-style-type: none">• Exposure times from 1 μs - 60 s
<ul style="list-style-type: none">• Temperature compensated
<ul style="list-style-type: none">• USB 2.0

Appendix C – Specifications of the SunSun Pump



Appendix D – Specifications of the Flow Meter



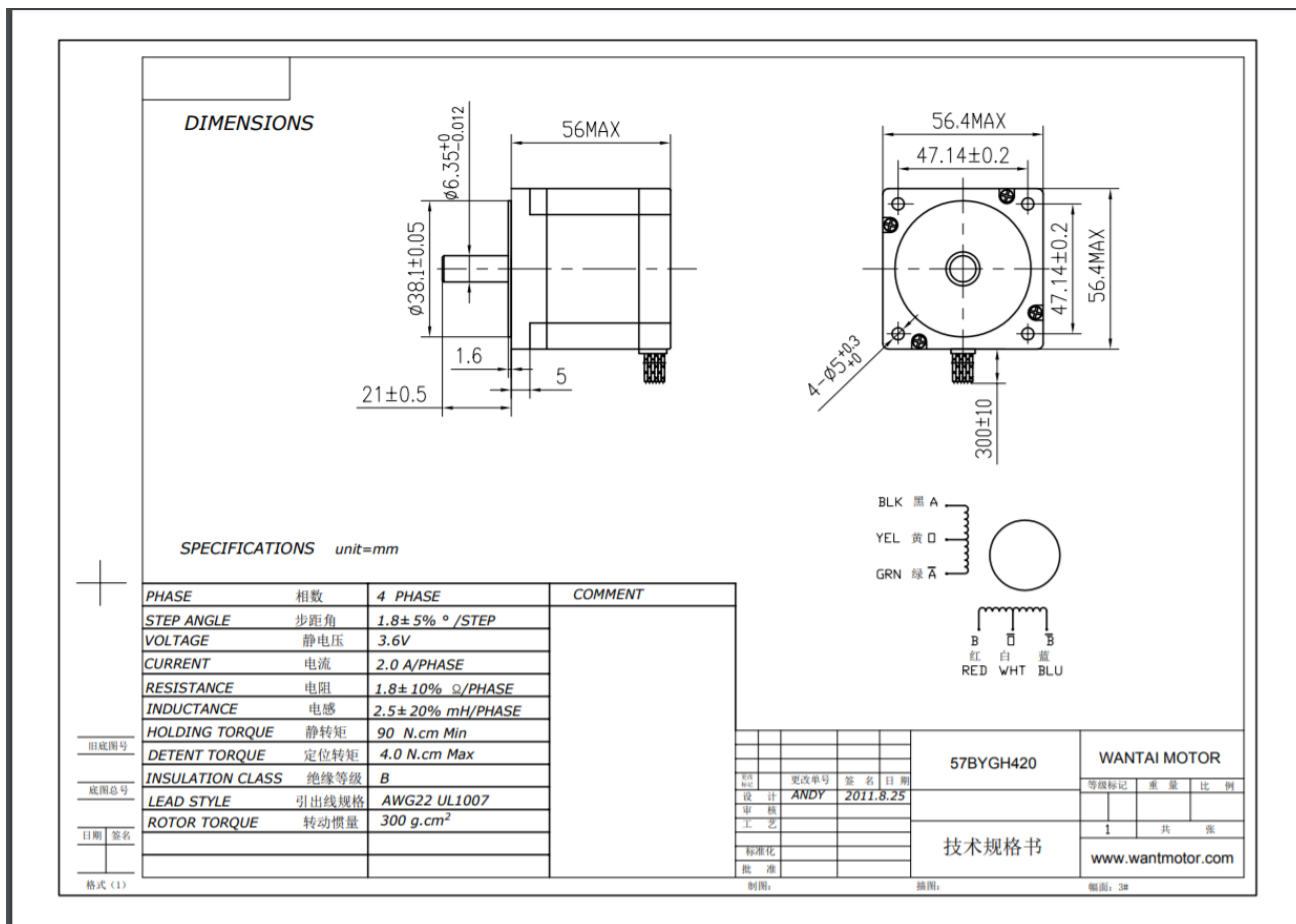
Body	Nylon 12 (Grilamid TR55)
Turbine	Nylon 12 Composite
Bearings	PTFE/15% Graphite
Operating Pressure	350 PSI (24 bar)
Burst Pressure	1400 PSI (97 bar)
Flow Range	0.026-.65 gallons/minute
	0.1-2.5 liters/minute
	3.4-84.5 ounces/minute
Pulses	83,200 per gallon
	22,000 per liter

	650 per ounce
Frequency Output	36.6-917 Hz
Operating Temperature	-4°F to 212°F (-20°C to 100°C)
Viscosity	32 to 70 SSU (0.8 to 16 Centistokes)
Filter	<50 Microns
Input Power	5 to 24 VDC
Output (Hz) NPN Sinking Open Collector @ 20mA Maximum Leakage	
Current	10µA (3K-30K Pull up resistor required)
Accuracy	±3% of Reading
Repeatability	0.5% of Full Scale
Electrical Connection	9.4mm Spacing 3-pole DIN Connector (1" high)
Inlet/Outlet Ports	1/4" NPT (1/4" G Male also available)

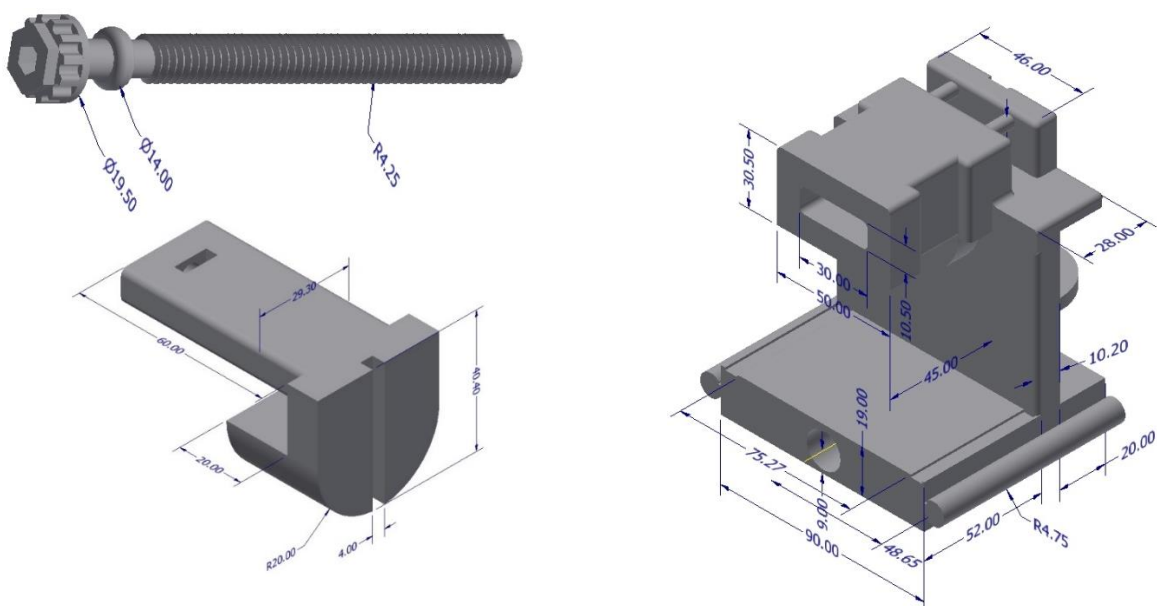
Appendix E – clear photopolymer resin form 2 material sheet

CLEAR FLGPCL03 ¹					
	METRIC ²		IMPERIAL ²		METHOD
	Green ³	Postcured ⁴	Green ³	Postcured ⁴	
Mechanical Properties					
Ultimate Tensile Strength	38 MPa	65 MPa	5510 psi	9380 psi	ASTM D 638-10
Young's Modulus	1.6 GPa	2.8 GPa	234 ksi	402 ksi	ASTM D 638-10
Elongation at Failure	12 %	6.2 %	12 %	6.2 %	ASTM D 638-10
Flexural Modulus	1.25 GPa	2.2 GPa	181 ksi	320 ksi	ASTM C 790-10
Notched IZOD	16 J/m	25 J/m	0.3 ft-lbf/in	0.46 ft-lbf/in	ASTM D 256-10
Thermal Properties					
Heat deflection temp. @ 264 psi	42.7 °C	58.4 °C	108.9 °F	137.1 °F	ASTM D 648-07
Heat deflection temp. @ 66 psi	49.7 °C	73.1 °C	121.5 °F	163.6 °F	ASTM D 648-07

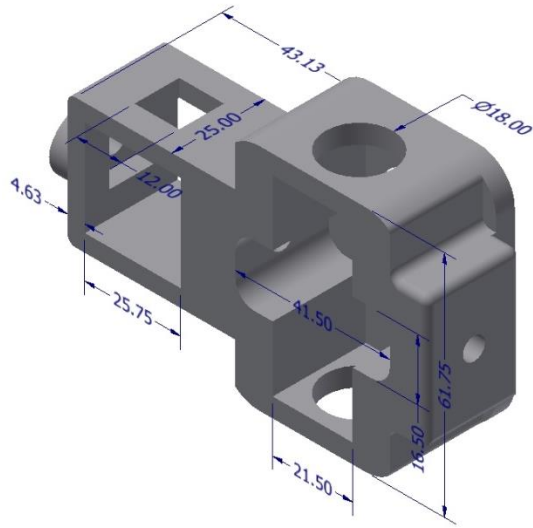
Appendix F – Stepper motor



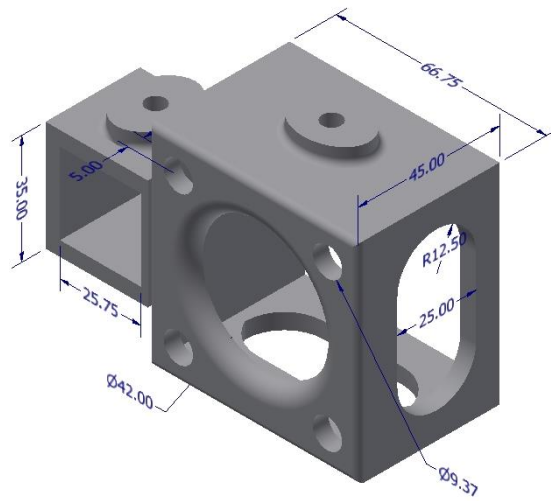
Appendix G – Flow setup (3D printed parts)



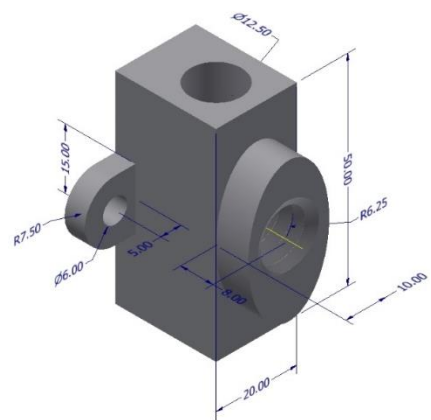
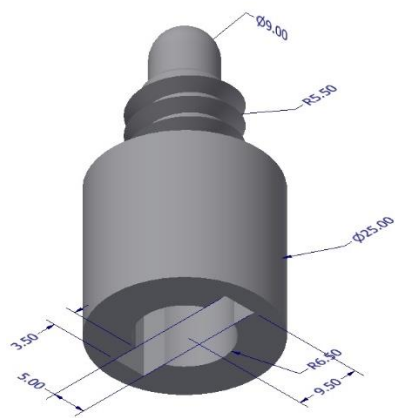
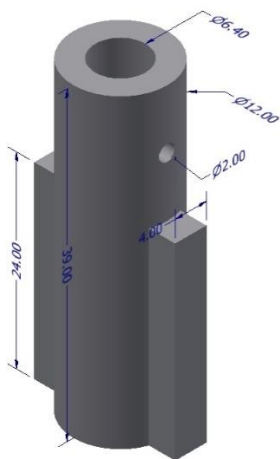
3D printed flow phantom mounting



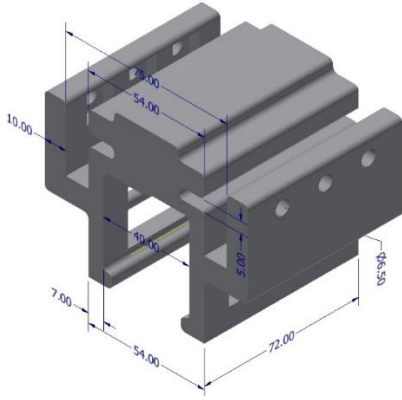
Screw valve mounting



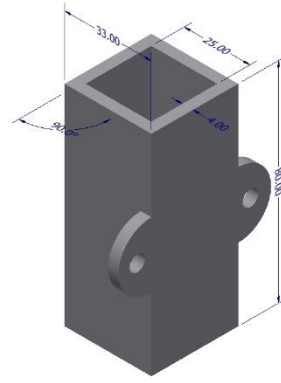
Stepper motor holder



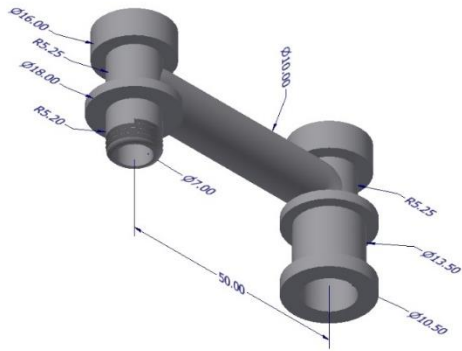
3D printed Screw valve and connector



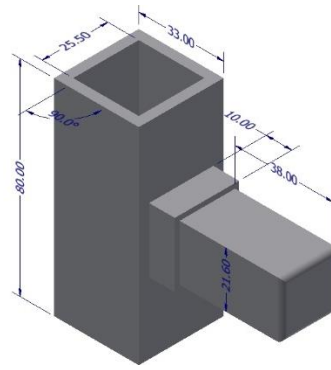
camera mounting



sliding connector



tubing connector



frame connector